
Article:
Pessu, F orcid.org/0000-0003-3587-4309, Hua, Y orcid.org/0000-0002-7457-1813, Barker, R orcid.org/0000-0002-5106-6929 et al. (1 more author) (2018) A Study of the Pitting and Uniform Corrosion Characteristics of X65 Carbon Steel in Different H2S-CO2-Containing Environments. CORROSION, 74 (8). pp. 886-902. ISSN 0010-9312

https://doi.org/10.5006/2537

A study of the pitting and uniform corrosion characteristics of X65 carbon steel in different H_2S-CO_2-containing environments.

Frederick Pessu, Yong Hua,*,** Richard Barker, ***and Anne Neville.****

Institute of Functional Surfaces (iFS), School of Mechanical Engineering.

Article history: (This style is Article Info subhead)

Received Day Month Year (This style is Article History and Keywords)
Accepted Day Month Year
Available Day Month Year

Keywords: (This style is Article Info subhead)

A. Hydrogen sulfide corrosion
B. Carbon dioxide corrosion
C. Iron sulfide
D. Pitting corrosion
E. Uniform corrosion.

* Institute of Functional Surfaces (iFS), School of Mechanical Engineering, University of Leeds. Leeds. United Kingdom. LS2 9JT.**

***Dr Frederick Pessu: Email: (f.o.pessu@leeds.ac.uk).

ABSTRACT

There have been increasing concerns related to the challenges posed by hydrogen sulfide (H_2S) corrosion to the integrity of oilfield pipeline steels. In environments containing variable quantities of both carbon dioxide (CO_2) and H_2S gas, the corrosion behavior of carbon steel can be particularly complex. There is still no universal understanding of the changes in the mechanisms, sequence of electrochemical reactions and impact on the integrity of carbon steel materials as a result of changes in H_2S-CO_2 gas ratio. The film formation process, film characteristics and morphology in CO_2 and H_2S-containing systems are also known to be different depending upon the environmental and physical conditions and this influences the rates of both general and pitting corrosion. Questions still remain as to how the combined presence of CO_2 and H_2S gases at different partial pressure ratios influence the corrosion mechanisms, as well as initiation and propagation of surface pits. This paper presents an investigation into the overall (i.e. general and pitting) corrosion behavior of carbon steel in CO_2-H_2S-containing environments. The work explores the impact of changes in ratios of CO_2 and H_2S partial pressures at both 30 and 80°C in a 3.5 wt. % NaCl solution. All experiments are performed at atmospheric pressure, while H_2S gas content is varied at 0 ppm (0 mol. %) 100 ppm (0.01 mol. %), 1000 ppm (0.1 mol. %) 10,000 ppm (1 mol. %) and 100,000 ppm (10 mol. %) in H_2S-CO_2 corrosion environments. Corrosion film properties and morphology are studied through a combination of scanning electron microscopy and X-ray diffraction. The results show that the morphology and composition of iron sulfide formed changes with H_2S gas concentration due to the continuous interaction of the corrosion interface with the corrosion media even in the presence of initially formed FeS (mainly mackinawite). This often leads to the formation of a different morphology of mackinawite as well as different polymorphs of FeS. This also has the impact of either increasing or decreasing the uniform corrosion rate at low and higher concentration of H_2S gas depending on the temperature. Pitting corrosion is also evaluated after 168 h to determine the impact of increasing H_2S content on the extent and morphology of pitting corrosion attack. The results from the pitting corrosion investigation show that increased and severe pitting corrosion attack occurs at higher H_2S concentration and temperature. The morphology of pitting corrosion attack is also linked to the changes in the H_2S content with an indication of a critical concentration range at which the nature of attack changes from narrow and small diameter pits to severe localized attack. The critical concentration threshold for such transition is shown in this study to reduce with increasing temperature.

INTRODUCTION

The mechanism of sour (H_2S/hydrogen sulfide) corrosion is known by the research community to be more complex than sweet (CO_2/carbon dioxide) corrosion. Studies on the corrosion of carbon steel in H_2S and/or H_2S-CO_2 containing oilfield environments have consistently highlighted such inherent complexity with respect to the combining mechanisms that influence its degradation process[1]. Recent findings have helped to establish the notion that H_2S corrosion is dominated by two processes: a "solid state" reaction and an aqueous phase corrosion reaction [2-4]. The solid state reaction is considered to be a heterogeneous reaction between H_2S and/or HS^- and Fe at the steel surface leading to the formation of iron sulfide corrosion products; mainly mackinawite[4-6]. The solid state reaction also precedes an aqueous phase H_2S-driven corrosion reaction. The aqueous phase corrosion reaction usually dominates the latter stages of H_2S corrosion as it is believed to control the process of transformation of initially formed FeS (mackinawite) to other more thermodynamically stable forms of iron sulfide [7-9].

Recent studies [1, 5, 10] have reported various implications of H_2S induced corrosion pathways, but with continued emphasis on the general corrosion behavior of carbon steel exposed to H_2S-containing conditions. Some of these studies are based on short duration tests and consequently prevent elucidation of the potential long term implications of H_2S-corrosion with respect to iron sulfide evolution and the effect on pitting corrosion. According to recent publications [1, 3, 5], the general corrosion rate of steel exposed to a H_2S-corrosion environment is significantly reduced with low concentrations of H_2S gas at 30°C. Reduction in corrosion rate in the presence of H_2S concentration as low as between 100 ppm to 500 ppm was attributed to the formation of a very thin mono-layer of chemisorbed Fe-S_{ad} onto the steel surface[1, 3] and in other instances, to the formation of mackinawite via solid state reaction in a system containing ~908 ppm of H_2S in the gas phase of an acidic media[5].

The adsorbed monolayer is thought to be capable of displacing adsorbed H_2O and OH^- from the steel surface[1], resulting in the kinetics of electrochemical reactions (Fe dissolution, H_2O reduction and carbonic acid/hydrogen reduction) being slowed down, possibly through an alteration to the properties of the electric double layer. However, increasing H_2S content has been shown to result in enhancement of the overall cathodic reaction through the contribution of the "solid state" of H_2S with the steel surface. This enhancement was observed by Zheng et al.[1], who reported a gradual increase in the general corrosion rate with increasing H_2S concentrations from 0.65% to 10%.

Iron sulfide corrosion products are likely to form on carbon steel exposed to H_2S-containing environments, with their kinetics, chemistry and morphology depending on both environmental and physical factors such as temperature/pH and flow conditions, respectively [4, 11, 12]. Once formed, iron sulfide has been shown to become an important factor in

the evolution of uniform and pitting corrosion[13]. The role of iron sulfide in this scenario is also dependent on the corrosion process preceding its formation, as well as the film's chemical composition, physical properties, nature and morphology. The complex changes associated with the evolution and formation of iron sulfide over time meant that the pitting and uniform corrosion damage on carbon steel in H_2S systems becomes particularly challenging to predict. Consequently, studies based on long-term exposure and detailed electrochemical data have become increasingly relevant in the understanding of H_2S corrosion of carbon steel, especially with published evidence of localized corrosion coinciding with the formation and/or breakdown of initially formed FeS (mackinawite) corrosion products[8] and in other instances, localized corrosion also correlating with the formation of other specific forms of iron sulfide[14].

The studies by Zheng et al[1] were based on 2 h experiments and did not take into account the complexities associated with film formation and the localized corrosion that may occur given the characteristic electronically-conductive nature of iron sulfide corrosion products. Such characteristics could influence the overall long-term corrosion behavior of steels. The purpose of this work is to investigate the effect of different H_2S concentrations in a mixed H_2S-CO_2-containing corrosion environment on the evolution of iron sulfide formation, pitting and uniform corrosion. This study is based on 168 h experiments that ensure the effect of *in-situ* changes in iron sulfide properties are taken into consideration in the analysis on pitting and uniform corrosion of carbon steel materials. This study also explores the propensity for pitting corrosion and the morphology of pitting attack in relation to the effect of changing H_2S-CO_2 ratio and temperature.

The work presented in this paper is based on experiments on carbon steel exposed to different concentrations of H_2S (100, 1000, 10,000 and 100,000 ppm) in a pre-mixed H_2S-CO_2 gas system under ambient pressure at two temperatures; 30 and 80°C. In these experiments, *in-situ* electrochemical measurement of the transient electrochemical response is combined with an analysis of the corrosion product formed and the extent of pitting corrosion at the end of each experiment.

The authors appreciate the significant practical complexities of performing H_2S-based corrosion tests, especially in a closed experimental system. Some of the main complexities are usually associated with;

I. The instability and non-equilibrium concentration of active ionic species at the corrosion interface in the initial test period immediately after immersion of samples and before the system stabilizes

II. The continuous change in the water chemistry over the test duration. This is usually associated with the change in the kinetics of the corrosion and buffering effect over the course of the experiment.

While these complexities are well known within the research community, the authors have considered the merits of these results from this study within these experimental constraints.

Experimental Procedure

All experiments were conducted in a 3.5 wt.% NaCl solution at temperatures of 30°C and 80°C with emphasis on investigating corrosion kinetics and corrosion product formation, quantification of uniform corrosion rates and extent and morphology of pitting corrosion as a function of different H_2S-CO_2 gas ratios. The different pre-mixed gas phase composition of H_2S and CO_2 and measured bulk pH at the start of each experiment are provided in **Table 1.** It is important to note here that the pH of the test systems was not controlled throughout the experiment but allowed to evolve as the corrosion process occurred. The recorded pH in Table 1 represents the starting pH of the solution after 20-30 minutes of introduction of the H_2S pre-mixed gas and pH is stable. A stable pH is used here to adjudge significant shift from non-equilibrium concentration of dissolved species in the corrosion environment towards equilibrium. The pH of bulk solution was only measured and monitored for tests in 10% H_2S and 90% CO_2 and pure CO_2 at 30 and 80°C over 168 h, and are shown in Figure 1(a) and (b), respectively. Tests in CO_2 systems were conducted in this study as a reference to the different H_2S-CO_2 corrosion systems.

Materials: X65 carbon steel samples were used as the working electrodes within a three-electrode cell in every experiment. The steel was in a normalized form and possessed a ferritic/pearlitic microstructure. The nominal composition of X65 steel is provided in **Table 2.**

The carbon steel was sectioned into 10 mm x 10 mm x 5 mm samples. Wires were soldered to the back of each test specimen and then embedded in a non-conducting resin. Prior to the start of each experiment, test samples were wet-ground up to 1200 silicon carbide grit paper, degreased with acetone, rinsed with distilled water and dried with compressed air before immersion into the test brine. A surface area of 1 cm^2 was exposed to the electrolyte per sample and 5 samples were used per liter of solution.

Experimental setup and brine preparation: A 3.5 wt.% NaCl brine solution was used for all experiments. Sweet (CO_2) and sour (H_2S) corrosion experiments were conducted using two separate bubble cell systems, but with the same sample surface area to brine volume ratio of 5 cm^2 per 1 liter of test solution maintained at the start of all tests. CO_2 corrosion experiments were conducted in two separate vessels simultaneously with each filled with 2 liters of brine. The vessels were sealed with 10 samples immersed per vessel and CO_2 was bubbled into the test solution continuously to ensure saturation of the solution. H_2S corrosion experiments were also conducted in two separate vessels simultaneously with each vessel filled with 1 liter of brine and containing 5 samples to maintain a comparable surface area to volume ratio with CO_2 experiments. Pre-mixed gases of varying composition as provided in **Table 1** were bubbled into the test solution continuously to ensure complete saturation of the test solutions.

The test solution for pure CO_2 corrosion experiments was purged with CO_2 for a minimum of 12 h prior to starting each experiment to reduce oxygen concentration down to 20 ppb, simulating oilfield environments. Nitrogen (N_2) was used initially to purge the test solution for a minimum of 12 h for tests in H_2S-containing environments (H_2S-CO_2). Prior to commencement of electrochemical measurements for sour corrosion tests, samples were placed in the N_2-saturated brine solution, after which H_2S-containing gas mixtures were bubbled into the solution for 20-30 minutes until a stable starting pH was achieved. As previously mentioned in this paper, the authors are aware of the complexities in the overall corrosion behavior of the test samples especially in the early stages. However, this was considered insignificant relative to the long

experimental duration of 168 h, especially as it took only between ~0.3-0.5 h for pH to stabilize and electrochemical measurements started.

In-situ electrochemical measurements: Electrochemical measurements were conducted on two samples per test cell. Each sample formed the working electrode in a three-electrode cell which also comprised of an Ag/AgCl reference electrode and a platinum counter electrode. All electrochemical measurements were conducted with an ACM Gill 8 potentiostat[1]. Linear Polarization Resistance (LPR) measurements were performed by polarizing the working electrode every 15 mins from 15 mV below the open circuit potential (OCP) to 15 mV more positive than OCP at a scan rate of 0.25 mV/s to obtain a polarization resistance measurement (R_p). Tafel polarization measurements were performed at each experimental condition at the end of a separate 5 h LPR test to determine anodic and cathodic Tafel constants and ultimately the Stern-Geary coefficient values, which were subsequently used to estimate general corrosion rates. Scans always started at the OCP and extended +250 mV and –500 mV at a scan rate of 0.25 mV/s for anodic and cathodic sweeps, respectively. Both anodic and cathodic sweeps were performed on separate samples in the same test solution to ensure reliable measurements and the cathodic sweep was always performed first. **Table 3** indicates the measured Tafel constants and the resulting Stern-Geary coefficient for all test conditions. AC impedance measurements were also performed on each sample in order to determine the solution resistance. The solution resistance values and the associated Stern-Geary coefficient were used in conjunction with R_p and Faraday's Law to determine the *in-situ* corrosion rates as a function of time for the experimental conditions under investigation in this study. Potentiodynamic measurements were also corrected for IR drop.

Characterization of pitting corrosion damage: Surface profilometry was used in this study to evaluate pitting attack. Pit depth measurements were conducted in alignment with ASTM G46-94[2][15]. An NPFLEX 3D interferometer was used for obtaining the discrete geometry of pits on over 80% of the steel surface (the remaining 20% relates to scans at the perimeter of the sample which were excluded). Pits were identified based on carefully chosen thresholds with distinct pit depths, diameters and areas being quantified. ASTM G46-94 stipulates that an average of the 10 deepest pits and the size of deepest pit (based on relative pit depth measurement after removal of corrosion products) should be used for pit damage characterization for the sample. A systematic stitching approach is adopted whereby 9 different 3 x 3 mm^2 areas were analyzed to cover a sample surface area of 9 x 9 mm^2. Consequently, 3D images of regions where the deepest pits exist are identified on the sample surface with a high degree of accuracy and resolution.

Corrosion product identification: X-ray diffraction (XRD) patterns were performed using a Bruker D8[4] equipped with a LynxEye detector and a 90 position auto sampler, employing Cu Ka radiation with an active area of 1 cm^2 programmable di-vergence slits. Scans were performed over a range 2Θ = 10 to 70° using a step size of 0.033 per second, with a total scan time of approximately 50 minutes. The results were analyzed using X'Pert HighScore software and compared with individual crystal standards from the database.

Results and Discussion

Figure 2 shows the Tafel plots obtained after 5 h of immersion in each test solution. **Figure 2**(a) and (b) correspond to test environments at 30 and 80°C, respectively. Tafel polarization tests were carried out after monitoring the corrosion rates from LPR measurements for 5 h. At 30°C, the cathodic sweep for the pure CO_2 system in **Figure 2**(a) shows a limiting current in the potential range of -750 to -900 mV. This is attributed to the diffusion-limited current of both the reduction reactions of H^+[16] and the buffering effect associated with H_2CO_3 at the steel surface[1, 16]. Below -920 mV the charge-transfer process associated with the reduction of H_2O is observed. With the presence of 100 and 1000 ppm of H_2S in the pre-mixed H_2S-CO_2 gas system at 30°C, the potentiodynamic curve (both anodic and cathodic reaction lines) are shifted to the left, leading to a lower corrosion rate than in the pure CO_2 system. Comparable results have also been published by Zheng et al[1] at 30°C and after 2 h in a rotating cylinder electrode. From the shape of the curves in **Figure 2**, it is clear that reduction reactions of H^+ and the buffering effect from H_2CO_3 are still dominant and influencing the cathodic process at a low pH (~pH 4), at 30 and 80°C and at concentrations of 1000 ppm H_2S and below, despite the influence of the presence of H_2S.

At higher concentrations of H_2S (1% and 10% H_2S) at 30°C, the H_2O reduction reaction is delayed to higher (more negative) cathodic potentials. A similar effect is also evident at 80°C in **Figure 2**(b), albeit not as clear-cut as at 30°C. The potentiodynamic curves also indicate that at concentrations of 1% and 10% H_2S, the cathodic currents were higher than at concentrations of 100 and 1000 ppm H_2S. This was also observed to be the case for tests at 80°C as shown in **Figure 2(b).** However the cathodic reaction curves at 1% and 10% H_2S show an additional cathodic reaction at potential range of -740 to -940 mV, which is consistent with observations by Zheng et al [1, 3]. The increase in cathodic currents at high negative over-potentials with increasing H_2S content is a result of an increasing contribution from the "solid state" reaction of H_2S to the total cathodic reaction[1]. At 80°C and lower H_2S concentration, the curves of H_2S corrosion are similar in shape of that of CO_2 system due to the relative dominance of H^+/H_2CO_3 reduction reactions at this temperature[16].

A low corrosion rate can be extrapolated from **Figure 2(a)** at 100 ppm of H_2S at 30°C. This has been attributed to the formation an adsorbed monolayer of iron sulfide as proposed by Zheng et al[1] depending on the length of exposure time. The adsorbed and/or formed iron sulfide layer in this instance is believed to be capable altering the electric double layer of the corrosion interface and resulting in suppression of the kinetics of electrochemical reactions [1, 17].

Corrosion kinetics and corrosion product formation: Influence of H_2S concentrations at 30°C

The corrosion potential and corrosion rates for carbon steel samples exposed to pure CO_2 and all four H_2S-CO_2 gas combinations at 30°C over 168 h is presented in **Figure 3**(a) and (b), respectively. A stable corrosion potential and corrosion rate of ~-670 mV and ~1.7 mm/y, respectively, are observed towards the end of the experiment in the 100% CO_2 system. SEM images under these conditions are provided in **Figure 4(a)**.

[1] ACM Gill 8 is a trademark name
[2] American Society for Testing and Materials (ASTM); West Conshohocken, Pennsylvania, United States.
[3] Trade name
[4] Trade name

Similar observations in corrosion rate have already been discussed in previous publications [18, 19] and linked to the evolution of Fe_3C, followed by nano-scale crystals of $FeCO_3$ after extended immersion times. Comparing all plots in **Figure 3(**b), the corrosion rate in 100% CO_2 is clearly higher than the corrosion rates in all of the H_2S-containing systems over 168 h. These results also corroborate with the Tafel plots in **Figure 2**(a) based on 5 h tests and results for tests in H_2S gas between 100 and 500 ppm after 2 h by Zheng et al[1] at 30°C.

Referring to **Figure 3**(b), the corrosion rates were approximately equal within the first 50 h for tests in 100 ppm, 1% and 10% H_2S-containing gas systems, except for test in 1000 ppm of H_2S which recorded a slightly lower corrosion rate during the same time. Among the tests in H_2S-containing systems, tests with 100 ppm and 1% H_2S recorded the highest, stable corrosion rate at 30°C, while the test in 10% H_2S has its corrosion rate consistently reducing with time over 168 h. It is also interesting to note that the corrosion rate increases steadily with time for test in 1000 ppm of H_2S gas from a lower starting corrosion rate value of ~0.1 mm/yr than tests in 100 ppm, 1% and 10% H_2S-containing systems to similar corrosion rate for the test in 10% H_2S at ~0.2 mm/yr after 168 h. As stated previously, it is believed that at very low concentrations of H_2S (100 ppm), a thin iron sulfide layer forms via chemisorption[1] and/or adsorption onto the steel surface[20], especially at low temperatures[20]. It is still unclear why the corrosion rate at 1000 ppm of H_2S is slightly lower than other concentration levels.

The evidence from the SEM images in **Figure 4**(b) for the test at 100 ppm H_2S shows an inner FeS (mackinawite) film similar to that formed either via a "solid state" reaction or chemisorption. This is because the topography of the corrosion products is similar to that of the original polished steel surface (with evidence of polishing marks) even after 168 h [1, 4-6, 21]. The overall physical features observed in **Figure 4(b)** are also consistent with iron sulfide layers that show a combination of an inner nano-crystalline layer iron sulfide and localised deposits of FeS (mackinawite). As has been proposed by Shoesmith et al[4] and Smith[22], the presence of polishing marks on the iron sulfide layer formed after 168h for test in 100 ppm of H_2S system can be linked to FeS (mackinawite) formation by ""solid state" reaction. This is supported by similarities in the crystal cell dimensions of iron and mackinawite[23]. According to Rickard and Luther III[23], the Fe-Fe inter-atomic distance in a mackinawite crystal is 2.5967 Å, which is similar to (BCC) ferrite crystal at 2.86 Å. This makes a ferrite-rich surface an almost perfect template for the nucleation of mackinawite to retain the polishing marks of an uncorroded surface as shown in **Figure 4** (b). The crystalline form of iron sulfide shown in **Figure 4**(b) is driven by surface precipitation from a supersaturated corrosion interface, especially for a closed test system as is the case in this study[22]. The nano-crystalline form of iron sulfide is favored by the low concentration (100 ppm) of H_2S in the corrosion environment. The SEM images shown in **Figure 4(c)** for test in 1000 ppm of H_2S show a combination of nano-crystalline iron sulfide layer and "fluffy" iron sulfide with localized regions where Fe_3C is revealed and iron sulfide is absent. These features could indicate the formation and rupture of sheet-like structures of iron sulfide and the continuous nucleation of other morphologies of iron sulfide on top of initially formed iron sulfide layer. Such features are also consistent with the observations by Shoesmith et al[4]. The combination of a nano-crystalline inner layer and outer fluffy-like deposits of iron sulfide could also be linked to the transition from non-equilibrium to equilibrium concentration of dissolved H_2S species. A non-crystalline and sheet-like iron sulfide is also shown in **Figure 4(d)** for test in 1% of H_2S. However, the non-crystalline and sheet-like iron sulfide layer is adjacent to a localized cavity. The latter can be argued as a potential precursor to the evolution of pitting corrosion.

Generally, the iron sulfide corrosion product layer appears mainly as nano-crystalline in nature at low concentrations of H_2S (confirmed by the absence of any peaks for FeS (mackinawite) on XRD patterns at 100 and 1000 ppm H_2S as shown in **Figure 5**). The formation of iron sulfide has led to lower corrosion rate with respect to the measured corrosion rate in 100% CO_2 within the first 60 h[1]. The corrosion potential tends to drop towards more negative values of potential with increase in the amount of H_2S. A similar observation on corrosion potential and corrosion rate have been published for 100 ppm H_2S at 30°C by Choi et al[7]. It is believed that the formation of iron sulfide corrosion product as shown in **Figure 4(e)** for tests in 10% H_2S acts to protect the surface from uniform corrosion, which also suppresses the cathodic reaction and leading to a shift in the corrosion potential towards more negative potential. With 1% H_2S gas, the iron sulfide corrosion product layer is composed of identifiable mackinawite (as shown by XRD pattern in **Figure 5** and a nano-crystalline FeS layer as shown in **Figure 4**(d). It is understood that the variation in the corrosion profiles for these sour systems could be driven by the interfacial reaction of FeS (mackinawite) via the formation of an intermediate specie ($FeHS^+$) with H^+[4, 9] according to the reaction:

$$FeHS^+ + H_3O^+ \rightarrow Fe^{2+} + H_2S + H_2O \qquad (1)$$

The protectiveness of iron sulfide formed in 10% H_2S system is influenced by the mechanisms of its formation on both the steel surface-iron sulfide side and the iron sulfide-corrosion environment side of the corrosion interface. These are also influenced by the local supersaturation towards iron sulfide formation and the accompanying intermediate reactions. According to Tewari et al[9], such intermediate reactions could lead to either the diffusion of $FeHS^+$ away from the corrosion interface as Fe^{2+} or through the incorporation of $FeHS^+$ into a growing corrosion product layer on the steel surface as iron sulfide[9] depending on the system pH and H_2S content. However, the concept of intermediate species and their interaction with initially formed iron sulfide have not been investigated or proven in this study.

The starting pH of the corrosion systems in this study is between 3.9 and 4.4, making the reaction pathway in Equation 1 the most probable at the mackinawite/corrosion media interface [9, 11]. For tests in 10% H_2S, the corrosion rate is relatively constant for the first 60 h. Beyond the 60 h mark, the corrosion rate gradually reduces to a constant value, while the corrosion potential is also constant. In this case, it is believed that the reaction in Equation 1 still holds. However, iron sulfide formation kinetics in this case is influenced by both H_2S concentration and time in a closed system by the reaction [4, 11]:

$$FeHS^+ \rightarrow FeS + H^+S \qquad (2)$$

The closed experiment vessels and high concentration of H_2S can help to ensure that the rate at which the steel surface is corroding is less than the rate of iron sulfide formation, in favor of Equation 2. The competing processes described herein are considered to be the reason why the corrosion rate varies differently with time with different H_2S gas concentrations as presented in **Figure 3** and as shown by the different morphology of iron sulfide in **Figure 4**.

Corrosion kinetics and corrosion product formation: Influence of H_2S Concentrations at 80°C

The corrosion potential and corrosion rates over 168 h for carbon steel samples in CO_2 and all four different H_2S-CO_2 gas combinations at 80°C are presented in **Figure 6**(a) and (b), respectively. Referring to Figure **6**(a), the corrosion potential in the 100% CO_2 corrosion system became constant with the establishment of a semi-protective mixture of nano scale and larger crystals of $FeCO_3$ corrosion product. This is shown in **Figures 6**(a) (the poly-crystalline form of $FeCO_3$ is not physically visible in these figures but has been confirmed by XRD results presented in **Figure 8**). This form of corrosion product was observed to reduce the general corrosion rate from a peak of ~5.6 mm/y to a constant value of ~3.1 mm/y after 168 h as shown in **Figure 6** (b).

Referring to results from tests in H_2S-containing systems (**Figure 5**(a)), the corrosion potential is observed to be more negative at higher concentrations of H_2S (1 and 10%) than in pure CO_2 system. This is consistent with the observations of Morris et al[17] and linked to the effect of H_2S gas on the reversible potential of Fe. At lower concentrations of H_2S (100 and 1000 ppm), the corrosion potential is more positive than in pure CO_2 corrosion system from 0-60 h. Similar observations are also shown for tests at 30°C for H_2S concentrations at 100 and 1000 ppm (**Figure 3**(b)). Although the reason for such observations at low H_2S levels still remains evasive, initial inferences from this study has shown that this may be related to the mechanism of formation of iron sulfide at lower concentrations of H_2S, which may be distinctly different from the mechanism at higher concentrations of H_2S. This is clearly shown in **Figure 6**(a) as the corrosion potential increases quickly at 100 and 1000 ppm of H_2S and then starts dropping towards more negative potential after 60 h. This suggests a fast and unique process of iron sulfide formation when compared to tests in 1 and 10% H_2S. At 1 and 10% of H_2S, the corrosion potential in **Figure 6**(a) and corrosion rate in Figure 6(b) is shown to be different from that at 100 and 1000 ppm of H_2S, with the former (1 and 10% of H_2S) showing higher initial corrosion rate. This could be an indication of the distinct mechanism of iron sulfide formation (most likely via surface precipitation from the bulk solution) at these concentrations of H_2S. In a previous publication [24], it has been established that in 10% mixed H_2S-CO_2 corrosion environments, the presence of CO_2 usually manifests in the form of higher initial ferrite dissolution and hence higher initial corrosion rate. However, at high temperatures of 80°C, the kinetics of iron sulfide formation are enhanced such that a large proportion of Fe^{2+} lost into the solution is consumed for iron sufide formation. This was referred to as the synergistic effect of CO_2/H_2CO_3 induced corrosion process, H_2S and temperature on iron sulfide formation. It was shown that the thickness of iron sulfide film was higher in H_2S-CO_2 systems than in H_2S-N_2 corrosion systems[24]. At these concentrations of H_2S the relatively lower solubility of iron sulfide with reference to $FeCO_3$ for a H_2S-CO_2 system [25-27] makes it more likely for iron sulfide formation via surface precipitation from the bulk solution.

Referring to the corrosion rate data in **Figure 6**(b), it is evident that the presence of H_2S at all concentrations reduces the general corrosion rate from high values in a pure CO_2 system through the formation of different morphologies of iron sulfide, as shown in **Figure 7**(b)-(e). At 100 and 1000 ppm of H_2S, the corrosion rate remained approximately stable (after a slight initial decrease at 100 ppm and an initial increase at 1000 ppm of H_2S gas) over 168 h of exposure time with a mackinawite film detected at the end of the 168 h test (**Figure 7**(b) and (c) and **Figure 8**). It is believed that the initial decrease in corrosion rate at 100 ppm of H_2S is related to the process of iron sulfide formation via chemisorption and/or heterogeneous ("solid state") reduction of $H_2S_{(aq)}$, especially as this is occurring within the first 36 h of the experiments. This has been shown by other authors [1, 21] to be the dominant mechanism between 12 and 48 h. With a further increase in the H_2S content to 1% and 10%, the corrosion characteristics are significantly changed. Higher *initial* corrosion rates at 1% (~1.5 mm/y) and 10% H_2S (~2 mm/y) are observed compared to the 100 and 1000 ppm H_2S system (~1 mm/y) but these are still lower than pure CO_2 (>4 mm/y) at 80°C.

At higher concentrations of H_2S, the reduction of the general corrosion rate is more prominent at 10% H_2S than at 1% of H_2S and can be attributed to the nature and morphology of iron sulfide formed, as well as the most prominent mechanism of formation at the corrosion interface. It is believed that at these concentration levels of H_2S, the formation of iron sulfide is a combination of different mechanisms ("Solid state" reaction and/or via surface precipitation from the bulk solution) depending the exposure time. Evidence to support this transition has been reported in a recent publication[24] based on experiments after 7 and 168 h and is supported by other authors[1, 4, 22]. This is also related to the continuous interaction of the intermediate specie $FeHS^+$ with the environment [4, 11]. This has been shown in this study to be favored by a combination of high temperature and high H_2S content. A combination of higher initial corrosion rate and high temperature at high concentration of H_2S helps to promote a complex combination of iron sulfide formation mechanisms, resulting in a different morphology and chemistry of iron sulfide as shown in **Figure 7** d) and (e).

The process of formation of a mixture of iron sulfide films also coincides with an increase in corrosion potential which occurs earlier (after ~80 h) in 10% H_2S corrosion system than in 1% H_2S corrosion system (after ~140 h) to indicate the influence of H_2S content. While it has not been shown here how the thickness of iron sulfide corrosion layer varies with H_2S concentration, the SEM images presented in **Figure 7**(b)-(e) and XRD pattern in **Figure 8** shows the evidence of difference in morphology and composition of iron sulfide formed with increasing concentration of H_2S gas. Pyrrhotite was detected on the steel surface at 1 and 10% H_2S as shown by the XRD patterns[28] in **Figure 8**. Troilite have also been reported to have its strongest peak at similar positions as pyrrohtite[29]. However, based on the evidences of the hexagonal morphology of FeS see **Figure 7(f)**, it is believed that the iron sulfide specie shown by the XRD pattern in **Figure 8** is pyrrohtite[29]. It is unknown whether the ennoblement of the corrosion potential at high concentration of H_2S is due to pyrrhotite formation, however, it has been shown that the ennoblement and the reduction in corrosion rate observed at 10% H_2S as shown in **Figure 6**(a) and(b) is related to the process of iron sulfide precipitation and that the transition from mackinawite to pyrrhotite is accelerated by increased temperature and H_2S concentration[22], explaining the presence of pyrrhotite at 80°C as shown in **Figure 8**.

The observed trend in corrosion potential and corrosion rate with increasing H_2S concentration at 80°C could also be seen as an indication of the complexities related to the formation of FeS (mackinawite). According to Smith[22], such complexities could be associated with the competing phenomenon of mackinawite dissolution and iron sulfide formation via surface precipitation. This could lead to either an increase or reduction in corrosion rate depending on which phenomenon dominates the corrosion process. Smith[22] also concluded that the final outcome of the competing processes is also controlled by temperature and H_2S concentration. Bulk pH was also considered to be very influential [4, 11].

It is believed that the continuous interaction between initially formed mackinawite and the corrosive environment leads to the development of iron sulfide onto the initially formed (FeS) mackinawite either as a

different morphology of mackinawite or other more stable forms of FeS such as pyrrhotite with increasing temperature, H_2S concentration[22] and pH[4, 11]. This is clearly depicted in the corrosion rate behavior in **Figure 6**(b) and shown by the SEM images in **Figure 7**(b), (c), (d), and (e) and the XRD pattern in **Figure 8**. Therefore the reverse is expected with decreasing temperature, H_2S content and pH such that the corrosion interface acts in such a way that the competing phenomenon keeps the corrosion rate constant or increased as shown in **Figure 3**(b) at 30°C. At 100 and 1000 ppm of H_2S gas, the corrosion rate was kept constant while the corrosion product formed were a mixture of different forms of iron sulfide. This therefore shows that the electrochemical process that is represented by changes in corrosion potential, corrosion rate and properties of iron sulfide film in this study is strongly linked to the competing processes of dissolution of initially formed FeS (mackinawite) and formation of other forms iron sulfide via surface precipitation.

It is clear from the results discussed thus far that the presence of H_2S in the corrosion environment could protect against uniform corrosion in reference to pure CO_2 corrosion due to the formation of iron sulfide corrosion products. However, this does not necessarily mean that other potential mechanisms of corrosion damage such as pitting corrosion are also mitigated against. This implies that a more comprehensive assessment to understand the true effect of these competing processes and the different mechanisms associated with H_2S-corrosion will require further research effort. Further discussions on the observed implications of the variation of the corrosion characteristics of carbon steel in different H_2S-CO_2 corrosion environment is presented in later sections of this paper.

Pitting corrosion characteristics at 30°C

Figure 9 presents data from the characterization of pitting corrosion damage on carbon steel exposed to different sour corrosion environments for 168 h at 30°C. Pit initiation on carbon steel in CO_2 corrosion environment has been characterized as a random phenomenon associated with the transition from general corrosion to pitting corrosion[30]. A combination of ferrite dissolution and the revealing of a Fe_3C layer have been shown to be a contributing factor towards the evolution of pitting corrosion in a low pH CO_2 saturated corrosion environment [30, 31]. The formation of a non-protective and/or semi-protective corrosion film has been shown to sustain pit growth up to ~22 µm (as the deepest pit) over 168 h as shown in **Figure 9.** This is supported by evidence of electrochemical characteristics **(Figure 3(b))**, nature of corrosion product **(Figure 4(a)),** and size of deepest pit **(Figure 9).** The morphology of pitting attack pure CO_2 environment after 168 h is observed in this study to be broad-diameter pits as shown in **Figure 10(a)**. It is also important to note that there is no confirmation on whether these pits will continue to grow beyond 168 h. One of the other unique features of the evolution of pitting corrosion in pure CO_2 corrosion system is the significant contribution of uniform corrosion to overall material loss. This has already been established in a previous publication[19].

The results of the size of the deepest pit (relative to corroded surface) in **Figure 9** show that the test in 100 ppm of H_2S recorded the shallowest pits after 168 h at 30°C. The size of the deepest pit tends to increase with increasing H_2S content after 168 h. In the CO_2 corrosion environment, the pit morphology is shown to be open and large diameter which is consistent with pit morphology in CO_2 systems and 10 wt.% NaCl solution from separate tests from a previous publication [19]. Interestingly, with increasing concentration of H_2S from 100 ppm to 1% and then 10%, the morphology of measured pits and corrosion damage on the surface changes from narrow pits with very small diameters (typically micro-pits); surrounded by a large un-corroded regions to pits surrounded by areas of localized-uniform attack (referring to **Figure 10 (b)-(d)**). At 10% H_2S, it is also evident that the size of deepest pit only increased marginally from the measured size of deepest pit in 1% of H_2S.

The iron sulfide formed at 1000 ppm of H_2S gas is able to protect the steel surface from uniform corrosion especially in the initial stages of the corrosion process (See **Figure 3(b)**). This is supported by the estimate of the thickness loss to uniform corrosion (based on linear polarization measurements) in **Figure 9**. The formation of iron sulfide at 1000 ppm of H_2S coincided with a marginal increase in size of measured deepest pit from a value of ~19 µm at 100 ppm of H_2S gas to ~24 µm. At 100 ppm of H_2S gas, the uniform corrosion rate remains constant but higher than at 1000 ppm of H_2S gas. The lower size of deepest pit at 100 ppm of H_2S than 1000 ppm of H_2S is likely due to the unique nature and properties of the iron sulfide film at 100 ppm of H_2S gas as shown in **Figure 4** (b) and how it interacts electrochemically with both sides of the its interface. Above 1000 ppm of H_2S, the size of deepest pit only increased slightly at 10% of H_2S. The relative contribution of uniform corrosion and the associated iron sulfide formation mechanism is believed to have influenced the evolution of unique morphologies of pitting attack with changes in H_2S concentration as presented in **Figure 9**. This also indicates a relationship between the continuous evolution of, and extent of pitting corrosion with the nature of and mechanism by which iron sulfide is formed. At 1% and 10% H_2S, the pits are surrounded by areas that have experienced *localized-uniform* corrosion attack as shown in **Figure 10**. This is an indication of a combination of high initial loss of Fe^{2+} (**Figure 3(b)**) and continuous ferrite dissolution across an electronically conductive iron sulfide film. This also implies that at high concentration of H_2S, continuous ferrite dissolution may be providing the interface with needed ions for a potentially more complex process of iron sulfide formation to support more pitting corrosion attack.

Pitting corrosion characteristics at 80°C

Figure 11 provides summary data on the pitting corrosion characteristics of carbon steel with changing H_2S gas concentration at 80°C. It shows that the size of the deepest pit is higher in the presence of 100 ppm and 10% H_2S when compared to the size of deepest pit in the pure CO_2 environment. However, the size of deepest pit in 1000 ppm and 1% H_2S is observed to be almost similar to the size of deepest pit in pure CO_2 environment. Referring to **Figure 12**, the morphology of pitting corrosion attack is observed to be changing from narrow diameter pits in 100 ppm of H_2S system to heavy pitting corrosion attack in 10% H_2S. The change in the morphology of pitting attack with changing H_2S concentration is more apparent than at 30°C. Coincidentally, the transition in morphology of attack correlates with the concentration range of H_2S gas (1000 ppm and 1% of H_2S gas) that also recorded the lowest size of deepest pit. This represents an indication of an intermediate transition concentration range at 80°C within which the morphology of pitting attack changes from having deep and narrow diameter pits to a severely pitted surface.

The progress of pitting corrosion in carbon steel is believed to be significantly influenced by the magnitude of the galvanic driving force induced by the formation of iron sulfide corrosion products. Referring to **Figure 6**(a) and in comparison to **Figure 3**(a), there is an observed increase in corrosion potential by ~70mV at 80°C in 10% H_2S system. This is far more noticeable than at 30°C, where there was no observable change. While this change in corrosion potential represents the

corrosion behavior of the entire corroding surface, it is believed that this could also be an indication of development of local galvanic cells between distinct anodic and cathodic sites (referring to exposed surface of the steel and iron sulfide film covered areas, respectively). However, these data do not show the local galvanic cells that could be driving the pitting corrosion process. While this has not yet been proven in this study, Han et al[32] indicated from their study that a change in corrosion potential between bare and corrosion film covered surface of 20-30 mV led to the development of galvanic effects for a CO_2 system. In this study, evidence of deep pits at 80°C in 10% H_2S corrosion environment coincide with an increase in potential by ~70mV compared to other test environments. This observation correlates with Han et al[32] observations and suggests similar effects may occur in H_2S systems.

Figure 6(a) presents evidence of the occurrence of ennoblement of the corroding surface, albeit to varying degree with increasing in H_2S content, most notably at 1 and 10% H_2S gas. It is also believed that a change in the overall potential of a corroding surface of such magnitude of between 20 and 70 mV (for test in 1 and 10% of H_2S) could indicate the existence of local galvanic cells capable of supporting the progress of pitting corrosion[32]. The slight increase in potential towards the end of the test in 1% of H_2S suggests that with extended experiment time, there may be enhanced ennoblement of the steel surface at this concentration. While electrochemical measurements related to these local galvanic cells have not been made or confirmed in this study, pitting corrosion data in **Figure 11** and **Figure 12** has shown a good correlation between the formation of iron sulfide (and H_2S content), changes in corrosion potential and size of pit depth.

An intermediate concentration of 1000 ppm and 1% H_2S is shown in **Figure 11** to promote the transition from deep and narrow pits or micro pits to severe pitting corrosion at 80˚C. Evidence of the different morphology of pitting corrosion attack is shown by the 3D images of pitted surfaces of carbon steel exposed to pure CO_2, 1000 ppm and 10% H_2S corrosion system in **Figure 12**. Based on a combination of these observations and previous statement on potential local galvanic cells, it can be argued that that pitting corrosion is driven by the galvanic effect associated with the mechanism of formation of iron sulfide and changes its nature and morphology. This is confirmed by the corrosion rate data (**Figure 6**), corrosion product formed (see **Figure 7**(a)-(e) and the extent and morphology of pitting attack at 10% H_2S in **Figure 12**.

Between 100 ppm and 1% H_2S, the transition from narrow diameter pits to shallower pits (but with higher uniform corrosion) may be related to the interaction caused by the competing processes of iron sulfide dissolution and precipitation as discussed earlier. Such interaction often leads to loss of Fe^{2+} and increase in uniform corrosion rate depending on the H_2S content and temperature. At 10% H_2S, the build-up of the iron sulfide film and the likely transition from mackinawite to pyrrhotite resulted in significant ennoblement of the steel (up to ~70mV of change in potential as shown in **Figure 6**(a)) and leading to a severe form of pitting attack.

The transition in morphology of pitting attack (between 1000 ppm and 1% of H_2S) could also be influenced by the changes in iron sulfide formation process and the masking effect of higher uniform corrosion surrounding the pits formed in comparison to test at 100 ppm of H_2S. The transition also confirms the initial suggestion that a change in the formation of iron sulfide from mainly adsorption and/or chemisorption to surface precipitation from bulk solution with increasing exposure time is usually preceded by some form of ferrite dissolution (driven by the interaction of intermediate species ($FeHS^+$) with the corrosion media). This could also be the reason for the manifestation of localized-uniform corrosion attack surrounding some growing pits. This process is favored by an increase in H_2S concentration and temperature.

In the context of the evolution of pitting corrosion in H_2S-containing systems, it believed that the initial stages of the corrosion process is critical to the nucleation of local anodic sites and initiation of pitting corrosion[30]. It helps to define the distribution of anodic and cathodic sites, with Fe_3C rich regions becoming the most favorable sites for the precipitation of iron sulfide corrosion products [27, 30]. This scenario is capable of inducing local galvanic cells across the surface of the steel especially when there is the likelihood that cathodic reactions will be supported by the conductive nature of specific iron sulfide corrosion products[11, 33] after its initial formation. In the case of tests at 80°C, the kinetics of iron sulfide formation is significantly enhanced. The emergence of Local anodic sites across the steel surface is also known to be stochastic in such corrosion systems. Thus, it is believed that the formed iron sulfide corrosion product electrochemically interacts with the steel surface to undermine these local anodes and manifest as pits and/or micropits. This is clearly evident from the summary of pitting corrosion characteristics of carbon steel in H_2S-containing systems provided in **Figure 9** and **Figure 11.**

The SEM images in **Figure 4, Figure 7** and the 3D images of sizes of deepest pits in **Figure 10** and **Figure 12** have shown that once pits are initiated, the extent of pit growth and the morphology of the attack after a certain exposure time is dependent on the nature of iron sulfide formed and the influencing environmental parameters such as changes in H_2S concentration and temperature. As already described in the previous section of this paper, the interaction and thus possible oxidation of complexed intermediate species ($(FeHS)^+_{ad}$) can drive local ferrite dissolution[11]. This is because cathodic regions in a local galvanic cell will have a higher pH[30] which promotes the conversion of species ($(FeHS)^+_{ad}$) to iron sulfide, while anodic regions of the local galvanic cells will have low pH to promote the conversion of species ($(FeHS)^+_{ad}$) to Fe^{2+} [4, 11, 27, 30]. The manner in which iron sulfide films develop significantly influences the level of protection offered as well as its stability and dissolution kinetics. In addition, the contribution of the solid state reaction and aqueous reduction of H_2S as well as its continuous interaction of initially formed FeS (mackinawite) with the corrosion media further complicates the corrosion process. It is believed that these reactions can also play a significant role in the overall pitting corrosion process at higher H_2S contents. All these processes contribute towards the extent of pitting corrosion observed on the steel surface at different H_2S content and temperature from this study. As shown in **Figure 3**(b) and **Figure 6**(b) for 30 and 80°C respectively, the continuous reduction in corrosion rate at 10% H_2S also means that the iron sulfide corrosion layer formed at higher concentration levels of H_2S at both temperatures is capable of limiting the dominance of ferrite dissolution (in the form of uniform corrosion) as well as ensuring only the competition of iron sulfide formation and dissolution defines the pitting and uniform corrosion characteristics of the exposed steel.

Conclusions

The overall corrosion characteristics of X65 carbon steel in different H_2S-CO_2 gas system has been investigated at 30 and 80°C with reference to a pure CO_2 corrosion environment. The following conclusions were deduced from the results of this work.

- The mechanism of H_2S corrosion and iron sulfide film formation in H_2S-CO_2 corrosion system is very complex and differs with H_2S concentration and temperature. This study has provided

experimental data to show to some extent that there was a continuous interaction of the steel surface under the initial iron sulfide layer with the corrosive environment. This is shown to manifest in terms of different corrosion damage mechanisms, formation of different morphologies of the same type of iron sulfide and other polymorphs of iron sulfide.

- The overall corrosion damage mechanism (uniform and/or pitting corrosion) of carbon steel materials exposed to different concentration of H_2S in mixed H_2S-CO_2 gas system is driven by the characteristic mechanism of H_2S corrosion and iron sulfide formation. High temperatures and H_2S concentrations promotes the formation of different forms and morphology of iron sulfide, such as "fluffy" mackinawite and pyrrhotite by surface precipitation from bulk solution and electrochemical interaction at the iron sulfide film/bulk solution interface. Low temperatures and H_2S concentrations promotes the formation of mackinawite mainly via heterogeneous reactions at the corrosion interface.

- Pitting corrosion attack is shown from this study to correlate with the evolution of different morphologies and physiochemical properties of iron sulfide formed at different H_2S content and temperature. Pitting corrosion attack increases with increase in temperature and H_2S content and is related to the nature of and mechanism of formation of iron sulfide formed in these conditions.

- The morphology of pitting corrosion attack is shown in this study to change with concentration of H_2S at specific temperatures. Pitting and/or localized attack changes from small diameter and narrow pits to severe pitting attack with increase in H_2S concentration at 80°C. The critical concentration threshold for this transition is shown in this study to reduce with increasing temperature.

References

1. Y. Zheng, J. Ning, B. Brown, and S. Nešić, "Electrochemical Model of Mild Steel Corrosion in a Mixed H2S/CO2 Aqueous Environment in the Absence of Protective Corrosion Product Layers", Corrosion, 71, 3 (2015): p. 316-325.
2. M. Singer, B. Brown, A. Camacho, and S. Nešić, "Combined effect of carbon dioxide, hydrogen sulfide, and acetic acid on bottom-of-the-line corrosion", Corrosion, 67, 1 (2011): p. 015004-1-015004-16.
3. Y. Zheng, B. Brown, and S. Nešić, "Electrochemical study and modelling of H2S corrosion of mild steel", Corrosion, 70, 4 (2013): p. 351-365.
4. D.W. Shoesmith, P. Taylor, M.G. Bailey, and D.G. Owen, "The Formation of Ferrous Monosulfide Polymorphs during the Corrosion of Iron by Aqueous Hydrogen Sulfide at 21°C", Journal of The Electrochemical Society, 127, 5 (1980): p. 1007-1015.
5. H. Ma, X. Cheng, G. Li, S. Chen, Z. Quan, S. Zhao, and L. Niu, "The influence of hydrogen sulfide on corrosion of iron under different conditions", Corrosion Science, 42, 10 (2000): p. 1669-1683.
6. J. Kittel, F. Ropital, F. Grosjean, E.M.M. Sutter, and B. Tribollet, "Corrosion mechanisms in aqueous solutions containing dissolved H2S. Part 1: Characterisation of H2S reduction on a 316L rotating disc electrode", Corrosion Science, 66, (2013): p. 324-329.
7. Y.-S. Choi, S. Nesic, and S. Ling, "Effect of H2S on the CO2 corrosion of carbon steel in acidic solutions", Electrochimica Acta, 56, 4 (2011): p. 1752-1760.
8. B. Brown and S. Nesic. "Aspects of localized corrosion in an H2S-CO2 environment", CORROSION, paper no. 1559, (Salt Lake City, UT.: NACE International, Houston, Texas, 2012).
9. P.H. Tewari and A.B. Campbell, "Dissolution of iron during the initial corrosion of carbon steel in aqueous H2S solutions", Canadian Journal of Chemistry, 57, 2 (1979): p. 188-196.
10. J. Tang, Y. Shao, J. Guo, T. Zhang, G. Meng, and F. Wang, "The effect of H2S concentration on the corrosion behavior of carbon steel at 90°C", Corrosion Science, 52, 6 (2010): p. 2050-2058.
11. H.-H. Huang, W.-T. Tsai, and J.-T. Lee, "Corrosion morphology of A516 carbon steel in H2S solution", Scripta Metallurgica et Materialia, 31, 7 (1994): p. 825-828.
12. A.G. Wikjord, T.E. Rummery, F.E. Doern, and D.G. Owen, "Corrosion and deposition during the exposure of carbon steel to hydrogen sulphide-water solutions", Corrosion Science, 20, 5 (1980): p. 651-671.
13. Y. Zheng, J. Ning, B. Brown, and S. Nešić, "Electrochemical model of mild steel in a mixed H2S-CO2 aqueous environment in the absence of protective corrosion product layers", Corrosion, (2014): p. 316-325.
14. J. Ning, Y. Zheng, B. Brown, D. Young, and S. Nešić, "The Role of Iron Sulfide Polymorphism in Localized H2S Corrosion of Mild Steel", CORROSION, 73, 2 (2017): p. 155-168.
15. ASTM Standard G46-94, Standard guide for examination and evaluation of pitting corrosion. ASTM International: West Conshohocken, PA, 2003.
16. S. Nesic, J. Postlethwaite, and S. Olsen, "An electrochemical model for prediction of corrosion of mild steel in aqueous carbon dioxide solutions", Corrosion, 52, 04 (1996): p. 280-294.
17. D.R. Morris, L.P. Sampaleanu, and D.N. Veysey, "The Corrosion of Steel by Aqueous Solutions of Hydrogen Sulfide", Journal of The Electrochemical Society, 127, 6 (1980): p. 1228-1235.
18. F. Pessu, R. Barker, and A. Neville, "The Influence of pH on Localized Corrosion Behavior of X65 Carbon Steel in CO2-Saturated Brines", Corrosion, 71, 12 (2015): p. 1452-1466.
19. F. Pessu, R. Barker, and A. Neville, "Understanding Pitting Corrosion Behavior of X65 Carbon Steel in CO2-Saturated Environments: The Temperature Effect", Corrosion, 72, 1 (2015): p. 78-94.
20. P. Marcus and E. Protopopoff, "Potential - pH Diagrams for Adsorbed Species: Application to Sulfur Adsorbed on Iron in Water at 25° and 300° C", Journal of The Electrochemical Society, 137, 9 (1990): p. 2709-2712.
21. R.C. Woollam, J.R. Vera, C. Mendez, A. Huggins, and W.H. Durnie. "Localized corrosion due to galvanic coupling between FeS-covered and uncovered areas: Another oilfield myth?", CORROSION, paper no. 2715, (Orlando: FL.: NACE International, Houston, Texas, 2013).
22. S.N. Smith. "Current understanding of corrosion mechanisms due to H2S in oil and gas production environments", CORROSION, Paper no. 5485, (Dallas, TX: NACE International 2015, 2015).
23. D. Rickard and G.W. Luther, "Chemistry of Iron Sulfides", Chemical Reviews, 107, 2 (2007): p. 514-562.

24. F. Pessu, R. Barker, and A. Neville, "Pitting and Uniform Corrosion of X65 Carbon Steel in Sour Corrosion Environments: The Influence of CO2, H2S, and Temperature", CORROSION, 73, 9 (2017): p. 1168-1183.
25. C.A.R. Silva, X. Liu, and F.J. Millero, "Solubility of Siderite (FeCO3) in NaCl Solutions", Journal of Solution Chemistry, 31, 2 (2002): p. 97-108.
26. W. Davison, "The solubility of iron sulphides in synthetic and natural waters at ambient temperature", Aquatic Sciences, 53, 4 (1991): p. 309-329.
27. B.M. Kermani and A. Morshed, "Carbon dioxide corrosion in oil and gas production: A compendium", Corrosion, 59, 08 (2003): p. 659-683.
28. F. Xu and A. Navrotsky, "Enthalpies of formation of pyrrhotite Fe1-0.125xS (0 <= x <= 1) solid solutions", American Mineralogist, 95, 5-6 (2010): p. 717-723.
29. N. Alsén, "Radiographic analysis of the crystal structures of magnetic grains, breithauptite, pentlandite, millerite and related compounds", Geologiska Föreningen i Stockholm Förhandlingar, 47, 1 (1925): p. 19-72.
30. J.L. Crolet, N. Thevenot, and S. Nesic, "Role of Conductive Corrosion Products in the Protectiveness of Corrosion Layers", Corrosion, 54, 3 (1998): p. 194-203.
31. F. Farelas, M. Galicia, B. Brown, S. Nesic, and H. Castaneda, "Evolution of dissolution processes at the interface of carbon steel corroding in a CO2 environment studied by EIS", Corrosion Science, 52, 2 (2010): p. 509-517.
32. J. Han, B.N. Brown, and S. Nešić, "Investigation of the galvanic mechanism for localized carbon dioxide corrosion propagation using the artificial pit technique", Corrosion, 66, 9 (2010): p. 12.
33. J. Kvarekval. "Morphology of localised corrosion attacks in sour environments", CORROSION, (Nashville, TN.: NACE International, Houston, Texas, 2007).

FIGURE CAPTIONS

Figure 1: Measured in-situ pH of corrosion media under two different gas atmospheres at (a) 30℃ and (b) 80℃, over 168 hours

Figure 2: Tafel polarization plots for X65 carbon steel in 3.5 wt. % NaCl solutions saturated with different combination of H_2S and CO_2 gas at (a) 30℃ and (b) 80℃ after 5 hours exposure.

Figure 3: Graphs of (a) corrosion potential and (b) corrosion rate of X65 carbon steel in 3.5 wt.% NaCl solution under different combination of H_2S-CO_2 gas at 30℃ over 168 hours.

Figure 4: SEM images of corrosion product layer on X65 carbon steel in 3.5 wt. % NaCl solution under different combinations of H_2S-CO_2 gas;(a) 100 mol.% CO2 , (b) 100 ppm of H_2S gas, (c) 1000 ppm of H_2S gas, (d) 1% of H_2S gas (e) 10% of H_2S gas at 30℃ and after 168 h.

Figure 5: XRD patterns for corrosion products formed on X65 carbon steel in 3.5 wt. % NaCl solution under different combinations of H_2S-CO_2 gas at 30℃ after 168 h.

Figure 6: Graphs of (a) corrosion potential and (b) corrosion rate of X65 carbon steel in 3.5 wt. % NaCl solution under different combination of H_2S-CO_2 gas at 80℃, over 168 h.

Figure 7: SEM images of corrosion product layer on X65 carbon steel in 3.5 wt. % NaCl solution under different combinations of H_2S-CO_2 gas;(a) 100 mol.% CO_2 , (b) 100 ppm of H_2S gas, (c) 1000 ppm of H_2S gas, (d) 1% of H_2S gas (e) 10% of H_2S gas at 80℃ and after 168 h.

Figure 8: XRD patterns for corrosion products formed on X65 carbon steel in 3.5 wt. % NaCl solution under different combinations of H_2S-CO_2 gas at 80℃ after 168 h.

Figure 9: Contribution of thickness loss to uniform corrosion and pit depths (relative to corroded surface) of X65 carbon steel in 3.5 wt. % NaCl solution under exposed to different combination of H_2S-CO_2 gas at 30℃ for 168 h.

Figure 10: 3D images of pitting corrosion damage on carbon steel surface exposed to (a) pure CO_2, (b) 100 ppm of H_2S, (c) 1000 ppm of H_2S and (d) 10% of H_2S corrosion system after 168 hours at 30℃.

Figure 11: Contribution of thickness loss to uniform corrosion and pit depths (relative to corroded surface) of X65 carbon steel in 3.5 wt. % NaCl solution under exposed to different combination of H_2S-CO_2 gas at 80℃ for 168 hours.

Figure 12: 3D images of pitting corrosion damage on carbon steel surface exposed to a) pure CO_2, (b) 1000 ppm of H_2S and (c) 10% of H_2S corrosion system after 168 h at 80℃.

TABLES

Table 1: Pre-mixed gas phase composition of H_2S and CO_2 gas and the bulk pH at the start of experiment at 30 and 80℃ based and room pressure.

Approx. gas phase conc. of H_2S in ppm	Partial pressure of H_2S (bar)	CO_2 (mol. %)	pH at 30°C	pH at 80°C
0	0.00	Balance	~3.80	~3.90
100	~1.00 X 10^{-4}	Balance	~4.00	~4.00
1000	~1.00 X 10^{-3}	Balance	~4.00	~4.10
10000	~ 0.01	Balance	~4.10	~4.20
100000	~0.10	Balance	~4.40	~4.30

Table 2: X65 Carbon steel elemental composition (wt. %)

C	Si	P	S	Mo	Mn	Ni	Nb	V	Fe
0.15	0.22	0.023	0.002	0.17	1.42	0.09	0.05	0.06	97.81

Table 3: Tafel constants at different temperatures for wet-ground X65 steel exposed to a 3.5 wt. % NaCl CO_2-saturated solution.

Temperature (℃)	Gas Content	β_a	β_c	B
30	0 ppm of H_2S (100% CO_2)	32.5	200.0	12.1
	100 ppm H_2S	50.0	115.0	15.1
	1000 ppm of H_2S	60	140	18.2
	1% of H_2S	55.0	120.0	16.4
	10% of H_2S	55.0	110.0	16.0
80	100% CO_2	57.5	135.0	17.5

	100 ppm H_2S	50.0	110.0	15.0
	1000 ppm of H_2S	60	120	17.4
	1% of H_2S	65.0	120.0	18.3
	10% of H_2S	57.5	160.0	18.4

***β_a and β_c in unit of mV/decade,** *B is Stern-Geary coefficient (mV/decade)

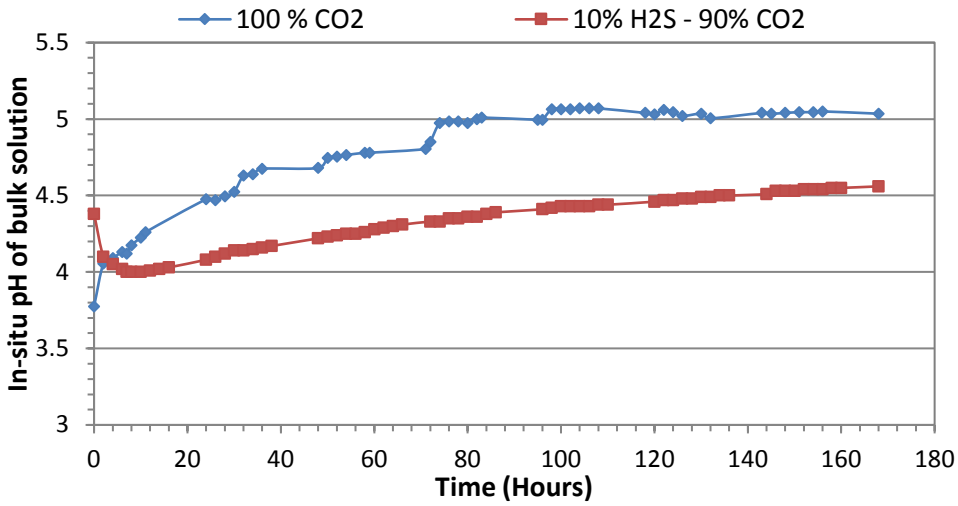

A

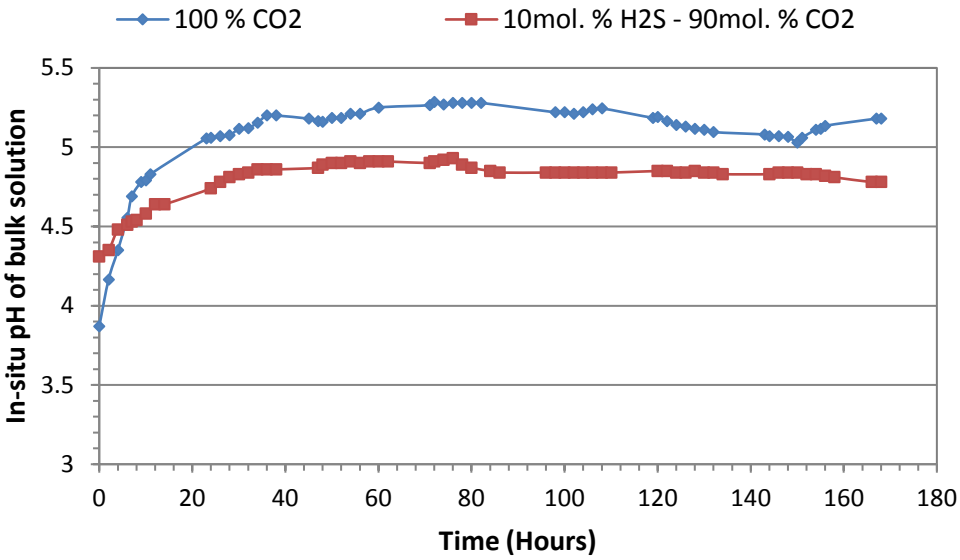

B

Figure 1: Measured *in-situ* pH of corrosion media under two different gas atmospheres at (a) 30°C and (b) 80°C, over 168 hours.

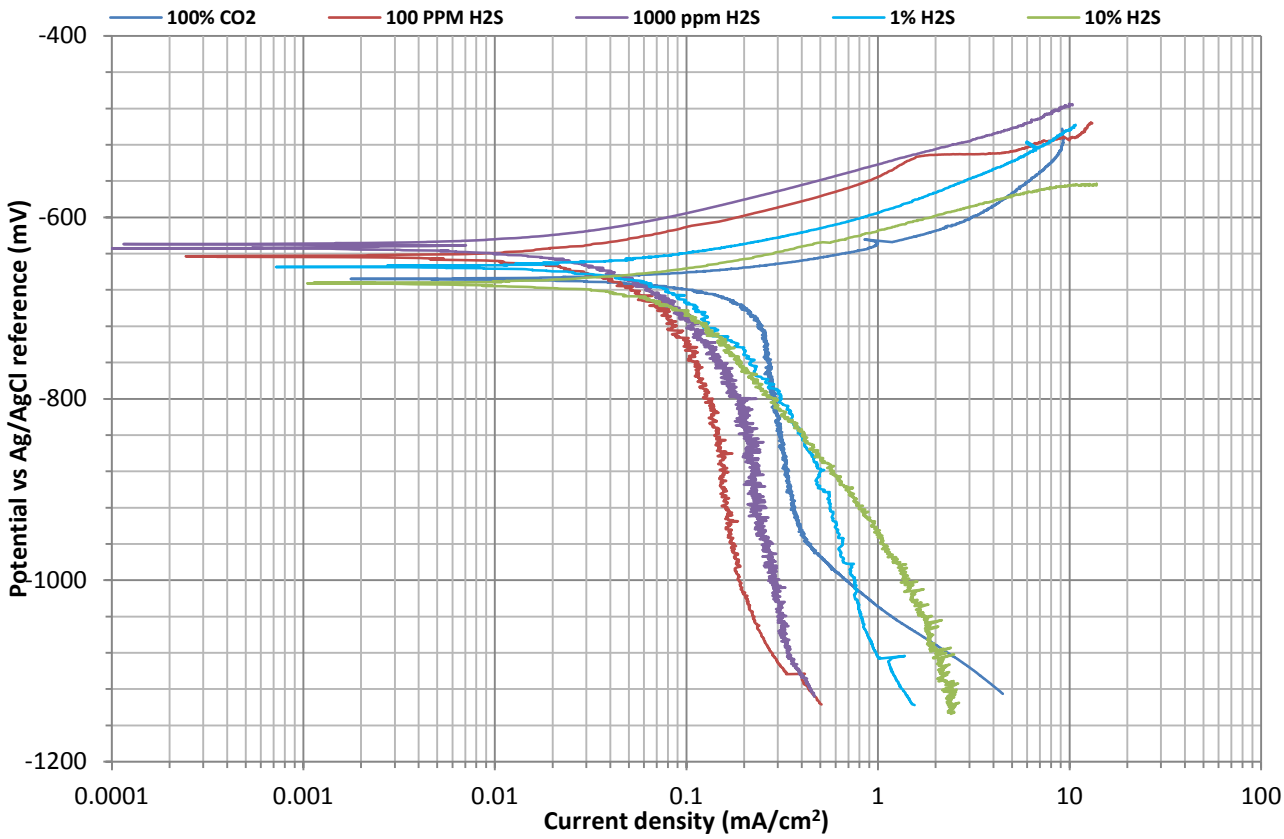

A

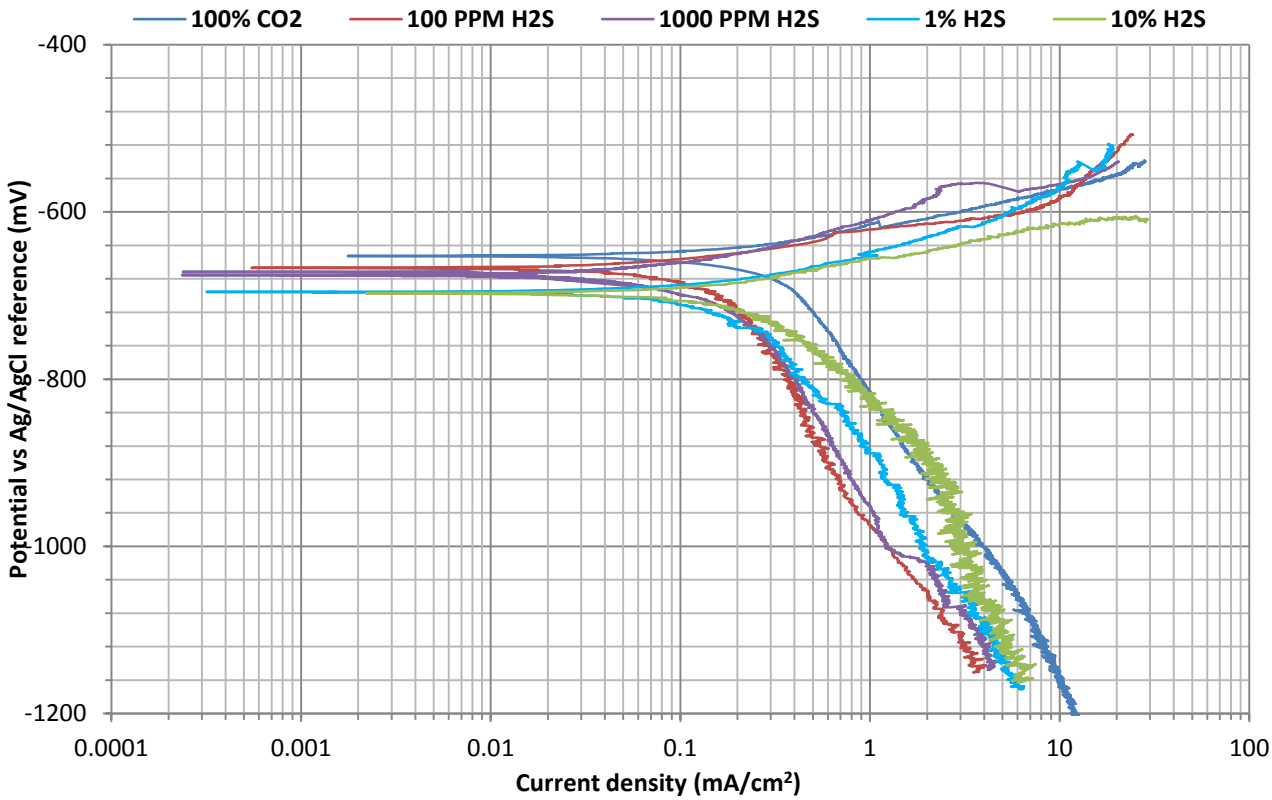

B

Figure 2: Tafel polarization plots for X65 carbon steel in 3.5 wt. % NaCl solutions saturated with different combination of H_2S and CO_2 gas at (a) 30°C and (b) 80°C after 5 hours exposure.

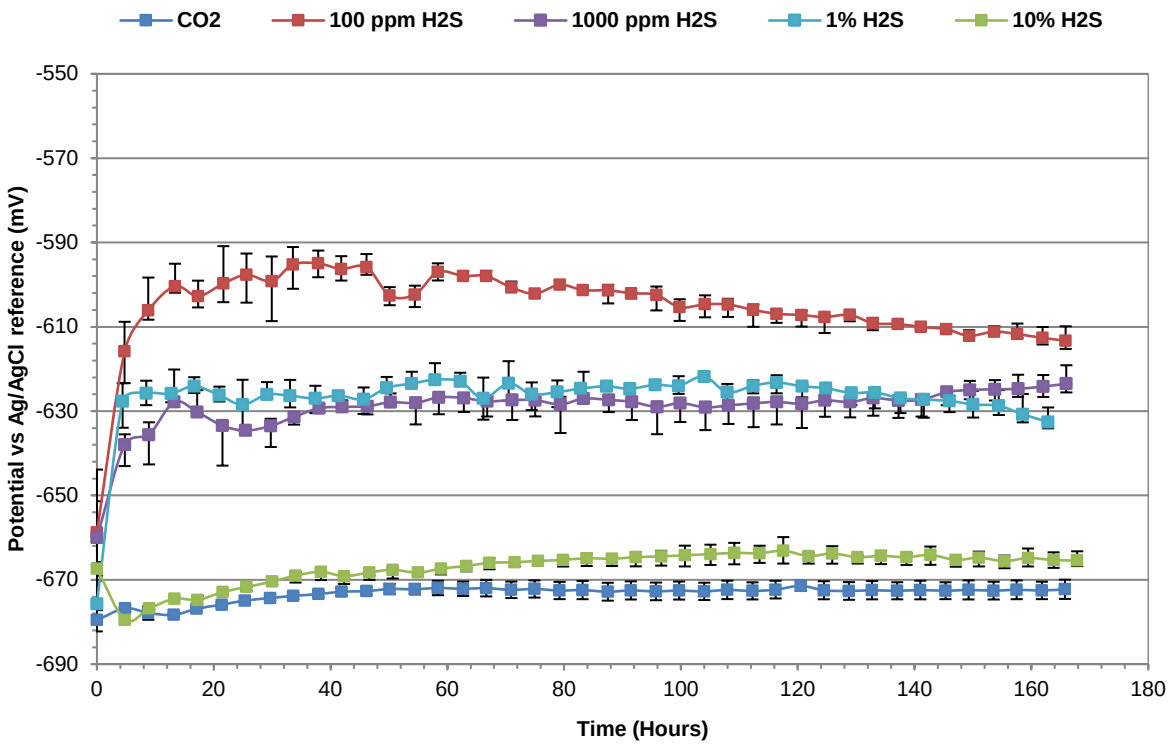

A

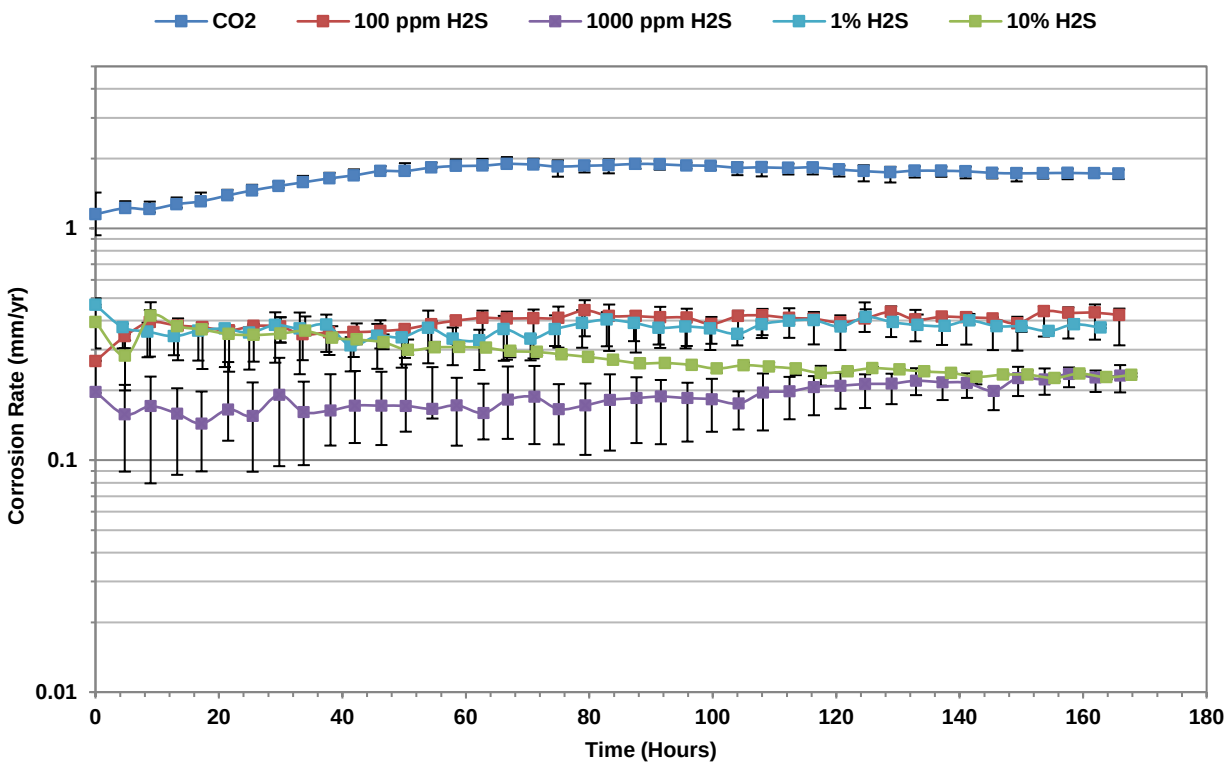

B

Figure 3: Graphs of (a) corrosion potential and (b) corrosion rate of X65 carbon steel in 3.5 wt.% NaCl solution under different combination of H_2S-CO_2 gas at 30℃ over 168 hours.

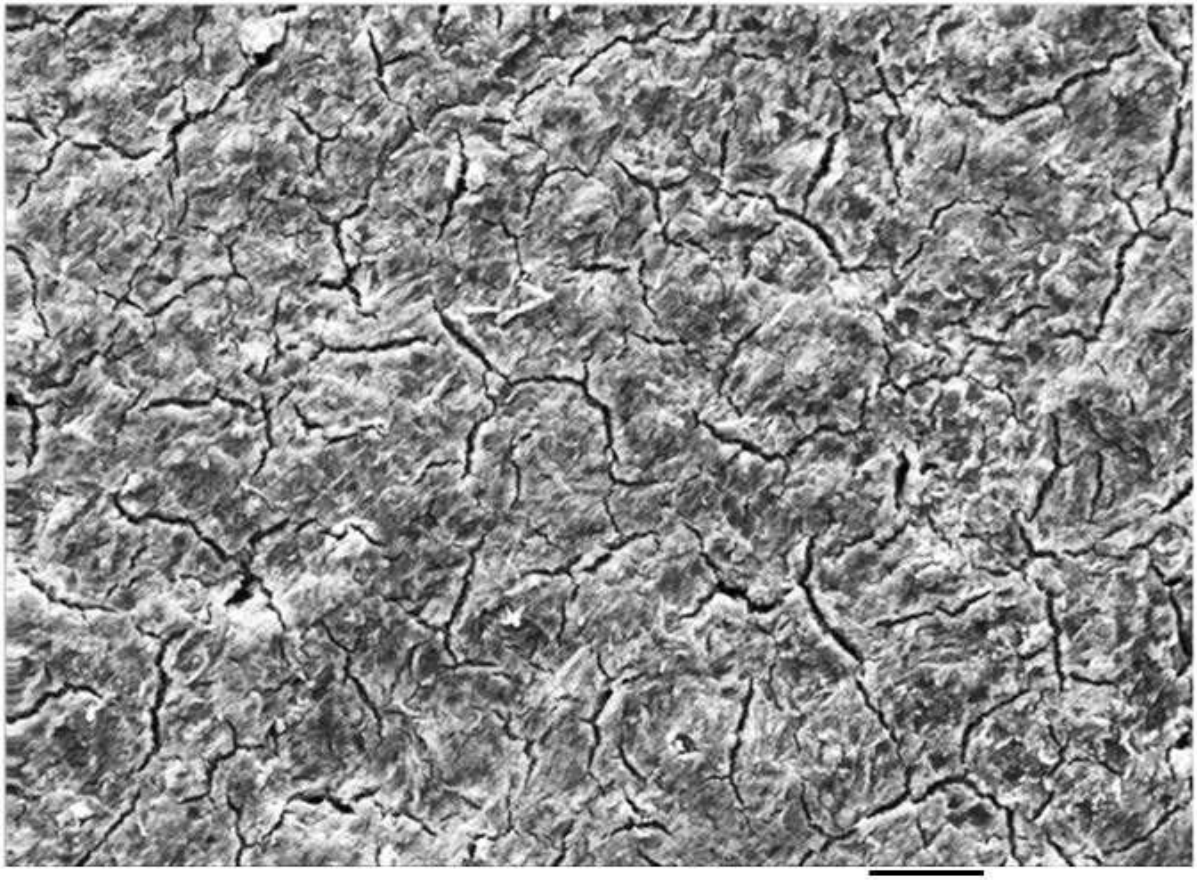

A

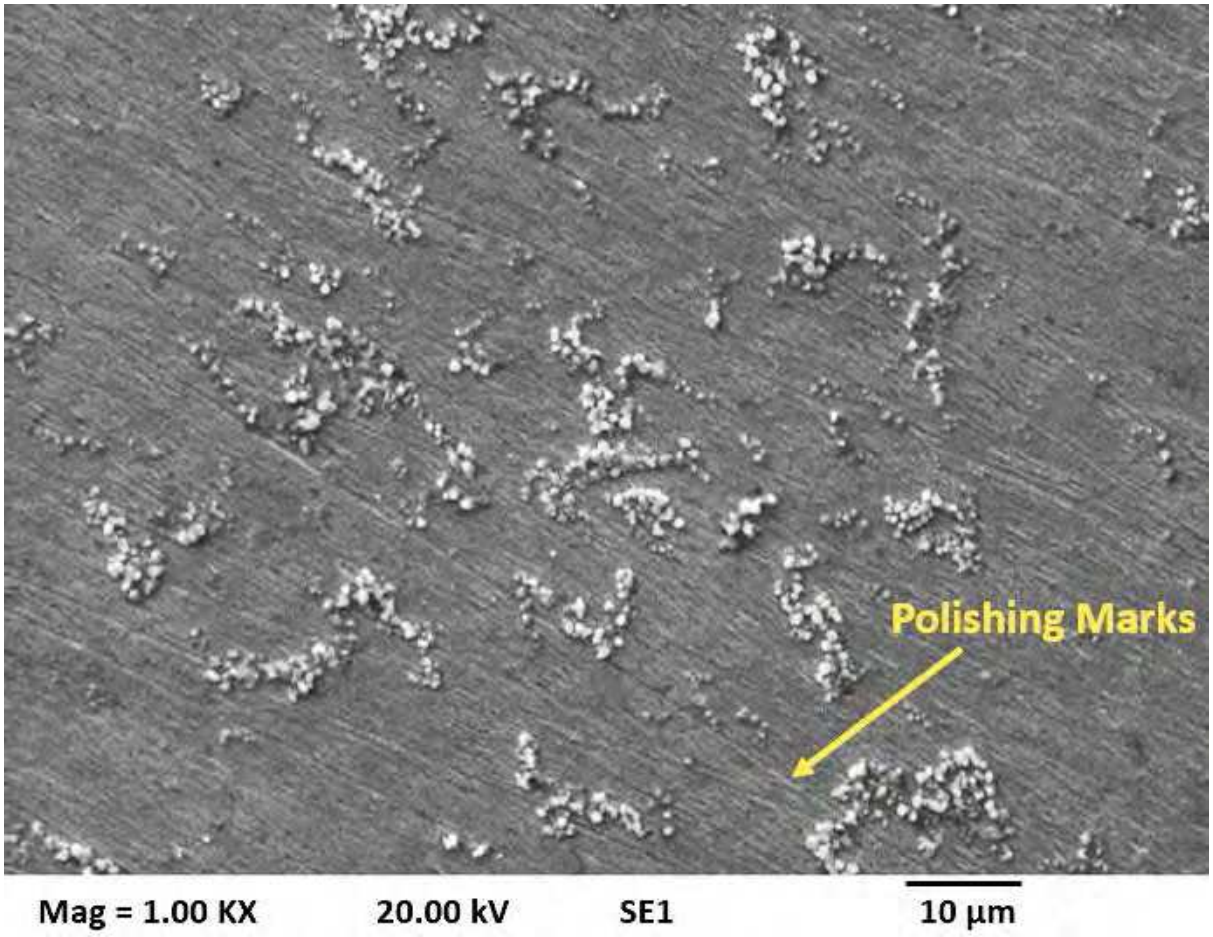

B

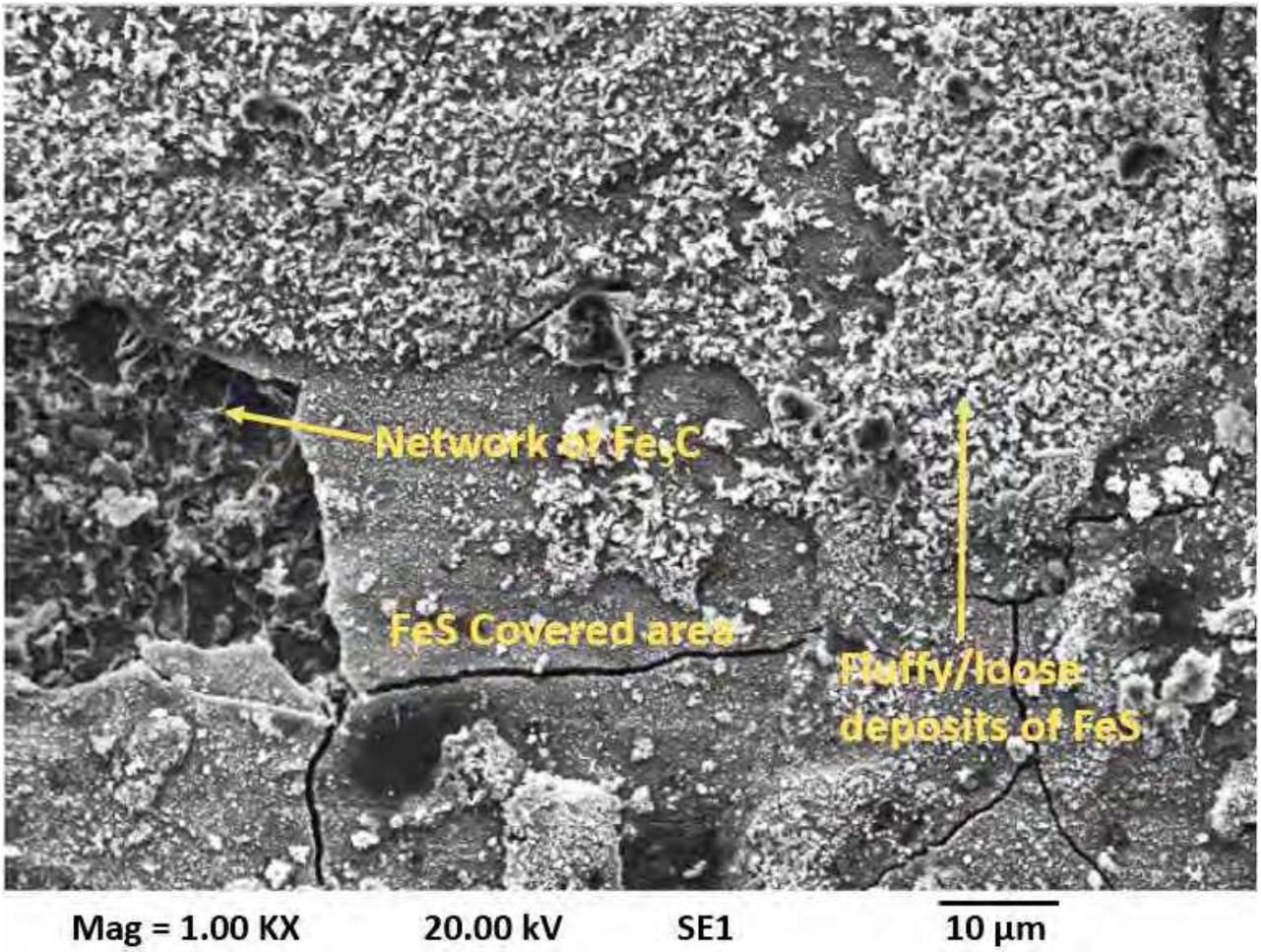
Network of Fe_3C
FeS Covered area
Fluffy/loose deposits of FeS
Mag = 1.00 KX
20.00 kV
SE1
10 µm

c

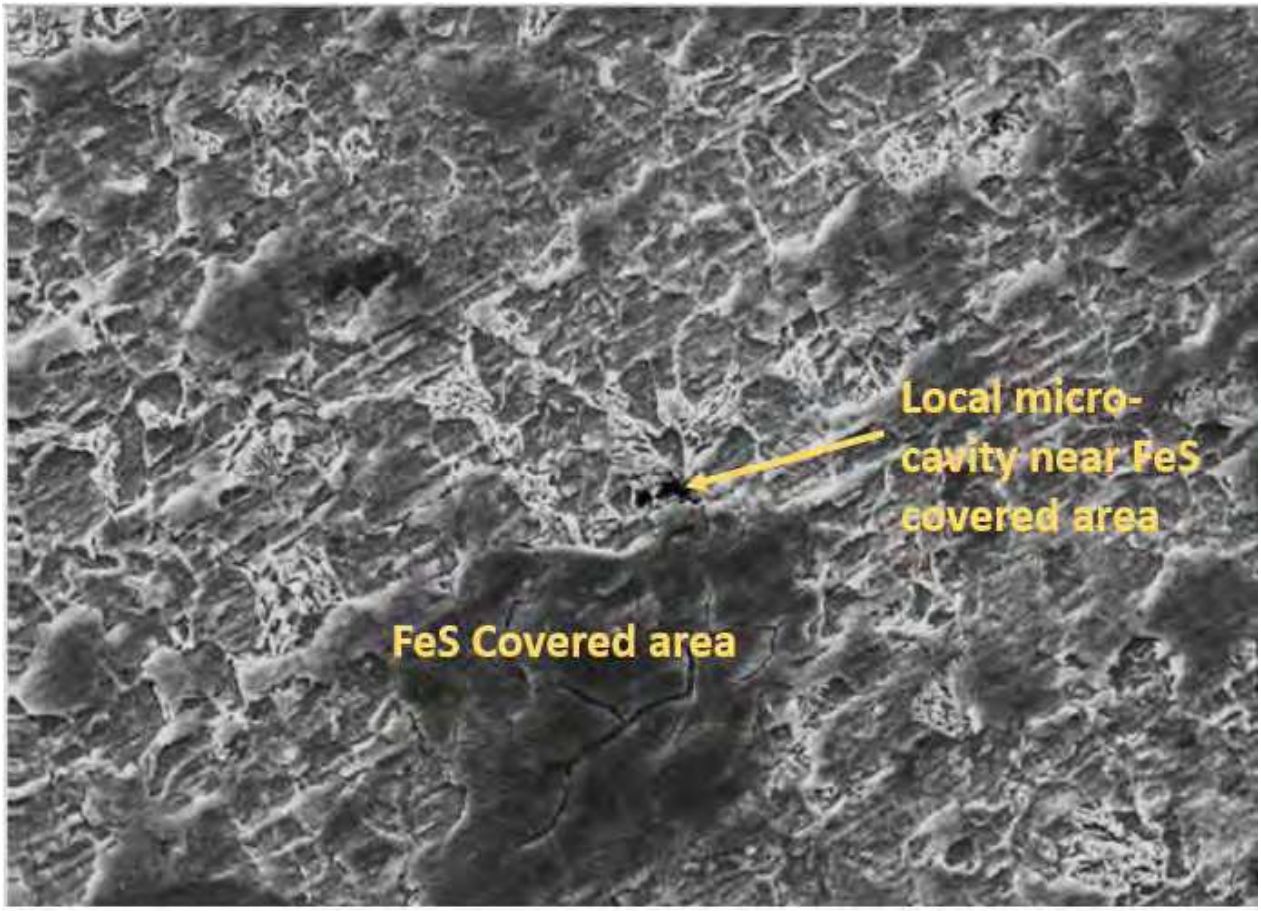

Mag = 1.00 KX 20.00 kV SE1 10 µm

D

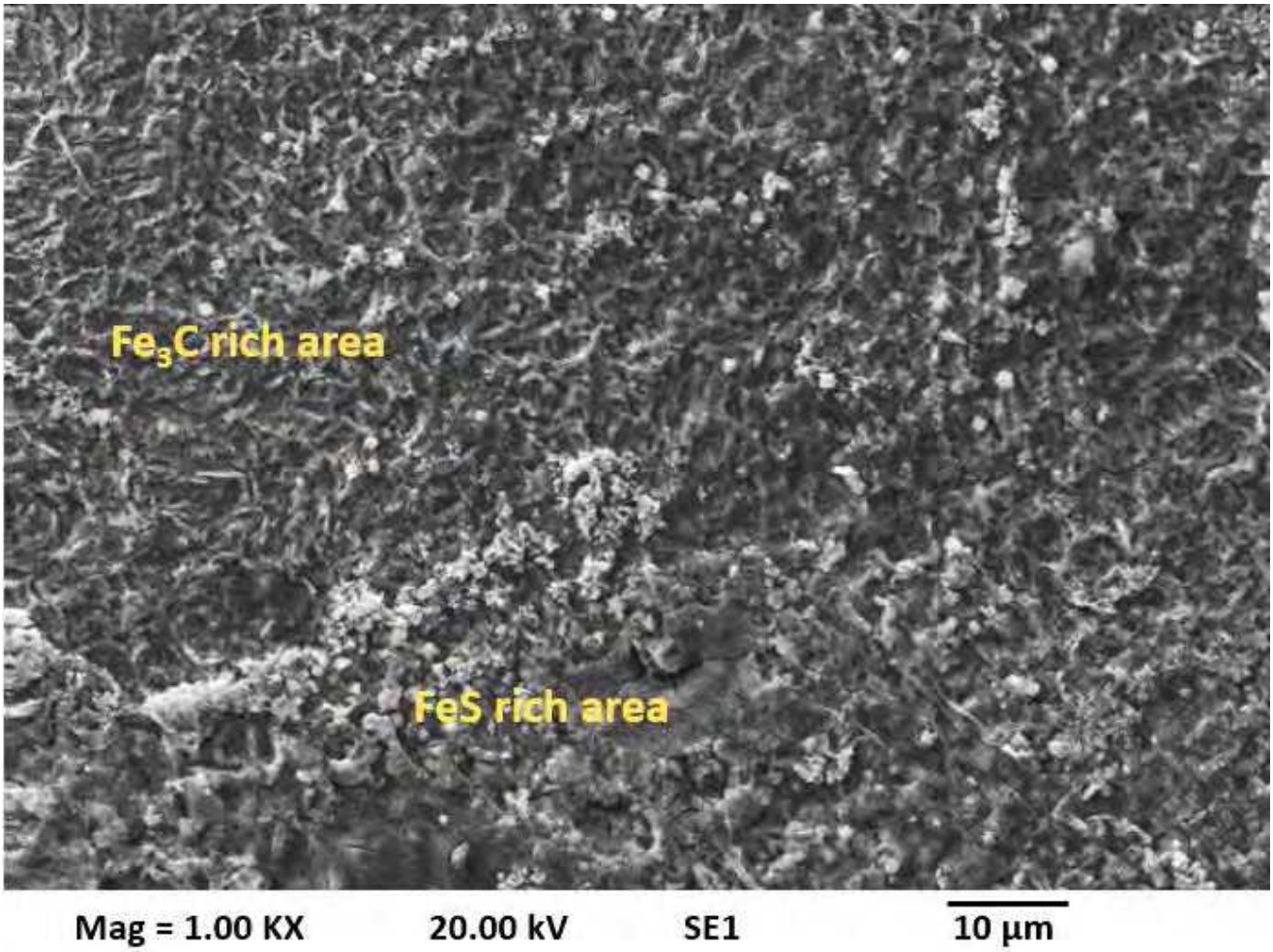

E

Figure 4: SEM images of corrosion product layer on X65 carbon steel in 3.5 wt. % NaCl solution under different combinations of H_2S-CO_2 gas;(a) 100 mol.% CO_2 , (b) 100 ppm of H_2S gas, (c) 1000 ppm of H_2S gas, (d) 1% of H_2S gas (e) 10% of H_2S gas at 30℃ and after 168 h.

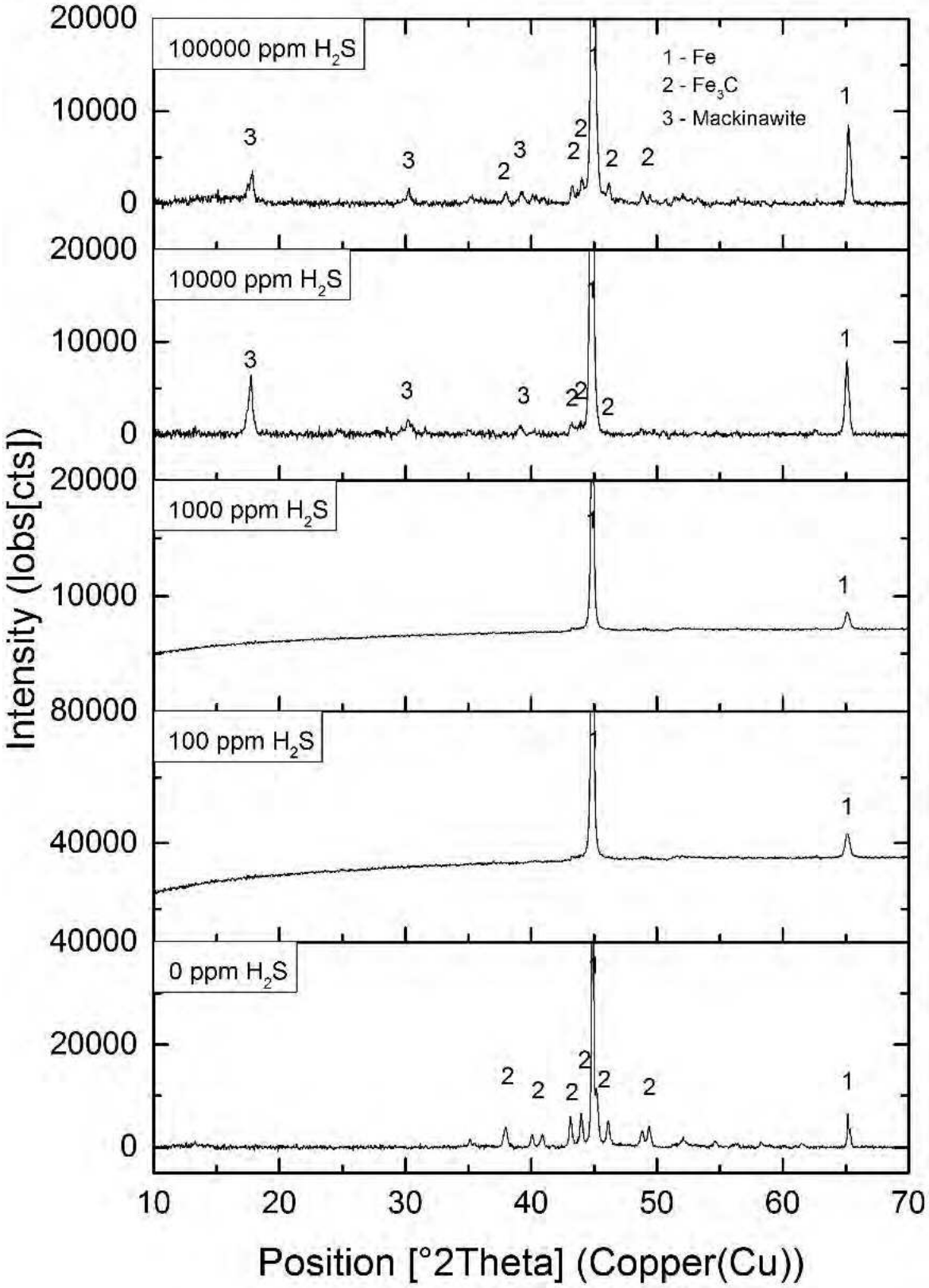

Figure 5: XRD patterns for corrosion products formed on X65 carbon steel in 3.5 wt. % NaCl solution under different combinations of H_2S-CO_2 gas at 30℃ after 168 h.

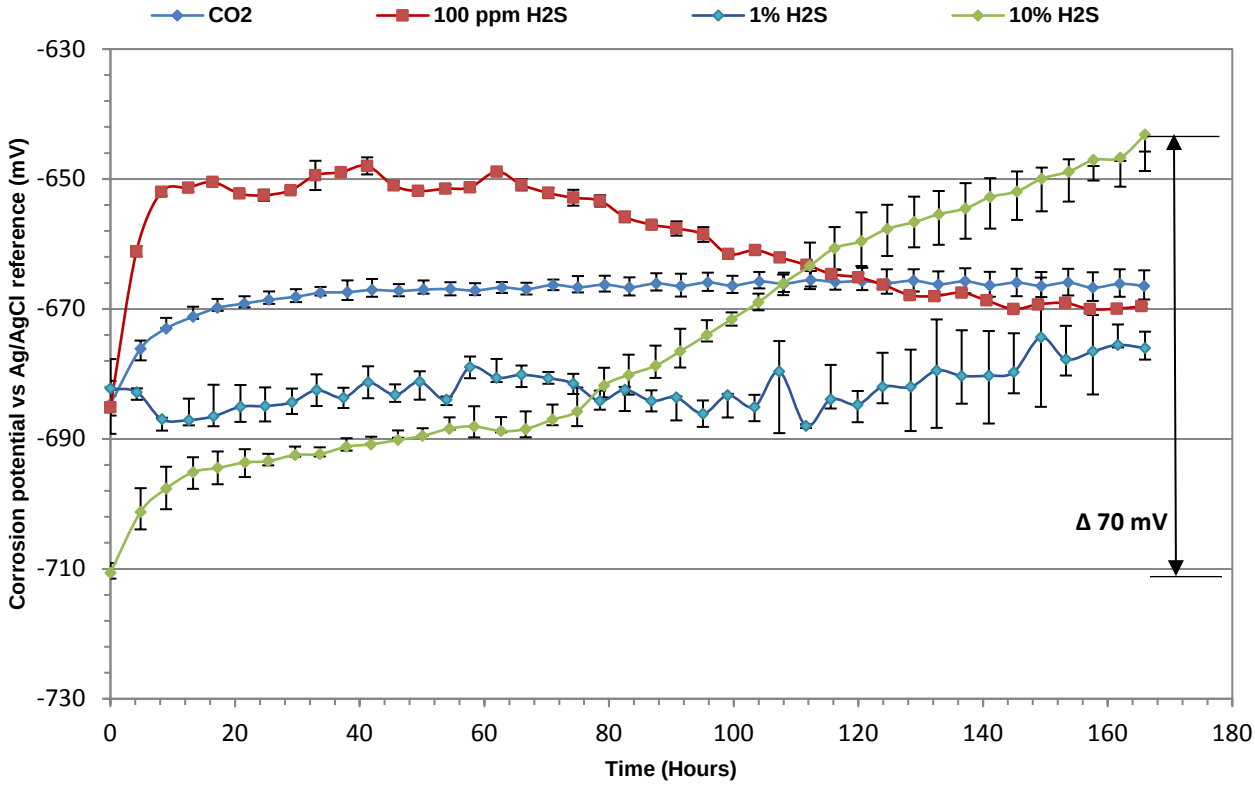

A

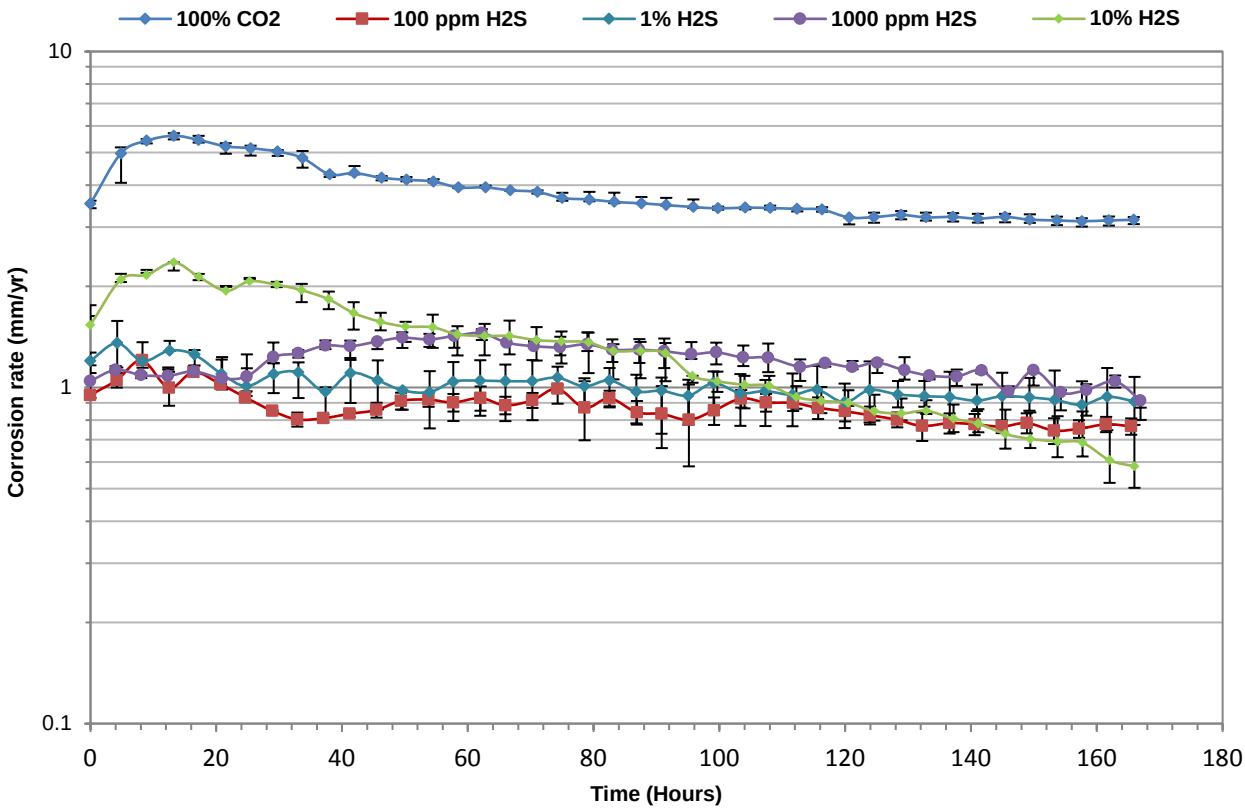

B

Figure 6: Graphs of (a) corrosion potential and (b) corrosion rate of X65 carbon steel in 3.5 wt. % NaCl solution under different combination of H_2S-CO_2 gas at 80℃, over 168 h.

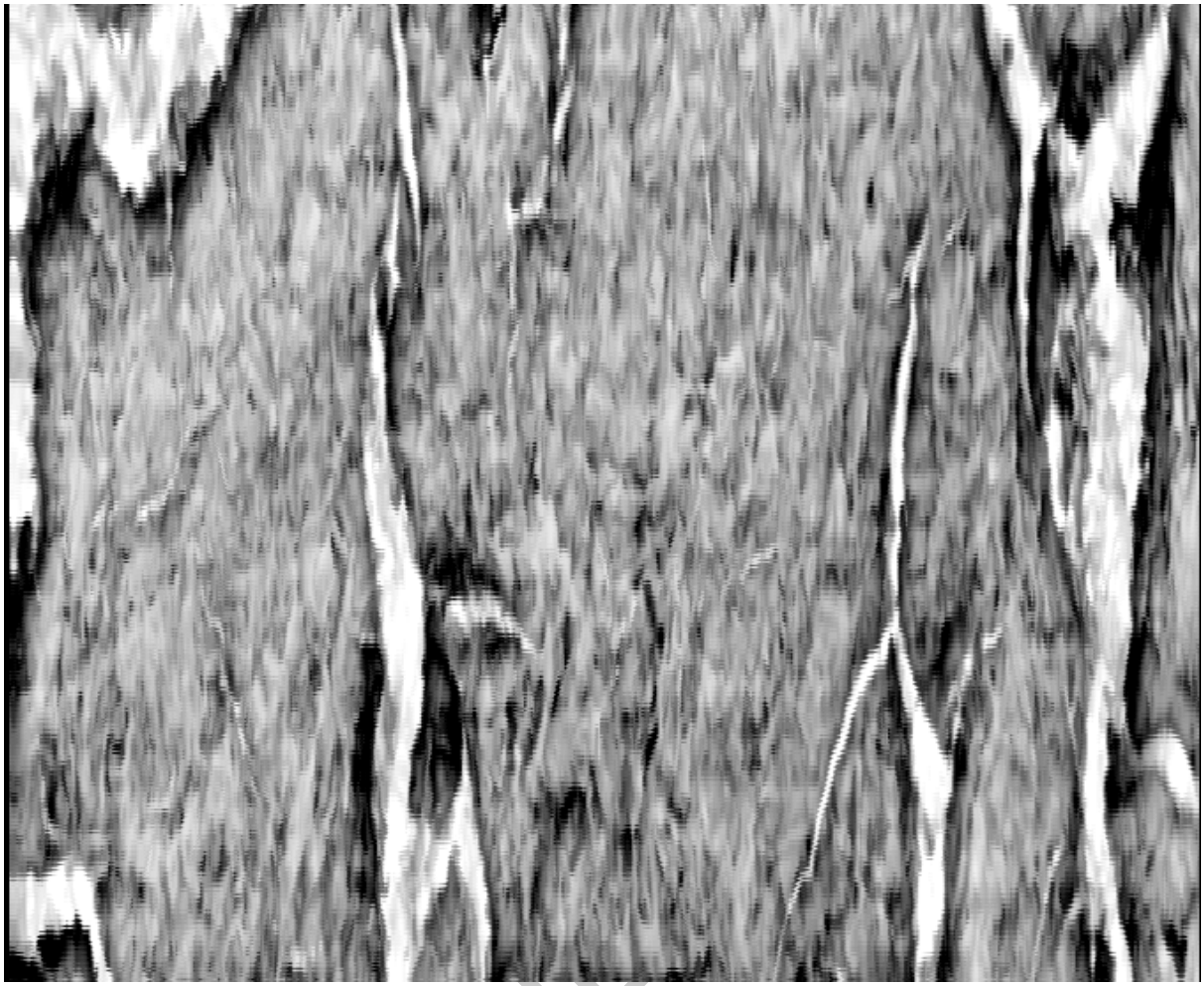

A

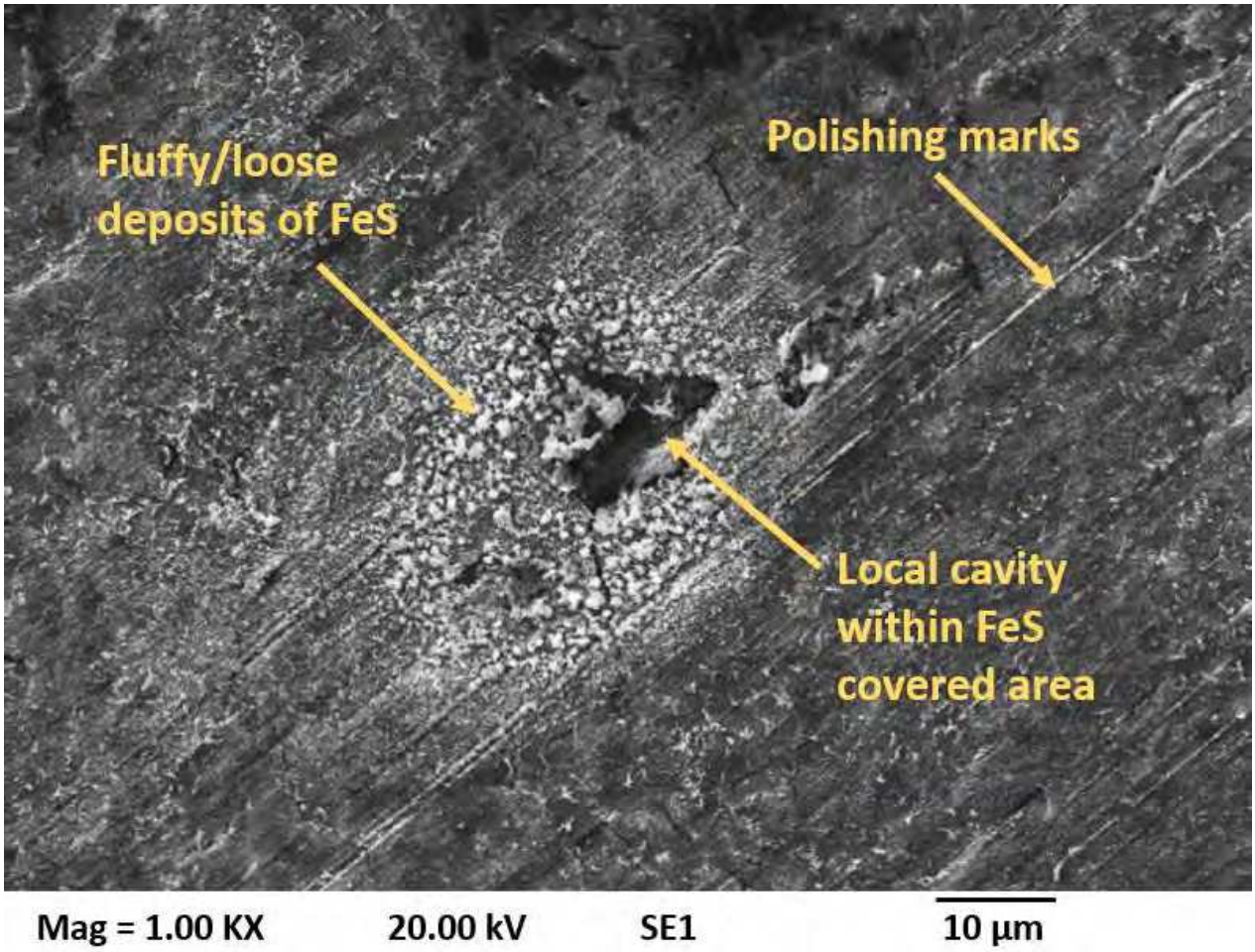
Fluffy/loose
deposits of FeS
Polishing marks
Local cavity
within FeS
covered area
Mag = 1.00 KX
20.00 kV
SE1
10 µm

B

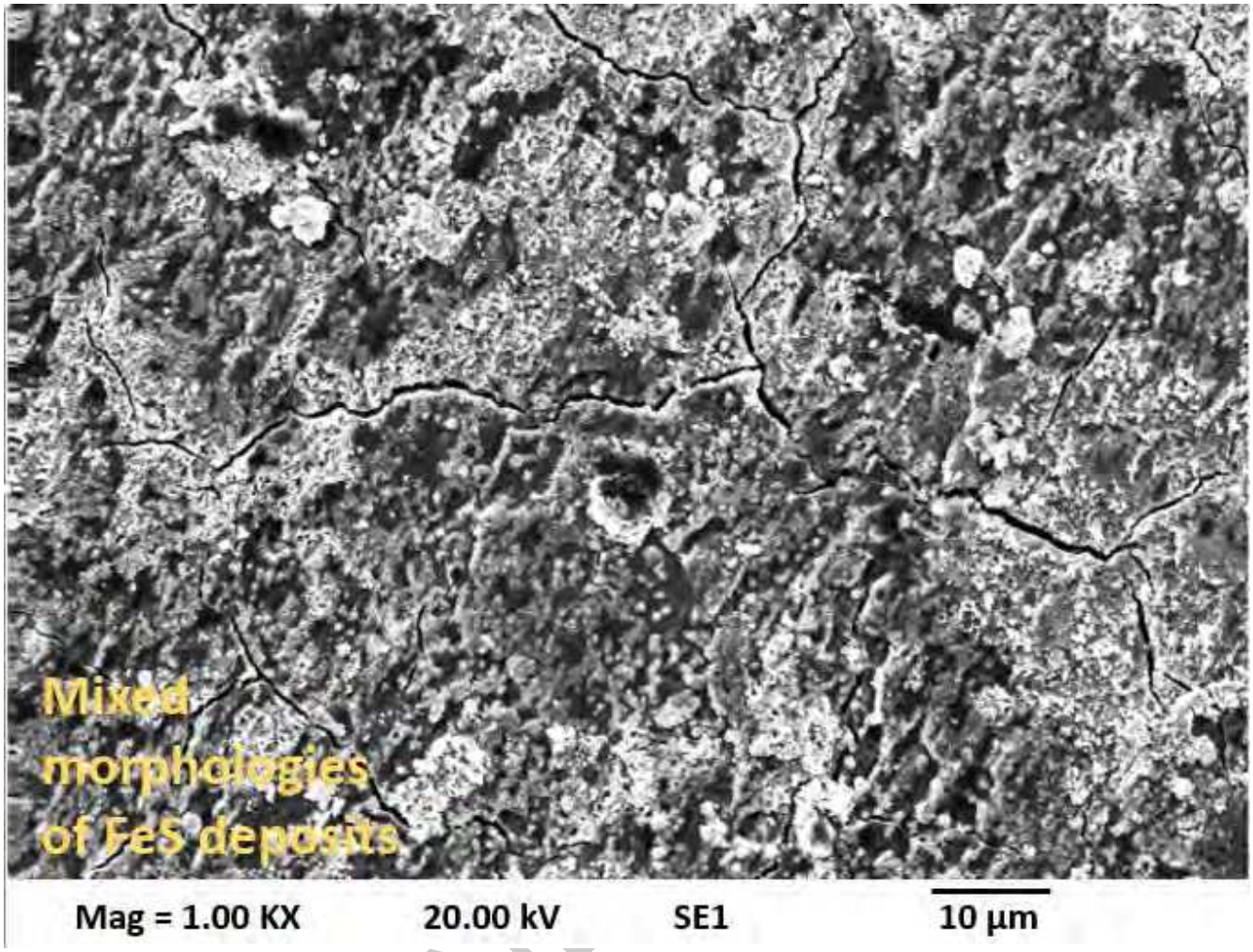
Mixed
morphologies
of FeS deposits
Mag = 1.00 KX
20.00 kV
SE1
10 µm

c

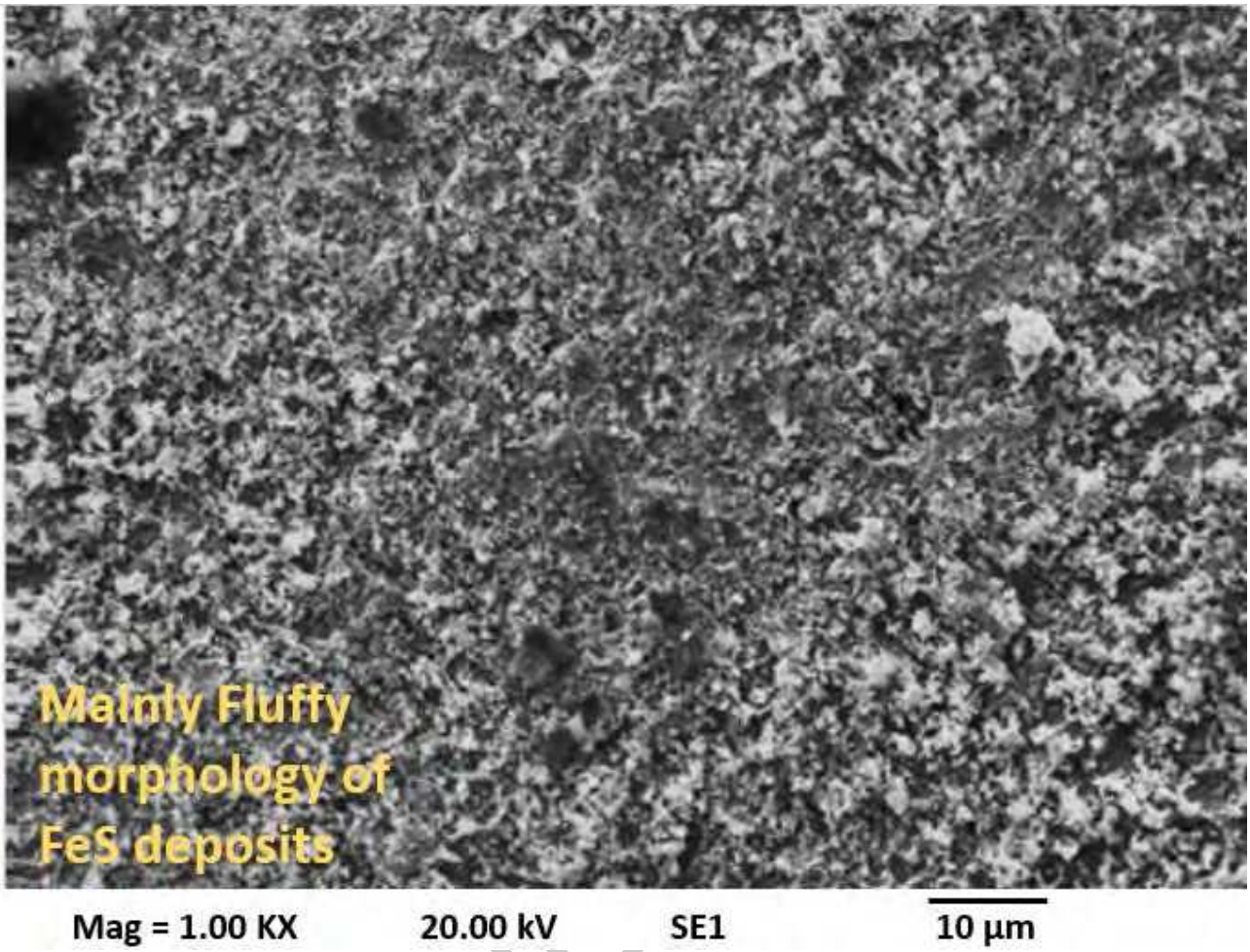
Mainly Fluffy
morphology of
FeS deposits
Mag = 1.00 KX
20.00 kV
SE1
10 µm

D

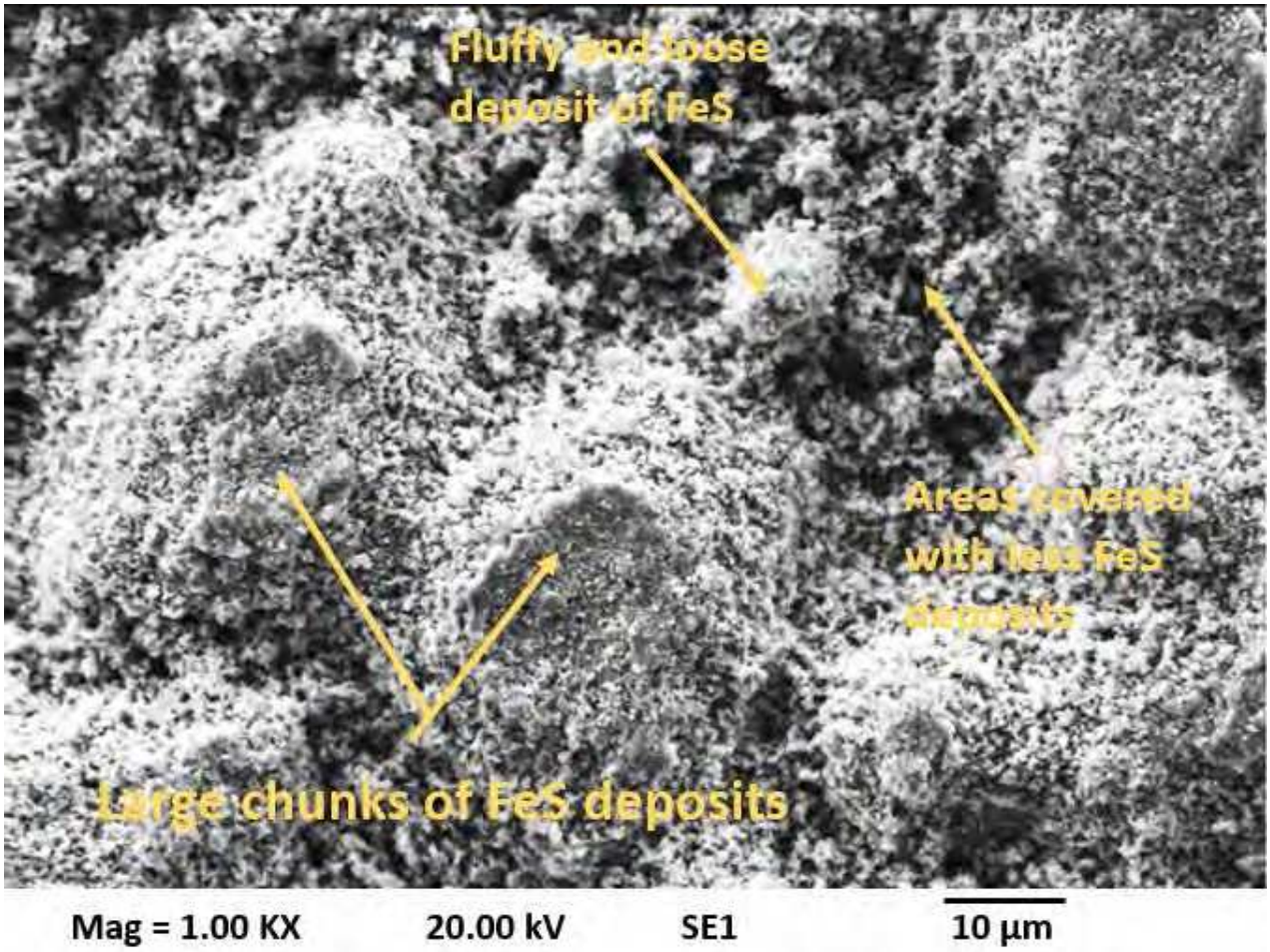
Fluffy and loose
deposit of FeS
Areas covered
with less FeS
deposits
Large chunks of FeS deposits
Mag = 1.00 KX
20.00 kV
SE1
10 µm

E

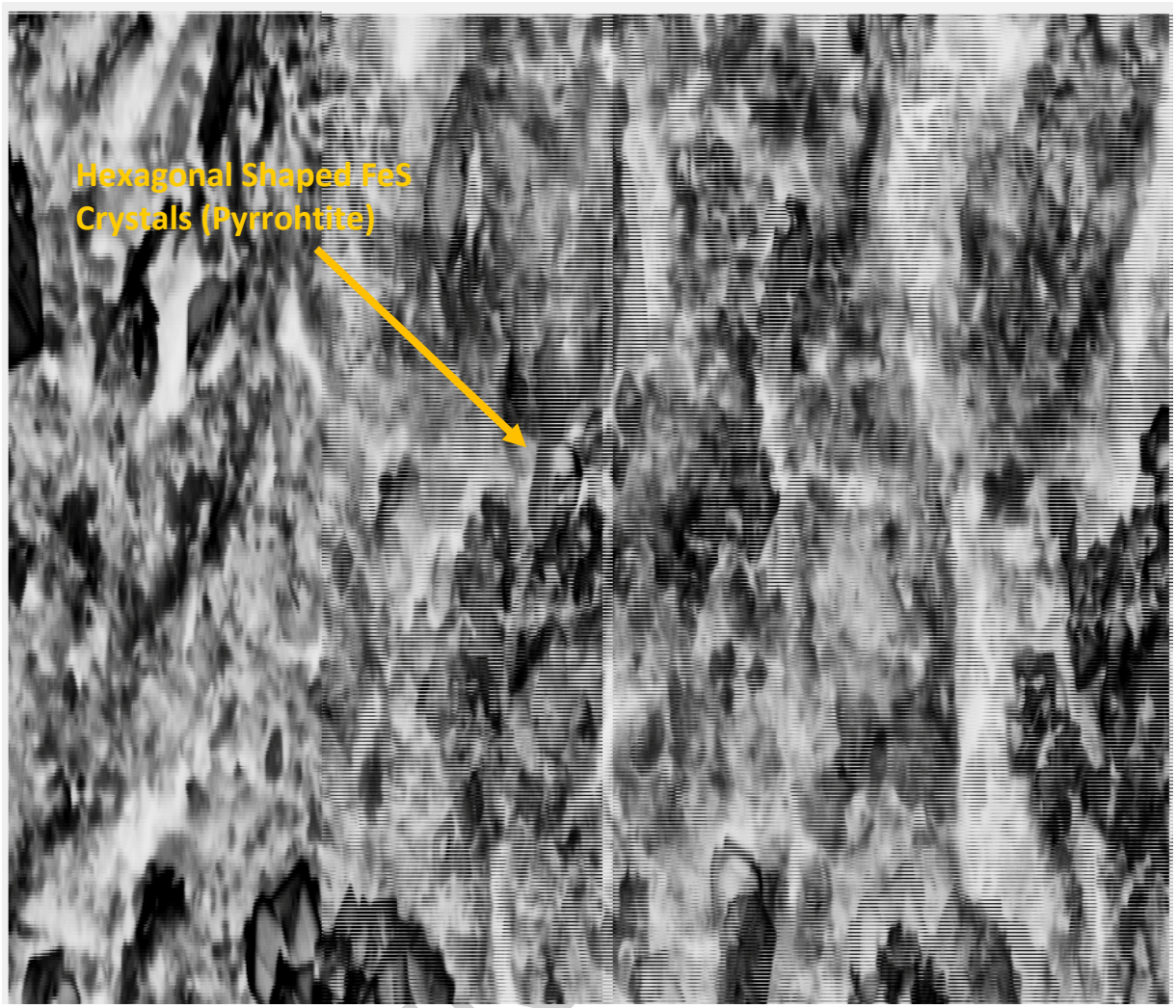

F

Figure 7: SEM images of corrosion product layer on X65 carbon steel in 3.5 wt. % NaCl solution under different combinations of H_2S-CO_2 gas;(a) 100 mol. % CO_2, (b) 100 ppm of H_2S gas, (c) 1000 ppm of H_2S gas, (d) 1% of H_2S gas (e) 10% of H_2S (f) 10% of H_2S (Higher Magnification) gas at 80℃ and after 168 h.

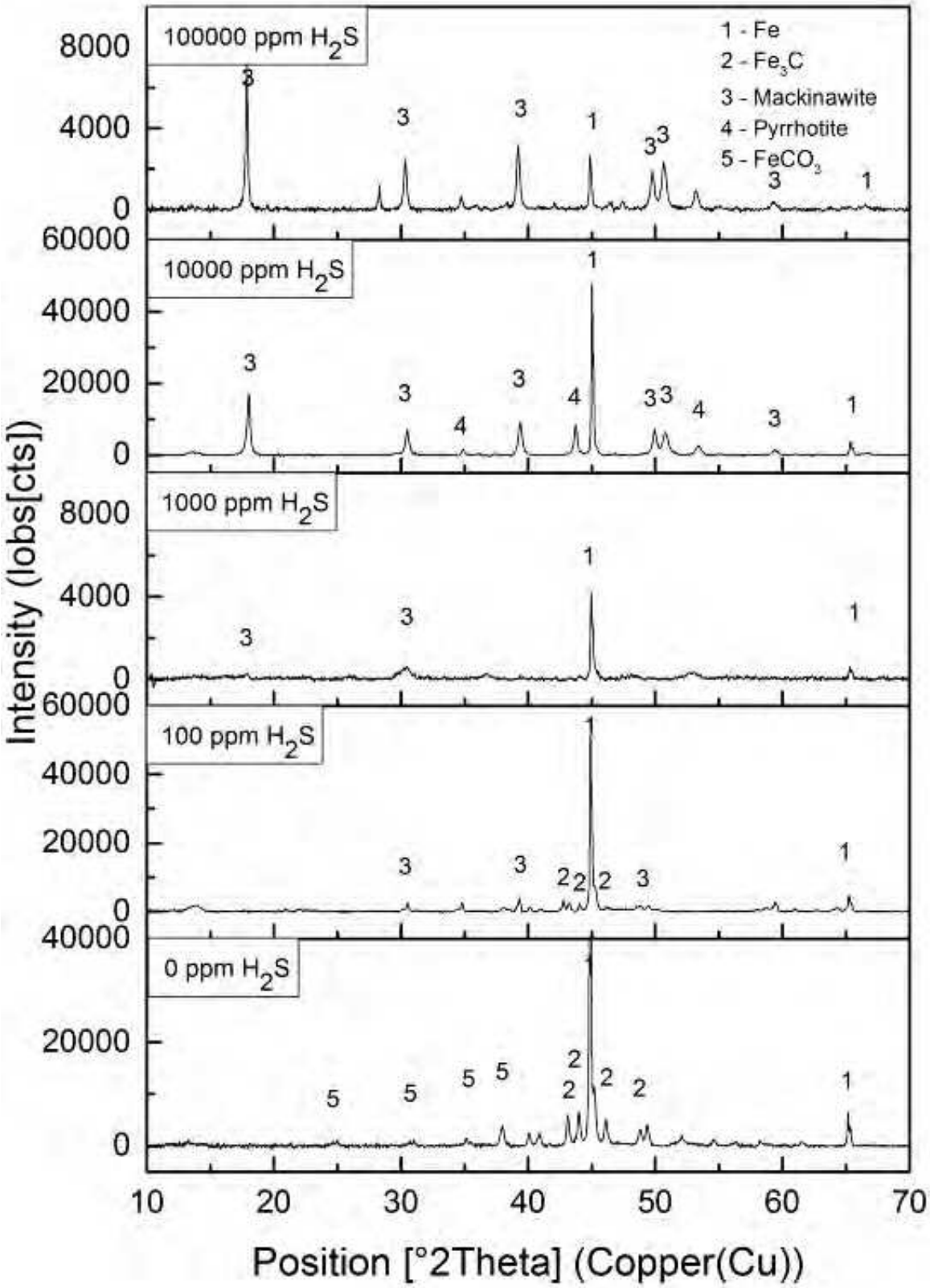

Figure 8: XRD patterns for corrosion products formed on X65 carbon steel in 3.5 wt.% NaCl solution under different combinations of H_2S-CO_2 gas at 80℃ after 168 h.

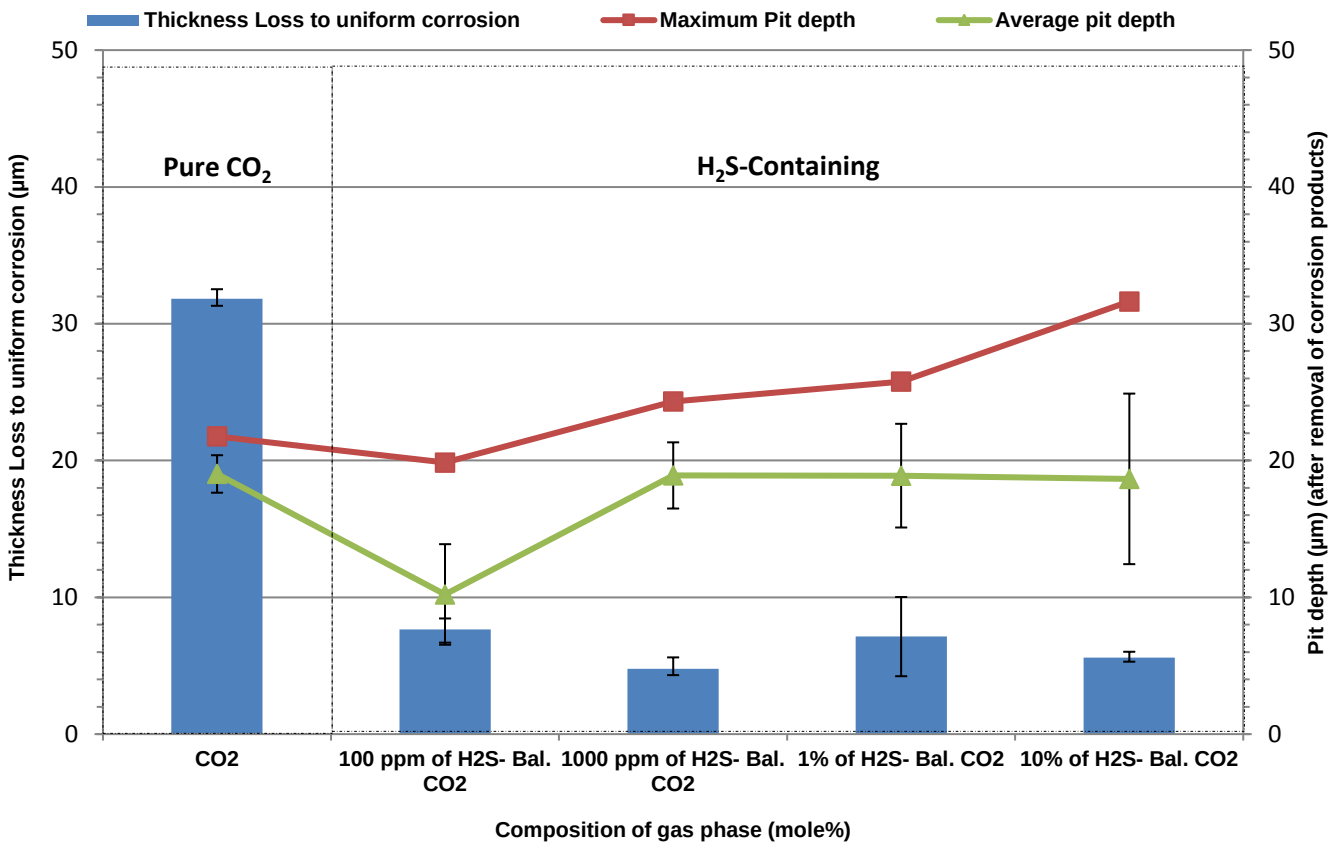

Figure 9: Contribution of thickness loss to uniform corrosion and pit depths (relative to corroded surface) of X65 carbon steel in 3.5 wt. % NaCl solution under exposed to different combination of H_2S-CO_2 gas at 30℃ for 168 h.

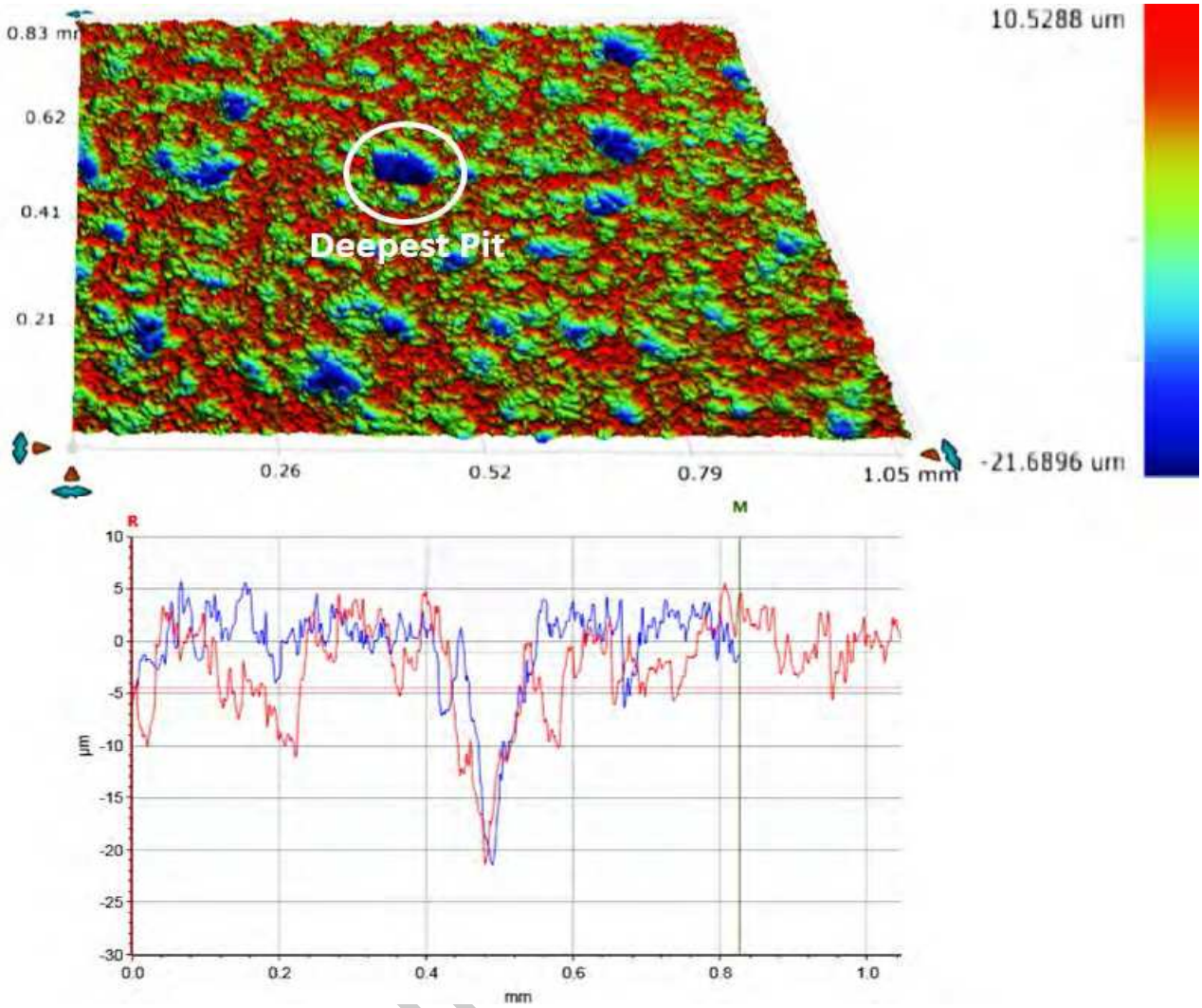
0.83 mm
0.62
0.41
0.21
Deepest Pit
0.26
0.52
0.79
1.05 mm
10.5288 um
-21.6896 um
M
R
µm
mm

A

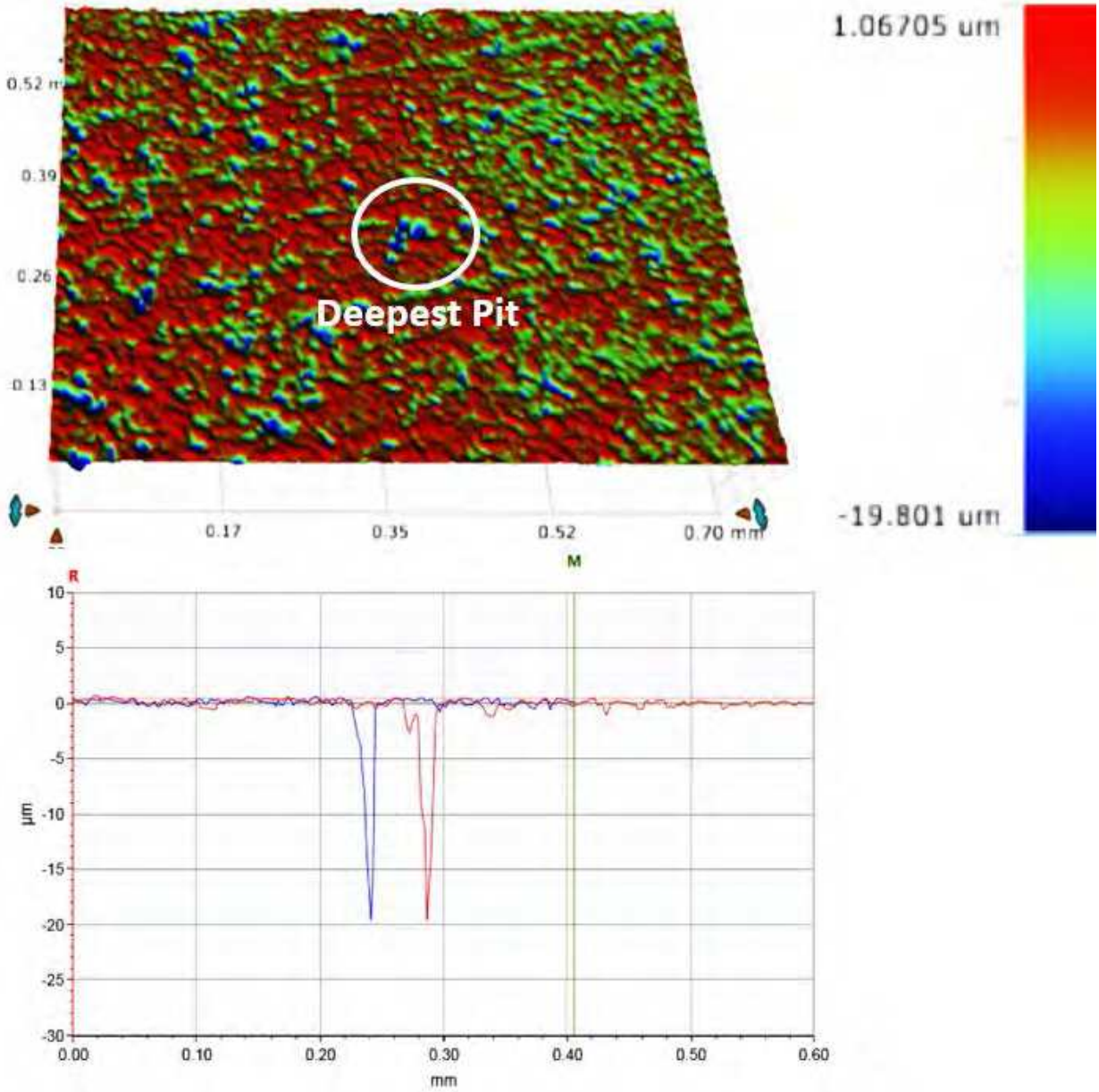
1.06705 um
-19.801 um
Deepest Pit
0.52 mm
0.39
0.26
0.13
0.17
0.35
0.52
0.70 mm
M
R
µm
mm

B

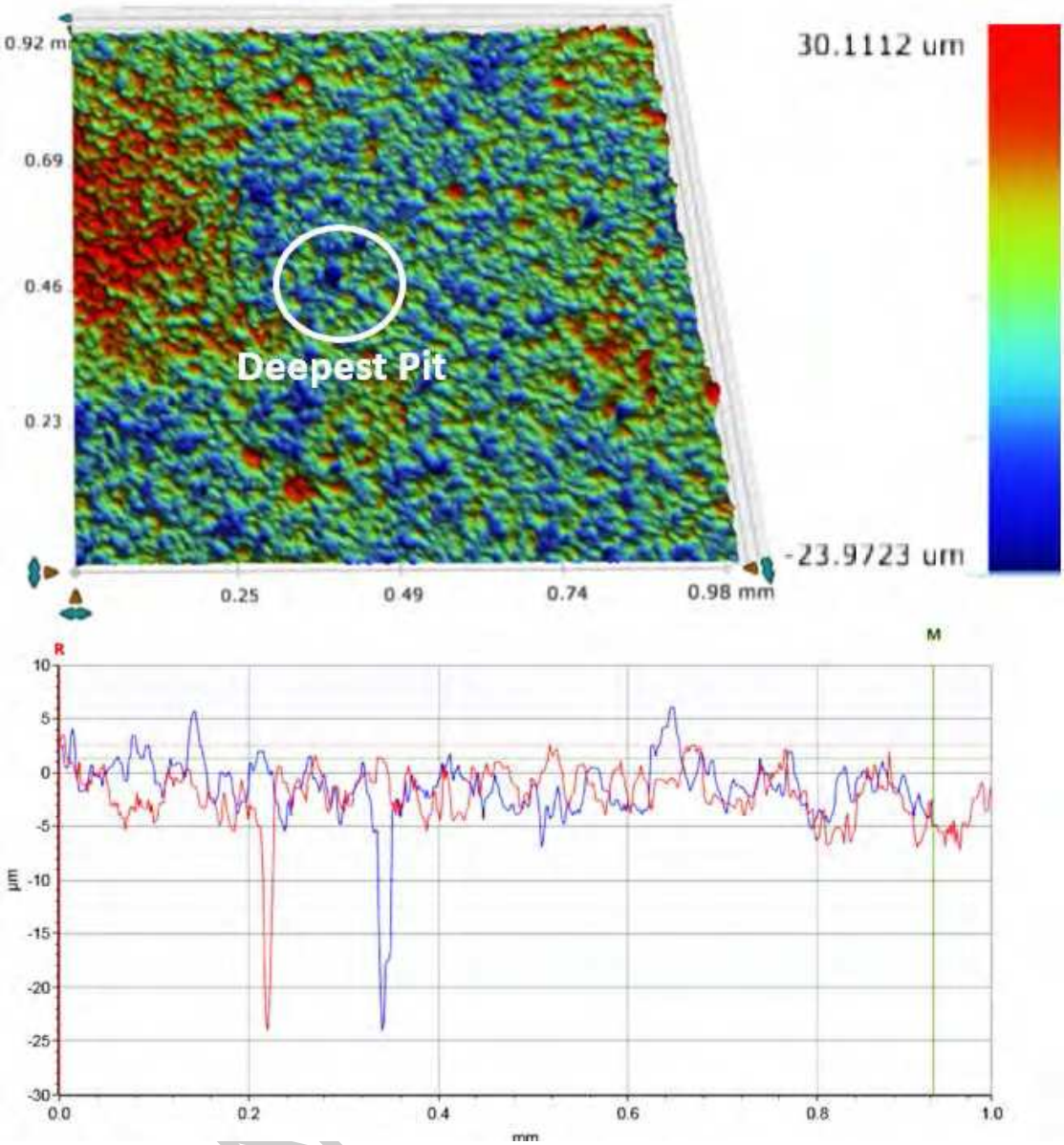
0.92 mm
0.69
0.46
0.23
30.1112 um
-23.9723 um
Deepest Pit
0.25
0.49
0.74
0.98 mm
R
M
µm
mm

c

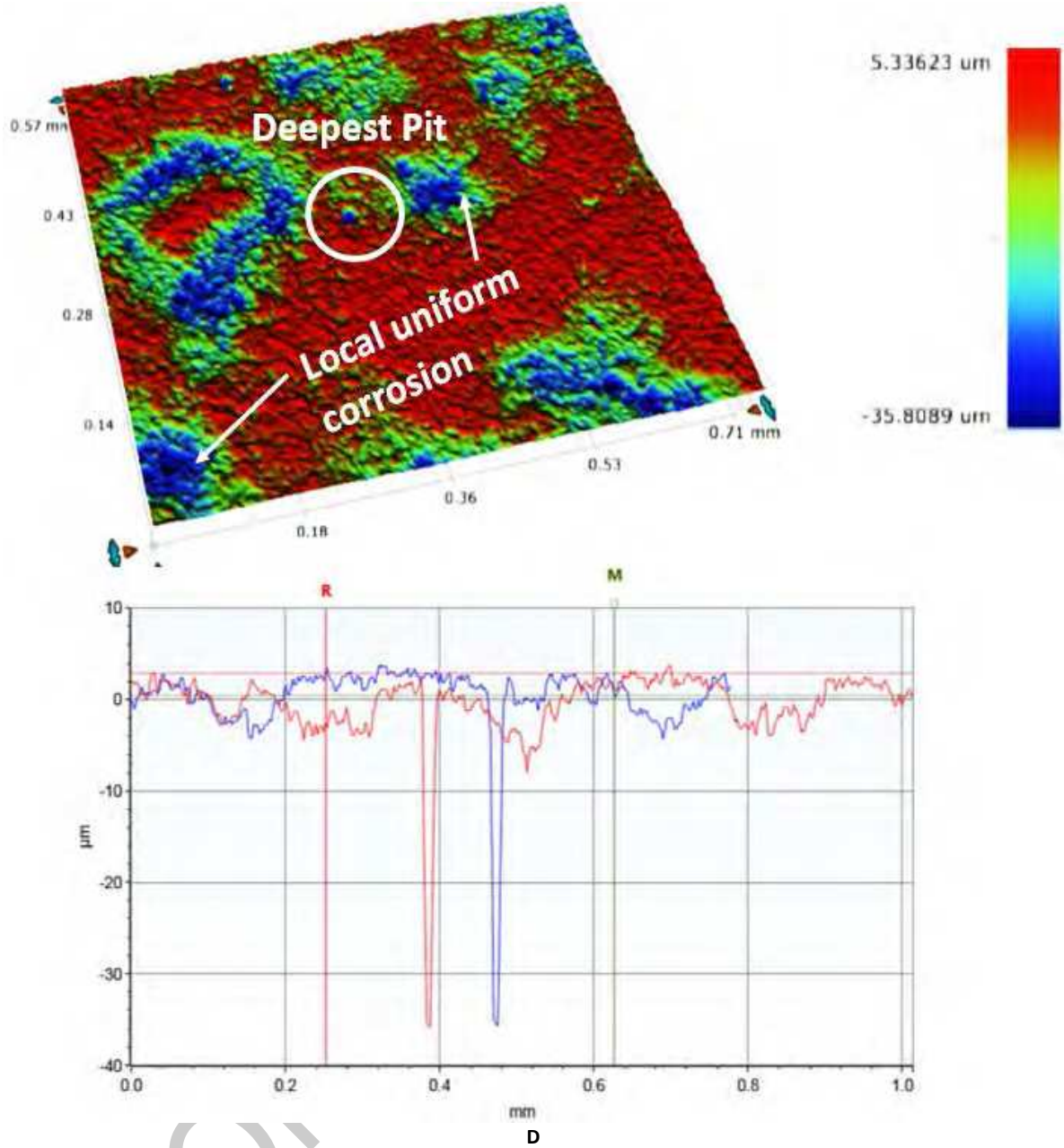

Figure 10: 3D images of pitting corrosion damage on carbon steel surface exposed to (a) pure CO_2, (b)100 ppm of H_2S, (c) 1000 ppm of H_2S and (d) 10% of H_2S corrosion system after 168 hours at 30℃.

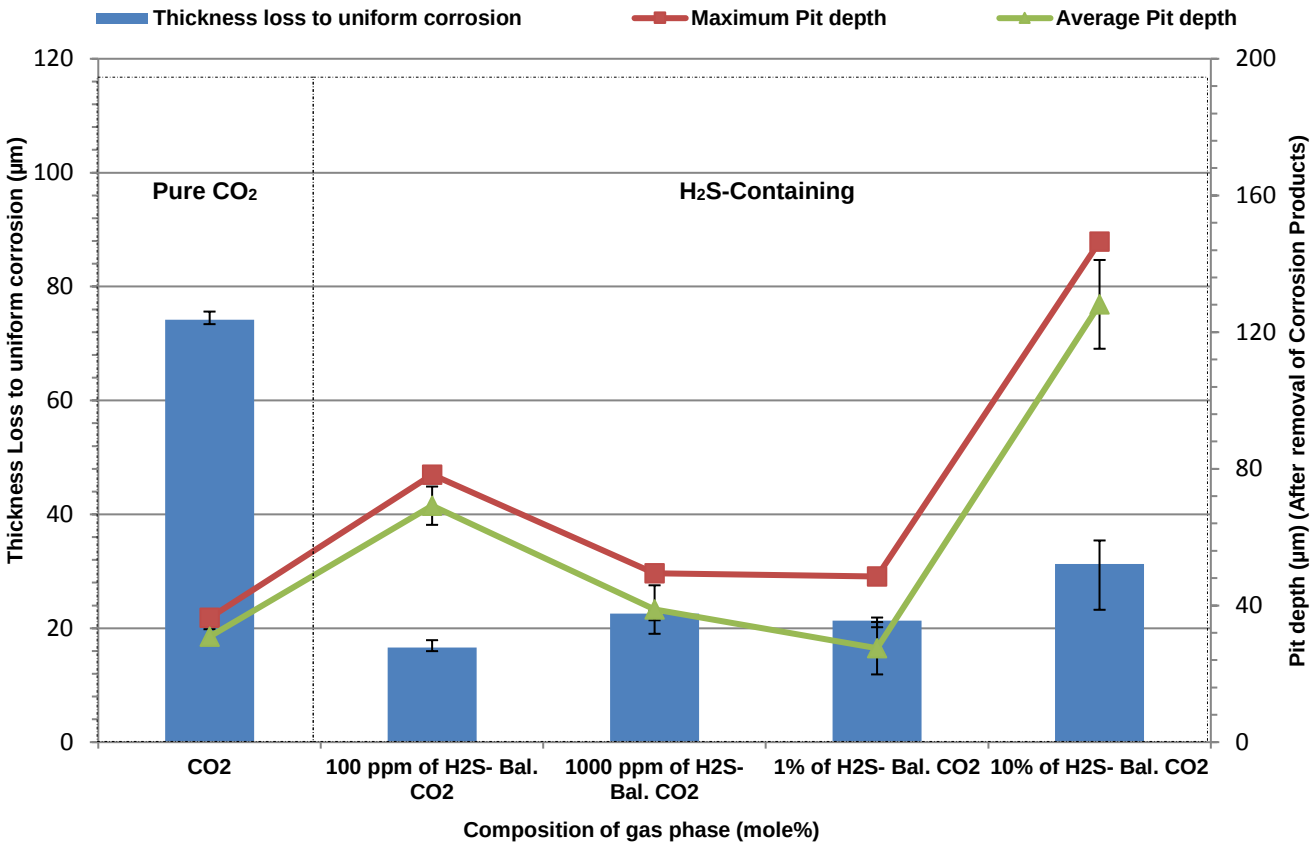

Figure 11: Contribution of thickness loss to uniform corrosion and pit depths (relative to corroded surface) of X65 carbon steel in 3.5 wt. % NaCl solution under exposed to different combination of H_2S-CO_2 gas at 80℃ for 168 hours.

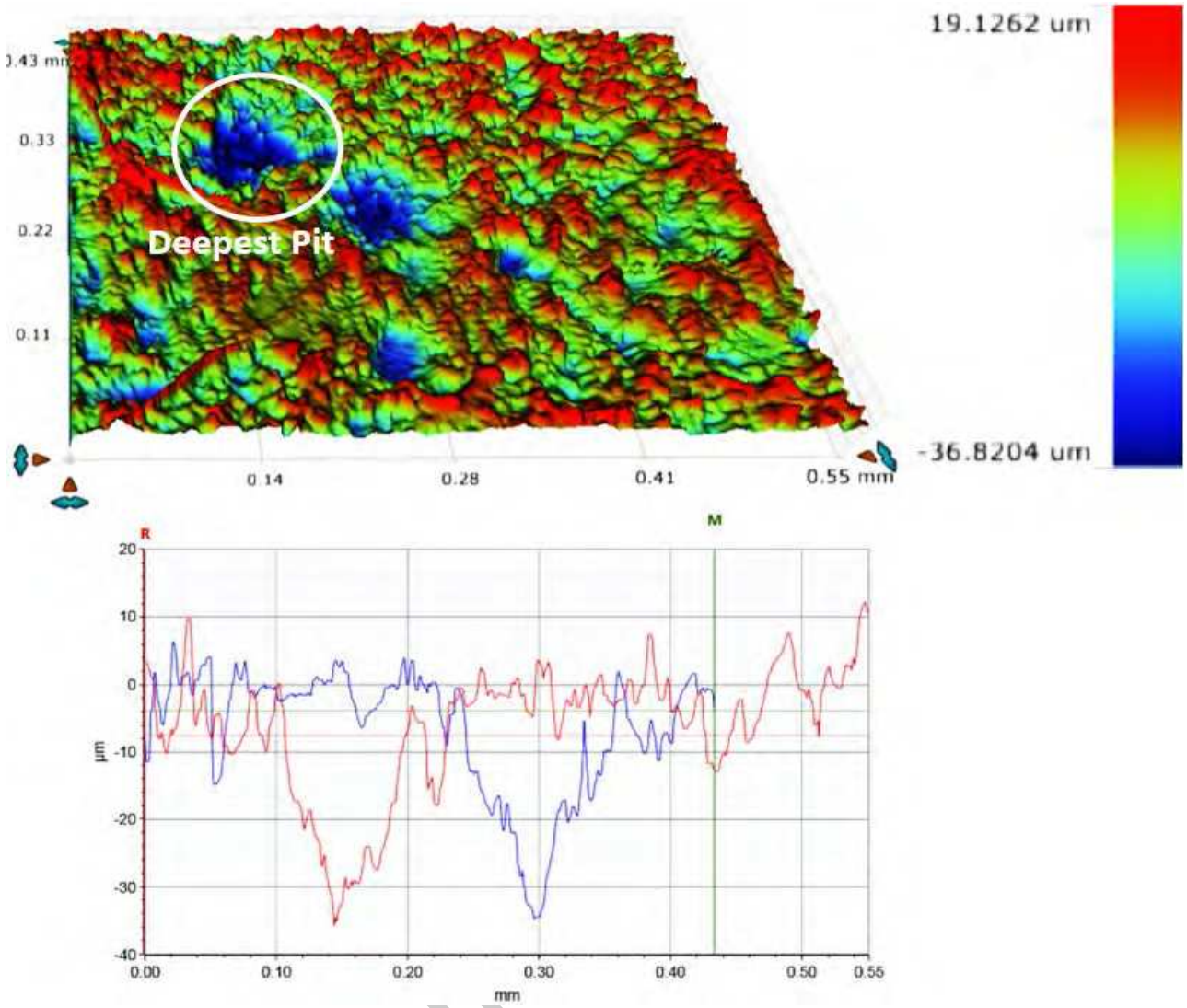
19.1262 um
-36.8204 um
Deepest Pit
0.33
0.22
0.11
0.14
0.28
0.41
0.55 mm
R
M
20
10
0
-10
-20
-30
-40
µm
0.00
0.10
0.20
0.30
0.40
0.50
0.55
mm

A

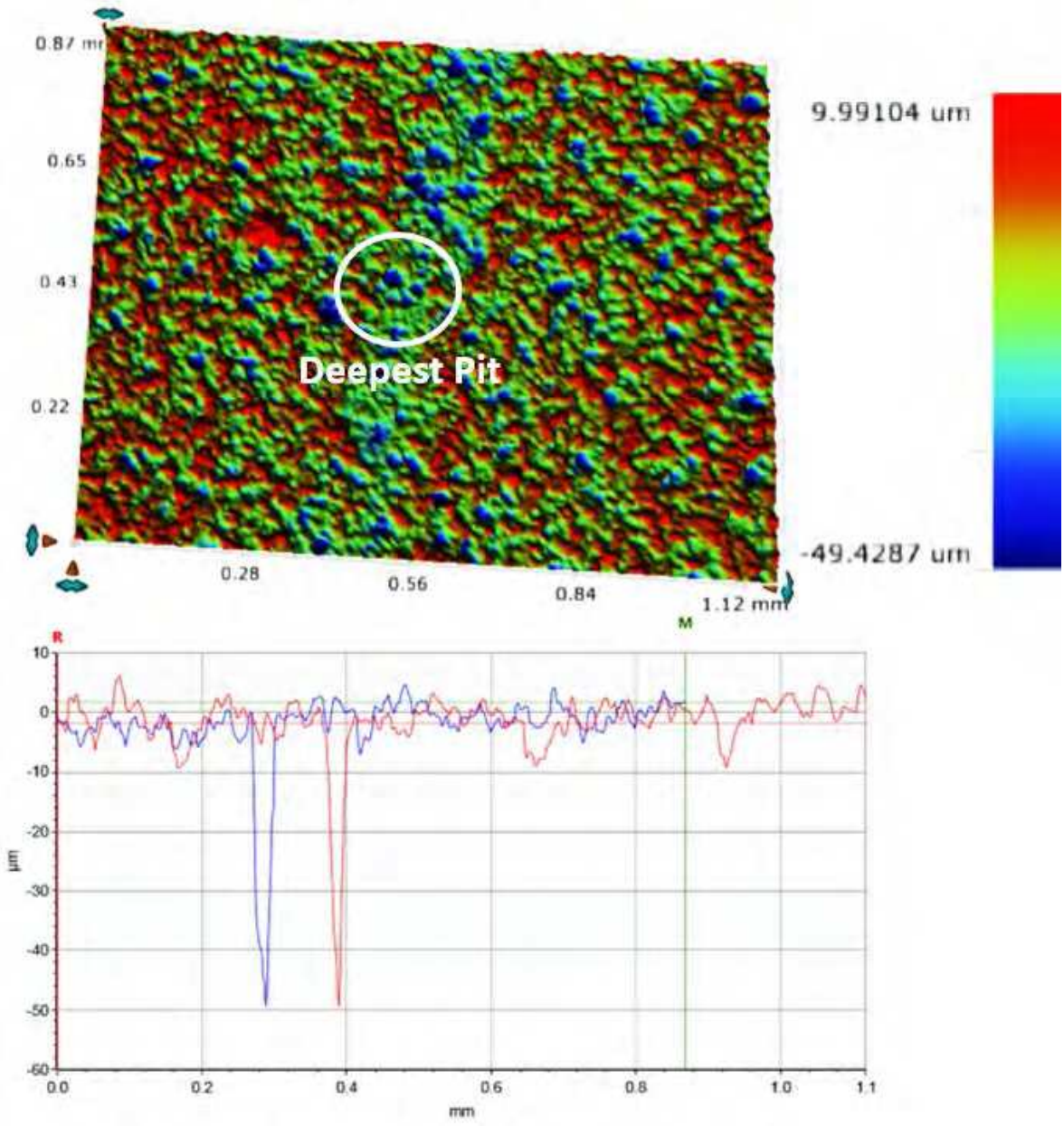
0.87 mm
0.65
0.43
0.22
0.28
0.56
0.84
1.12 mm
9.99104 um
-49.4287 um
Deepest Pit
R
M
10
0
-10
-20
-30
-40
-50
-60
µm
0.0
0.2
0.4
0.6
0.8
1.0
1.1
mm

B

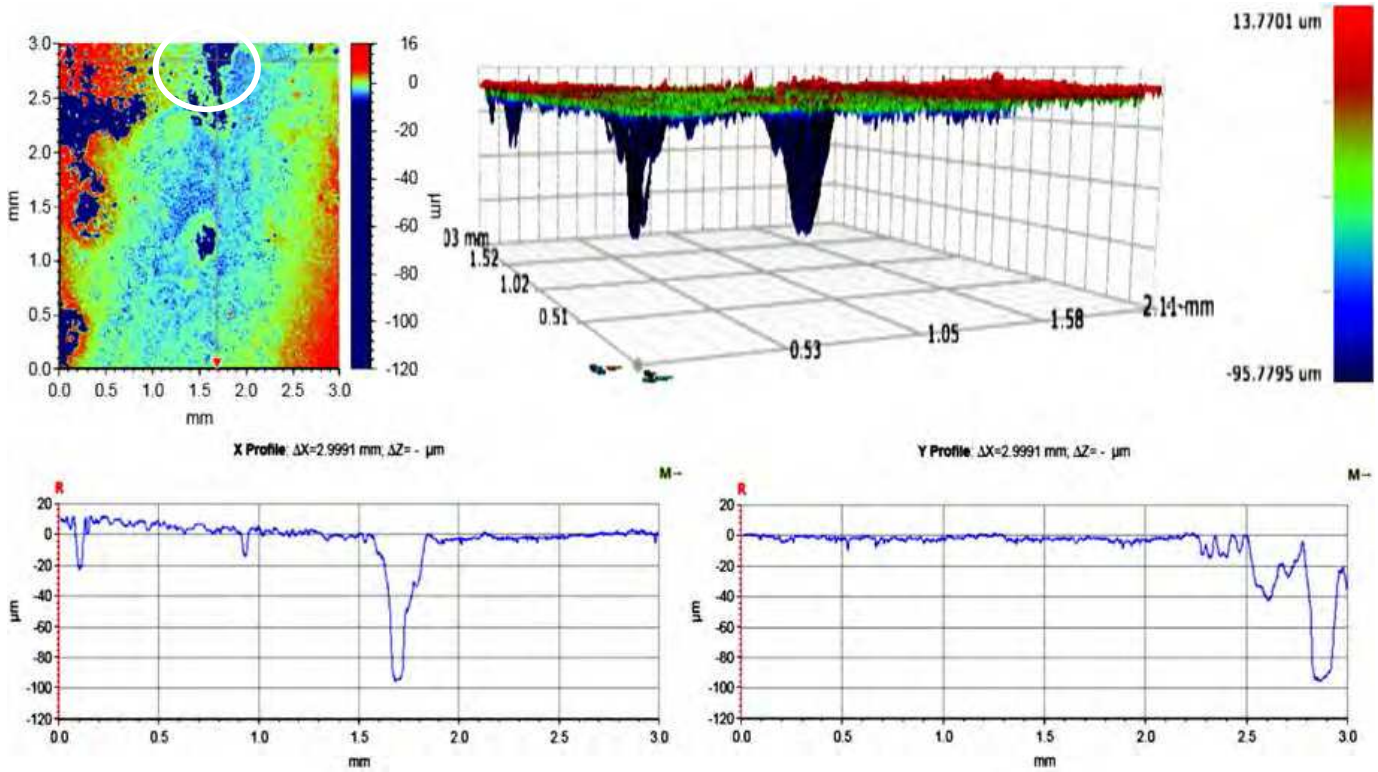

C

Figure 12: 3D images of pitting corrosion damage on carbon steel surface exposed to a) pure CO_2, (b) 1000 ppm of H_2S and (c) 10% of H_2S corrosion system after 168 h at 80℃.

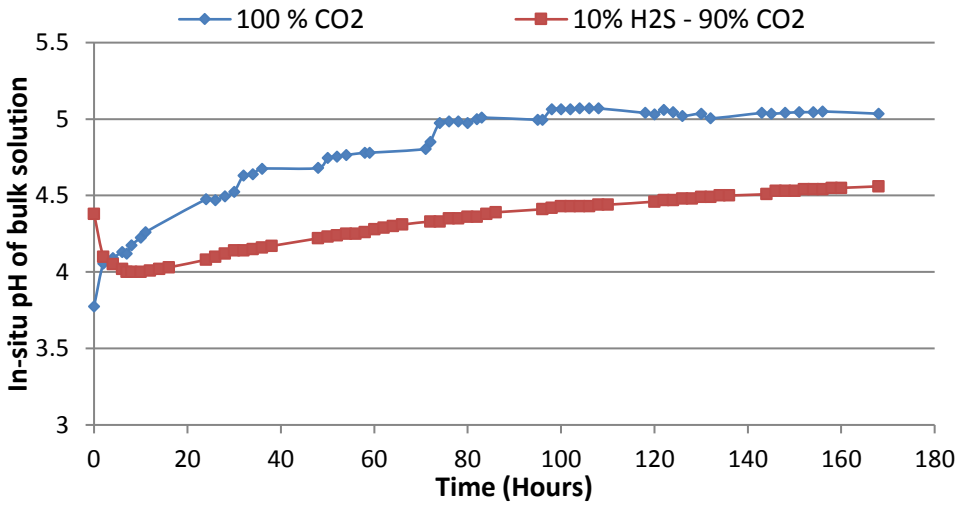

A

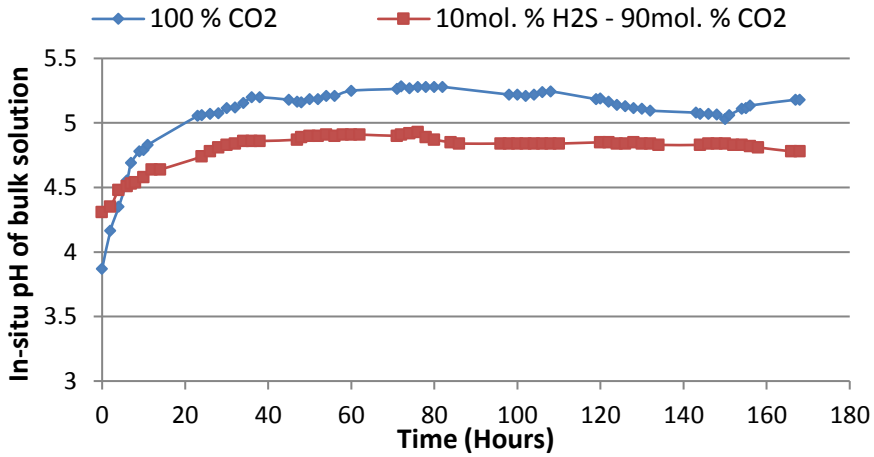

B

Figure 1: Measured *in-situ* pH of corrosion media under two different gas atmospheres at (a) 30°C and (b) 80°C, over 168 hours.

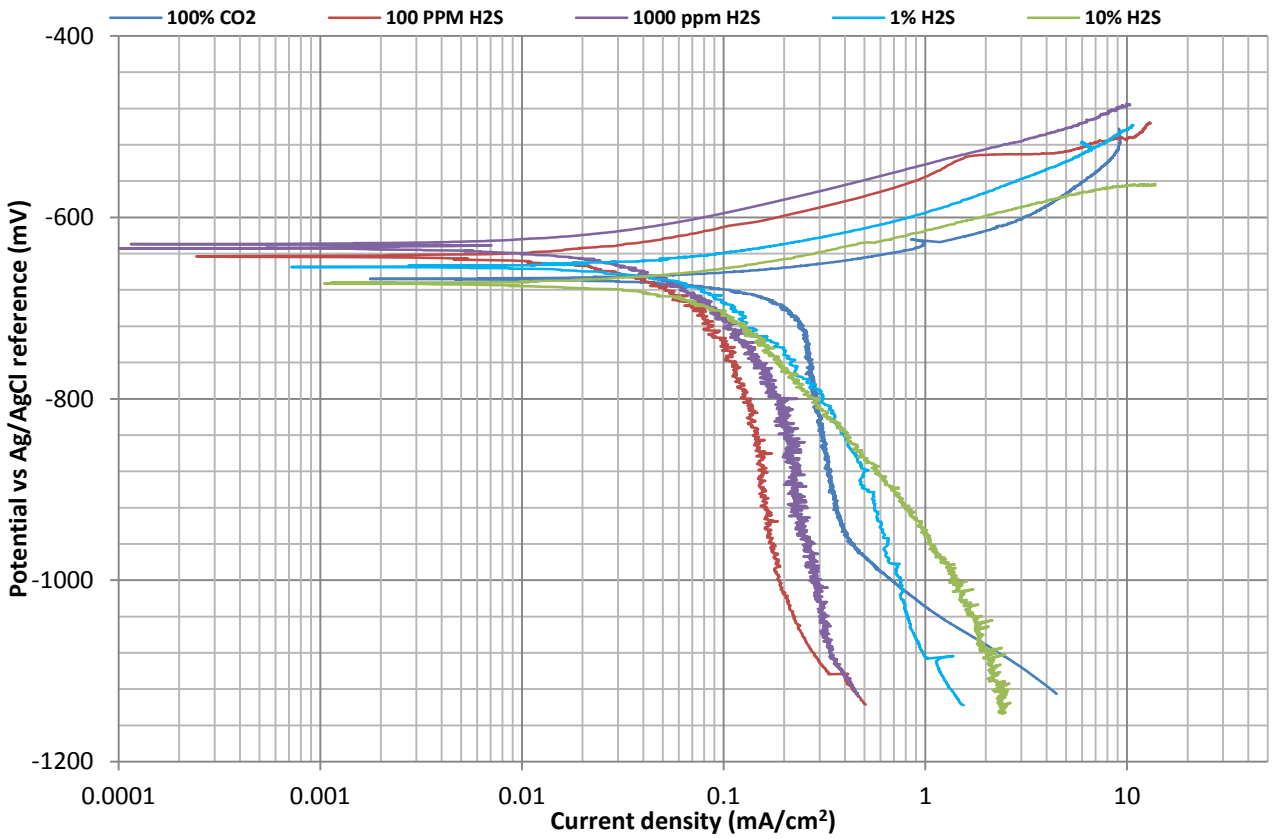
100% CO2
100 PPM H2S
1000 ppm H2S
1% H2S
10% H2S
-400
-600
-800
-1000
-1200
Potential vs Ag/AgCl reference (mV)
0.0001
0.001
0.01
0.1
1
10
Current density (mA/cm²)

A

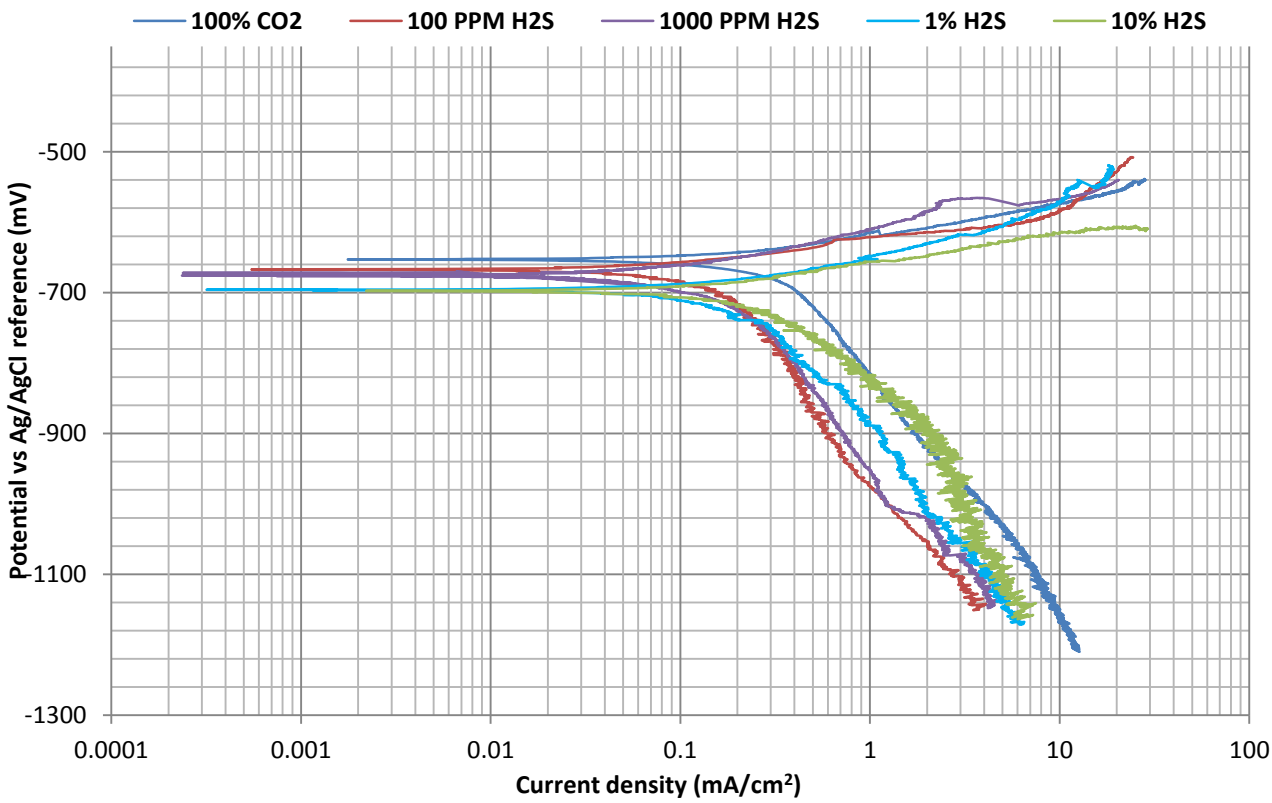
100% CO2
100 PPM H2S
1000 PPM H2S
1% H2S
10% H2S
-500
-700
-900
-1100
-1300
Potential vs Ag/AgCl reference (mV)
0.0001
0.001
0.01
0.1
1
10
100
Current density (mA/cm²)

B

Figure 2: Tafel polarization plots for X65 carbon steel in 3.5 wt. % NaCl solutions saturated with different combination of H_2S and CO_2 gas at (a) 30°C and (b) 80°C after 5 hours exposure.

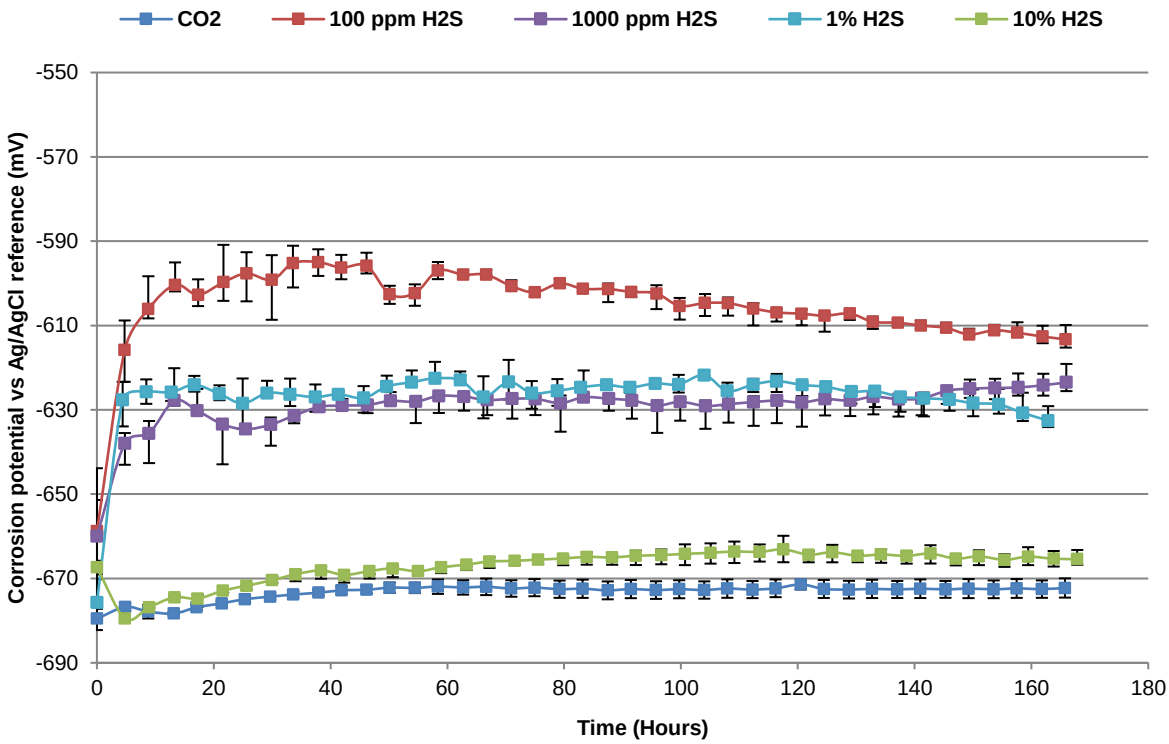

A

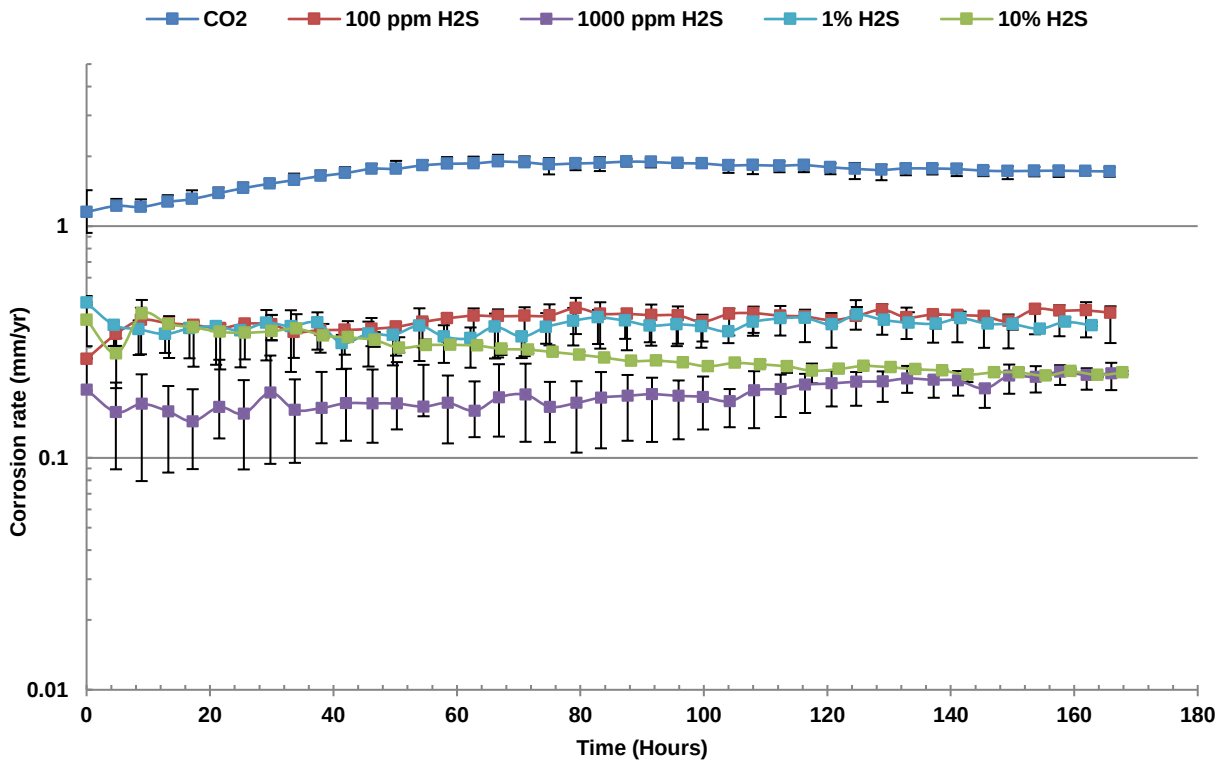

B

Figure 3: Graphs of (a) corrosion potential and (b) corrosion rate of X65 carbon steel in 3.5 wt.% NaCl solution under different combination of H_2S-CO_2 gas at 30℃ over 168 hours.

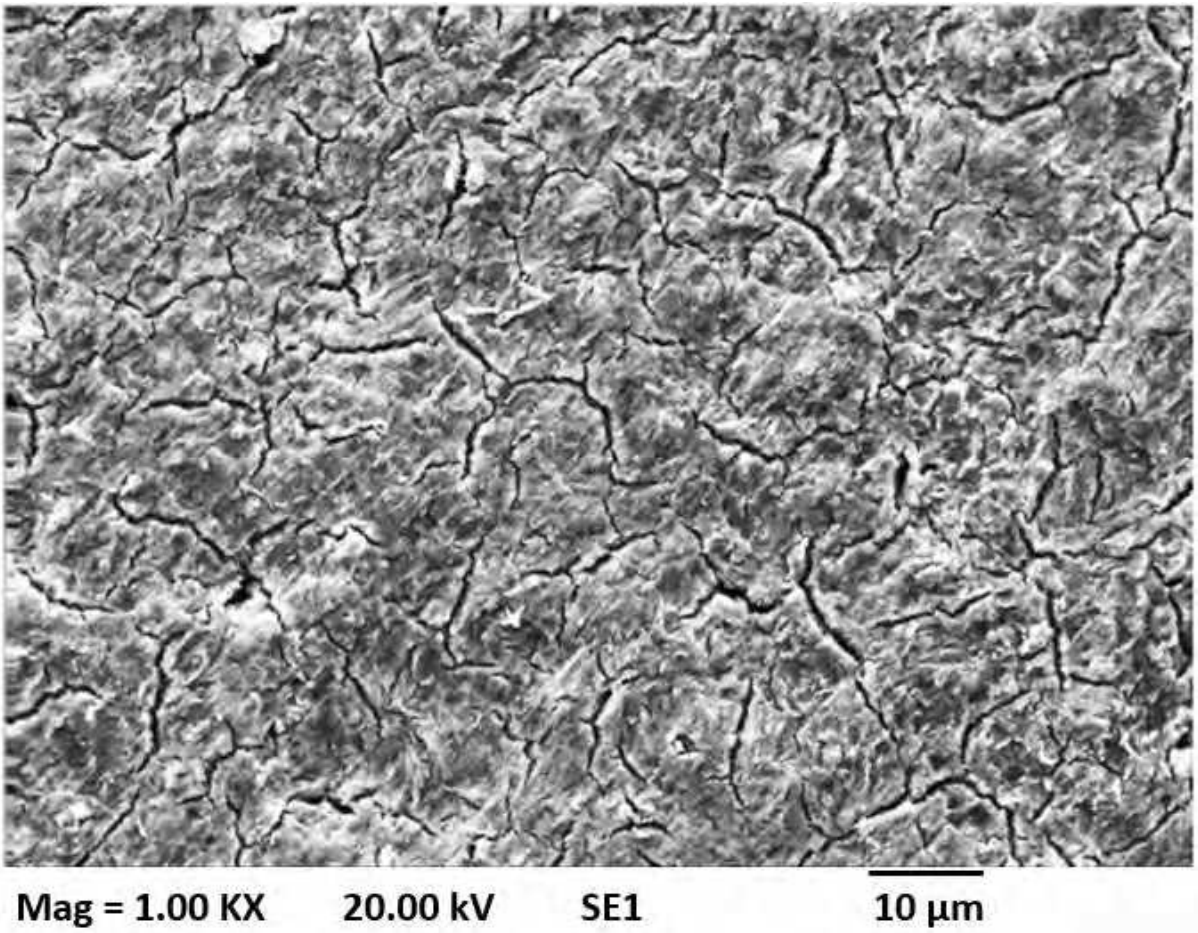

A

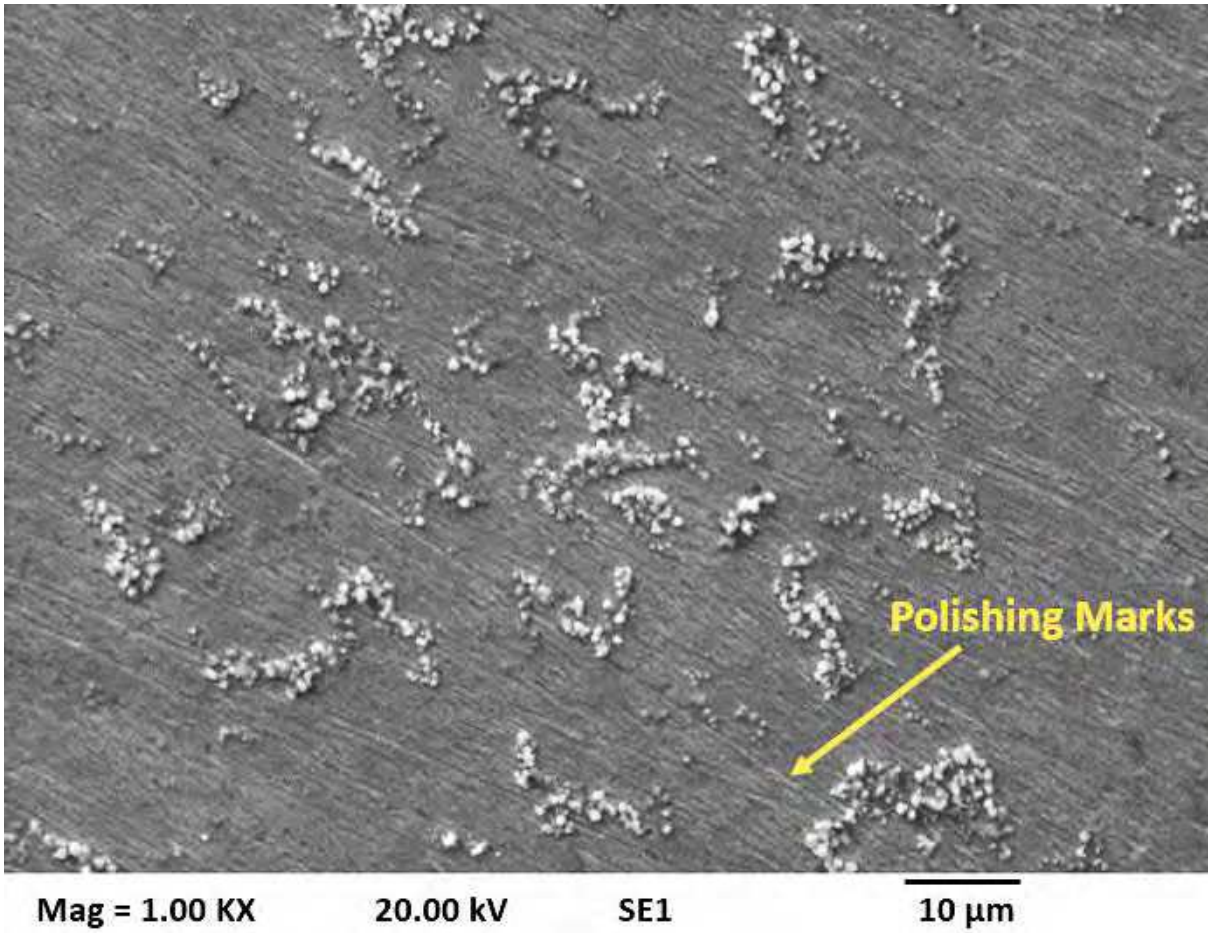

B

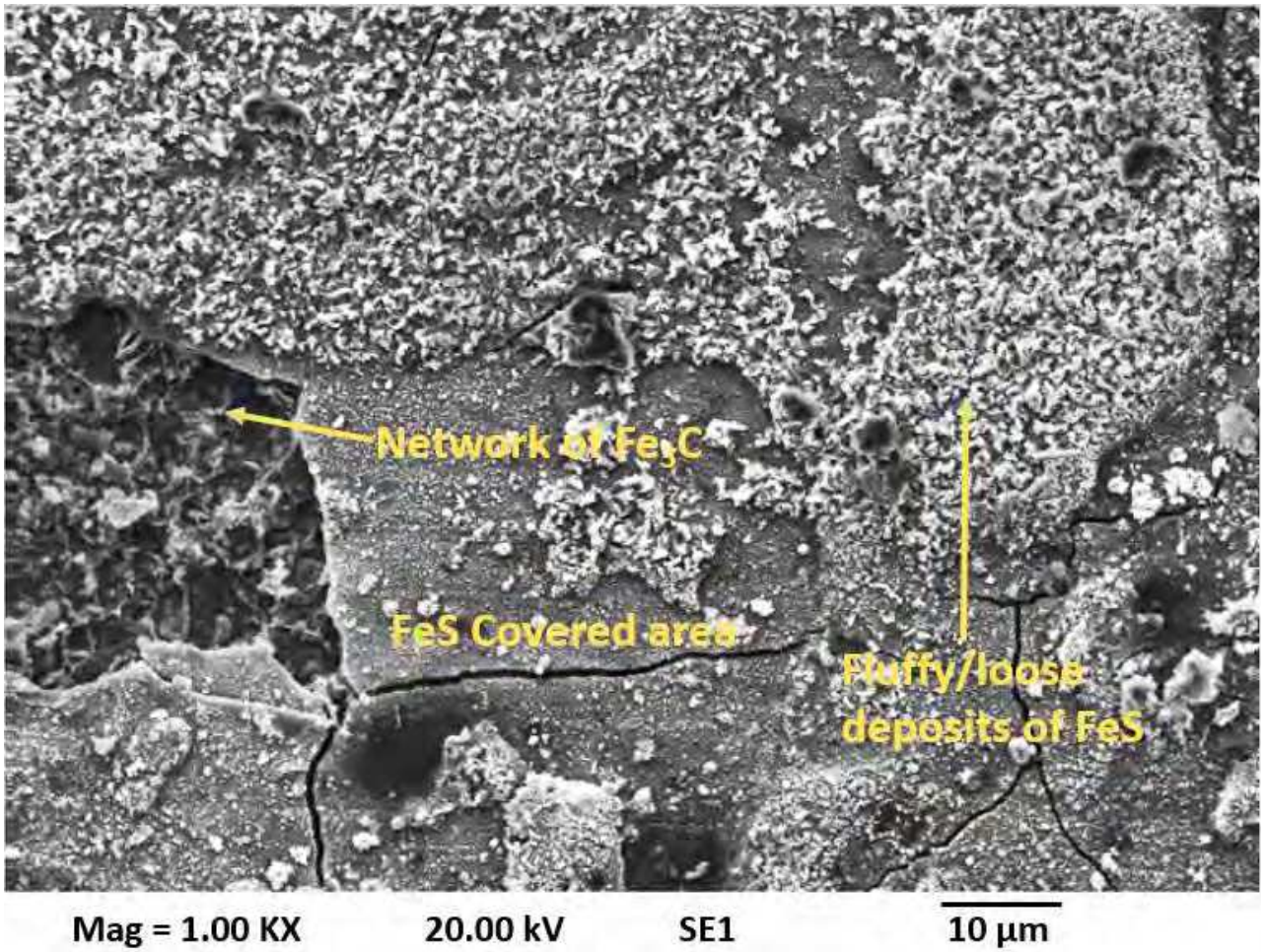
Network of Fe_3C
FeS Covered area
Fluffy/loose deposits of FeS
Mag = 1.00 KX
20.00 kV
SE1
10 µm

C

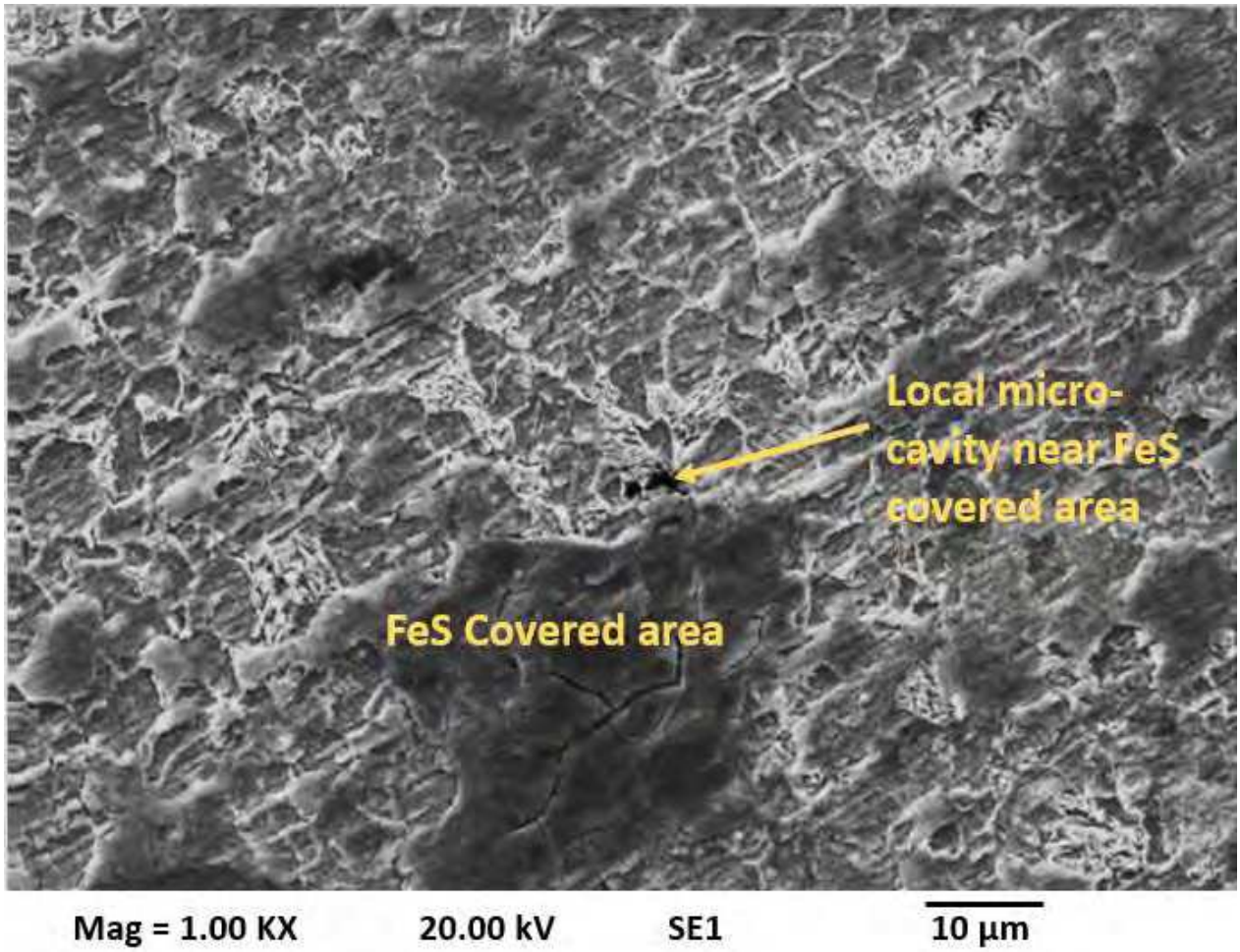
Local micro-
cavity near FeS
covered area
FeS Covered area
Mag = 1.00 KX
20.00 kV
SE1
10 µm

D

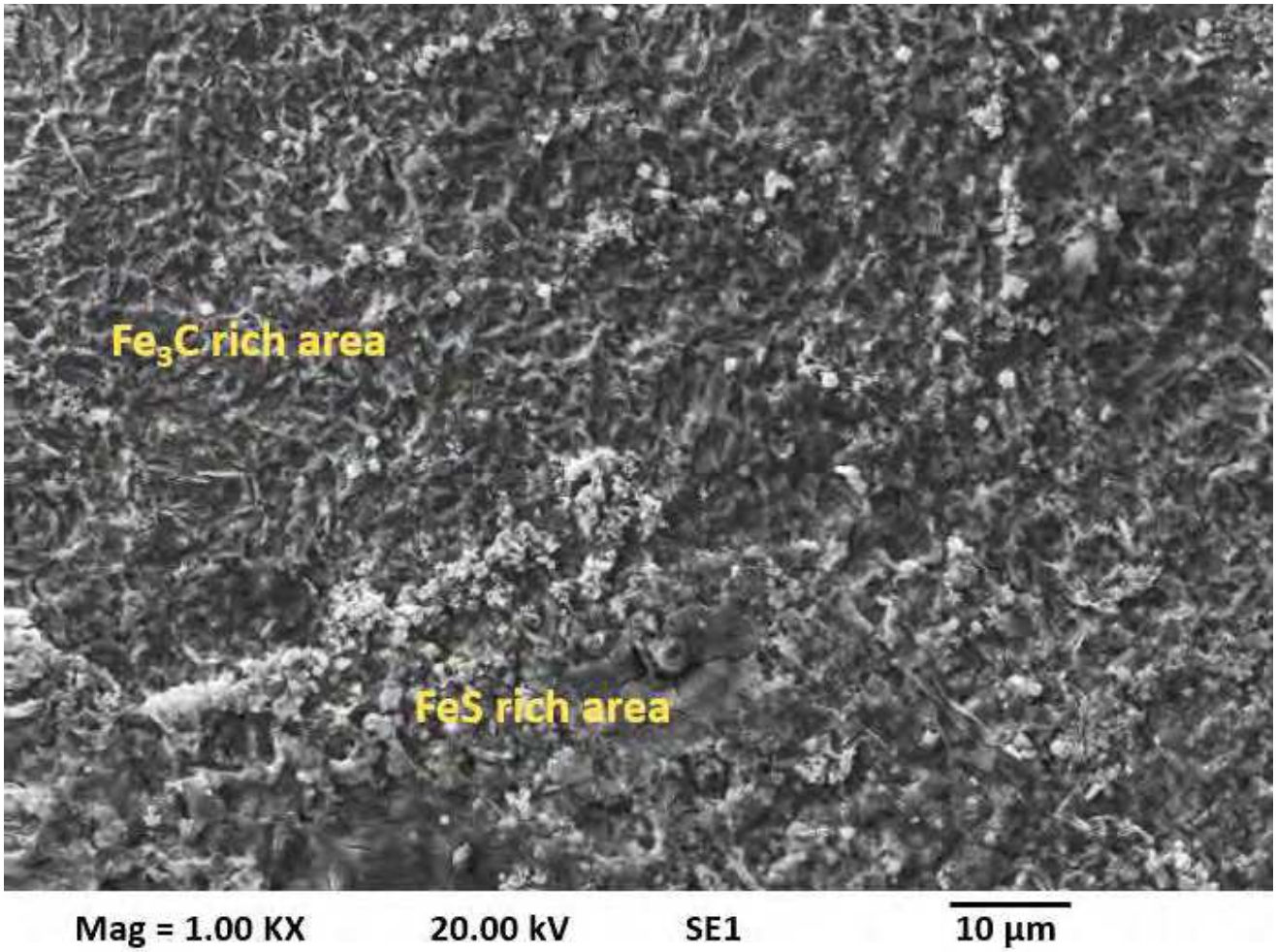

E

Figure 4: SEM images of corrosion product layer on X65 carbon steel in 3.5 wt. % NaCl solution under different combinations of H_2S-CO_2 gas;(a) 100 mol.% CO_2 , (b) 100 ppm of H_2S gas, (c) 1000 ppm of H_2S gas, (d) 1% of H_2S gas (e) 10% of H_2S gas at 30℃ and after 168 h.

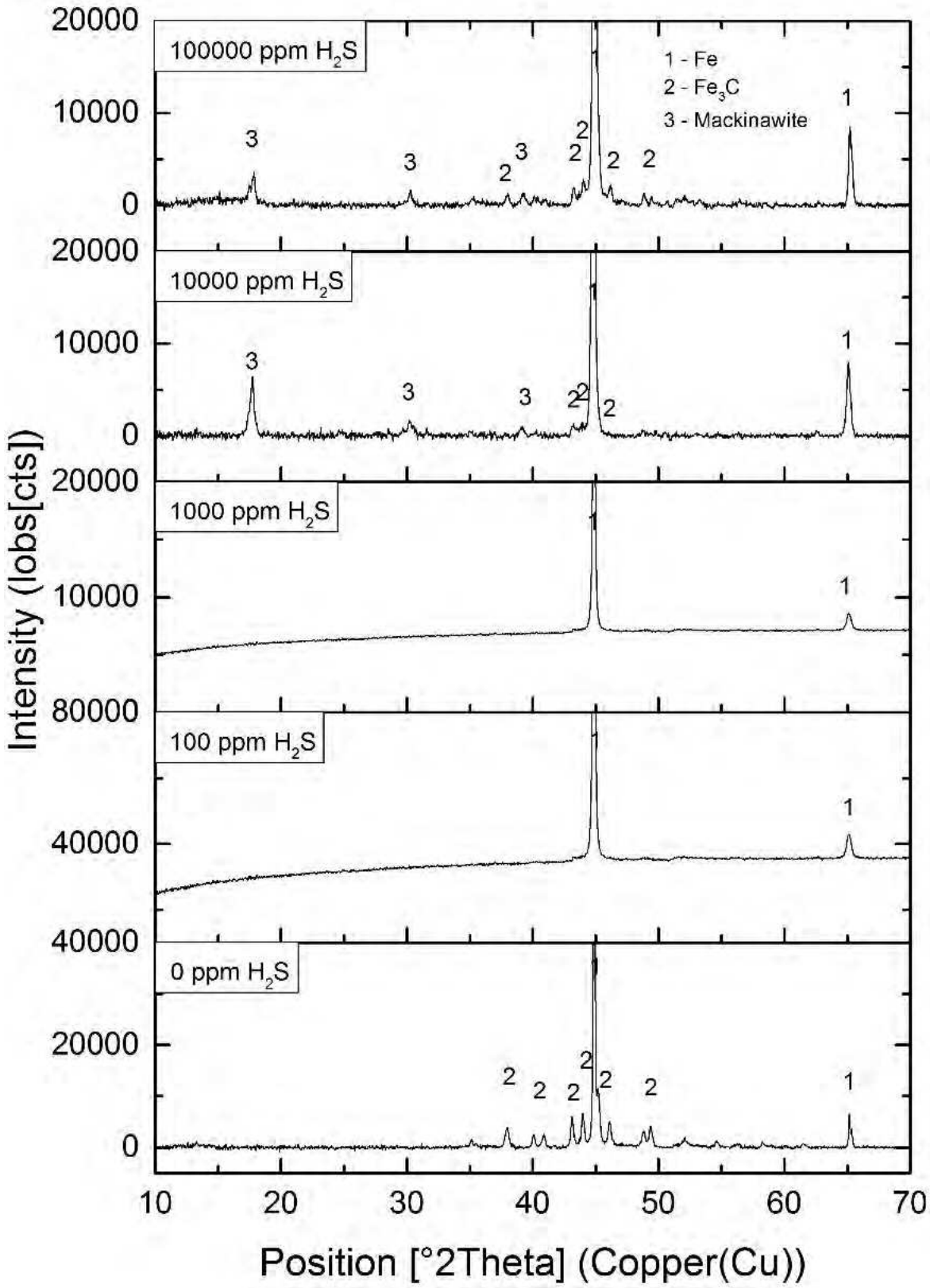

Figure 5: XRD patterns for corrosion products formed on X65 carbon steel in 3.5 wt. % NaCl solution under different combinations of H_2S-CO_2 gas at 30℃ after 168 h.

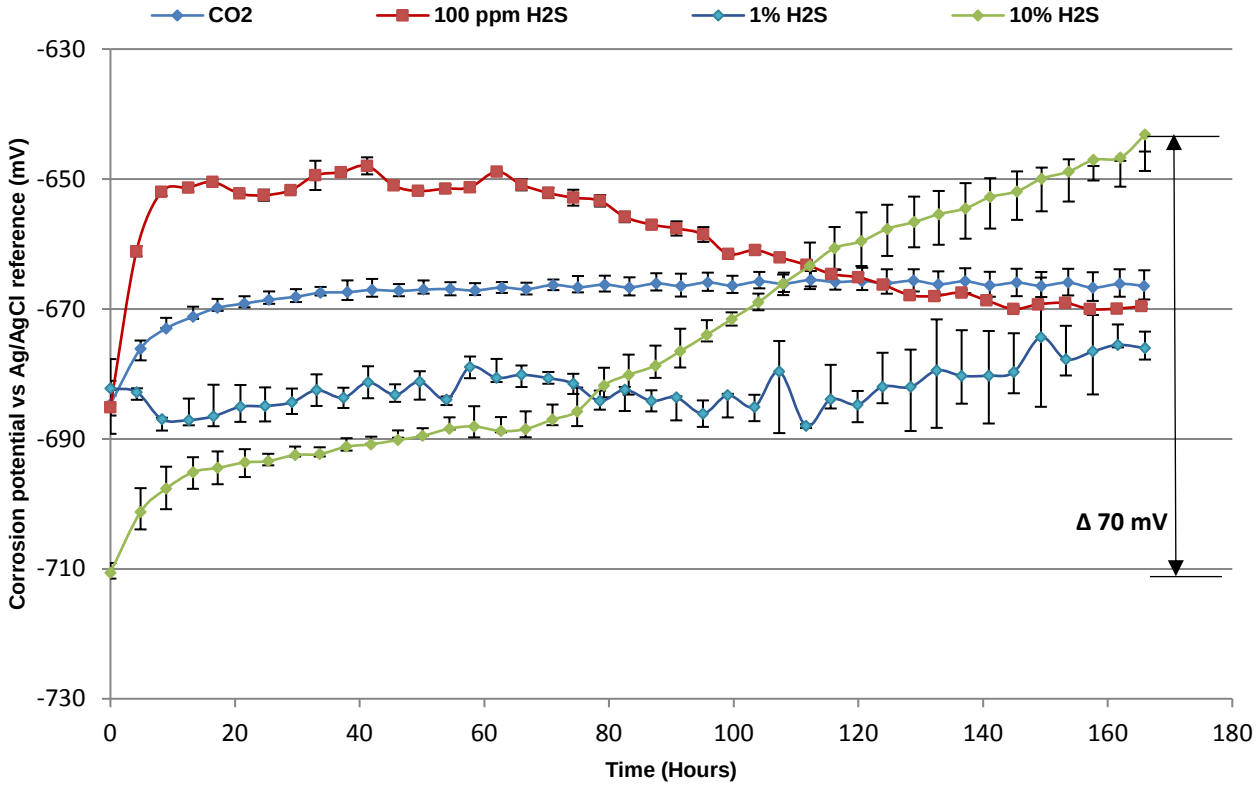

A

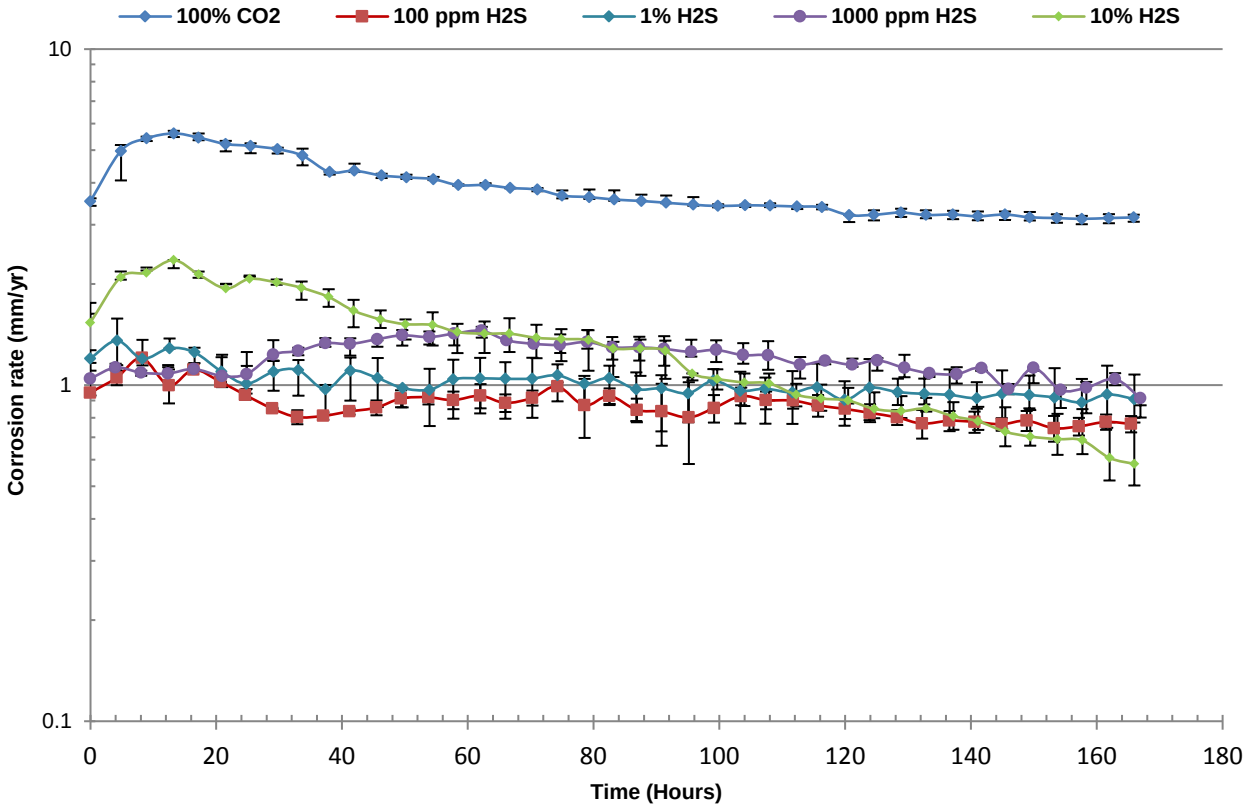

B

Figure 6: Graphs of (a) corrosion potential and (b) corrosion rate of X65 carbon steel in 3.5 wt. % NaCl solution under different combination of H_2S-CO_2 gas at 80℃, over 168 h.

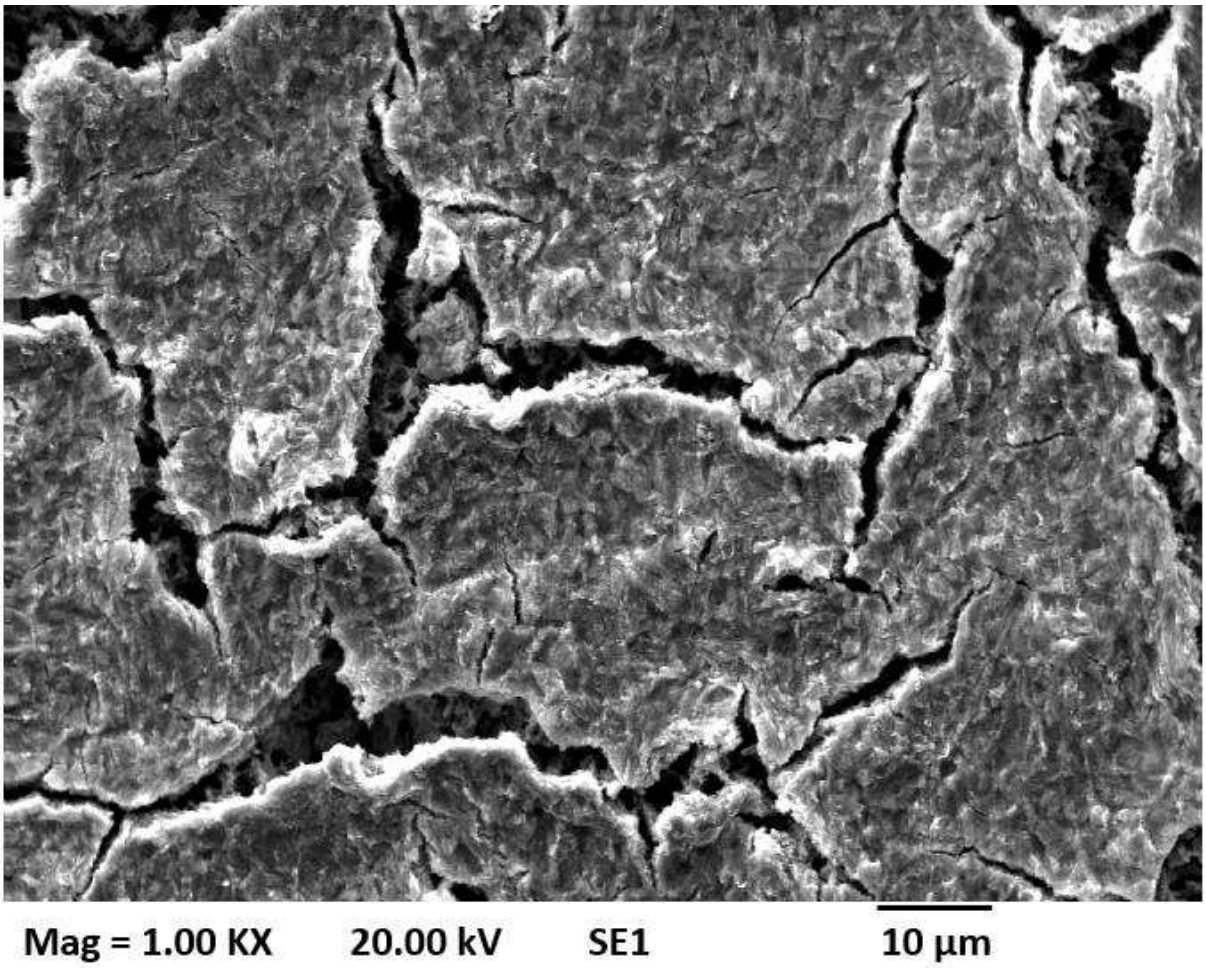

A

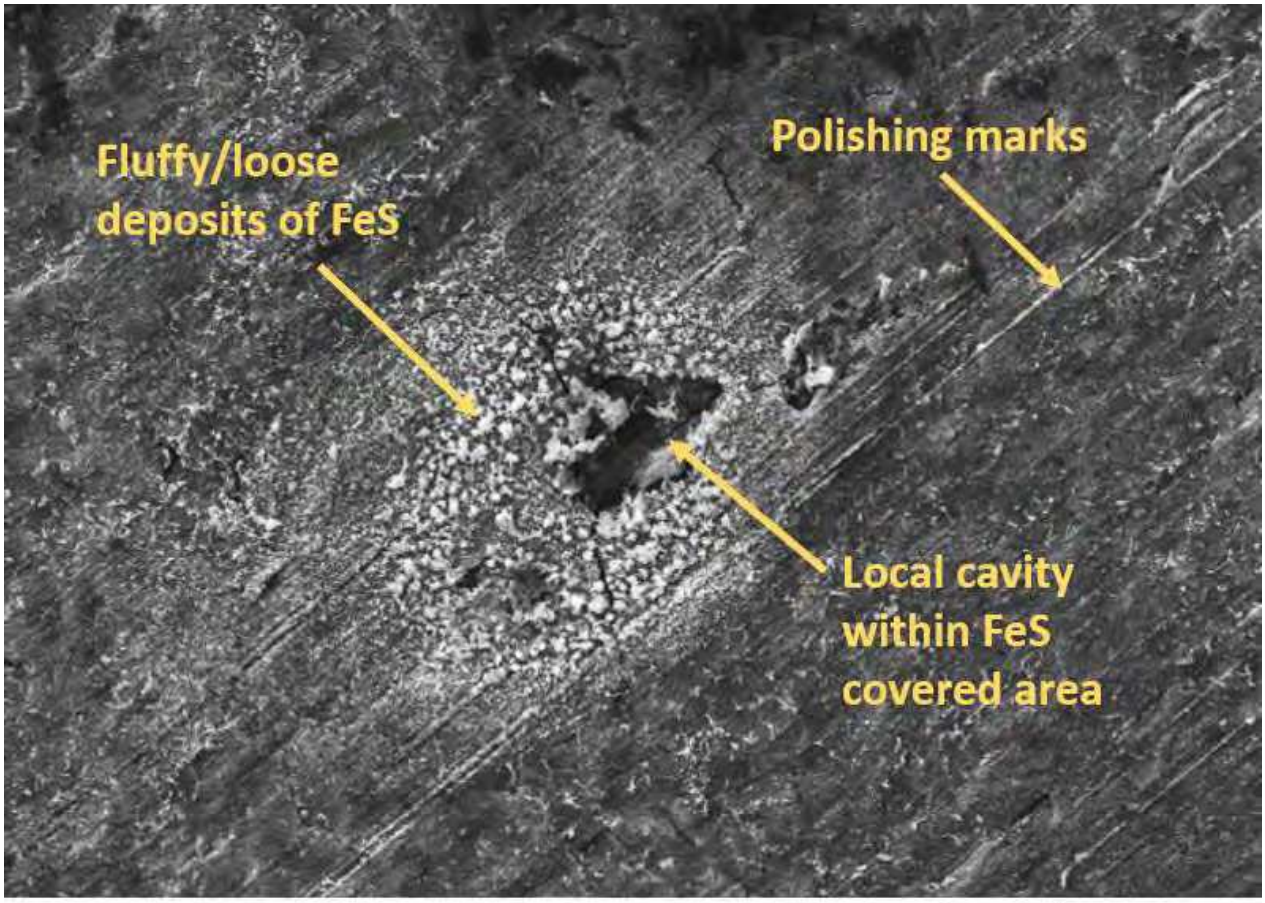

Mag = 1.00 KX 20.00 kV SE1 10 µm

B

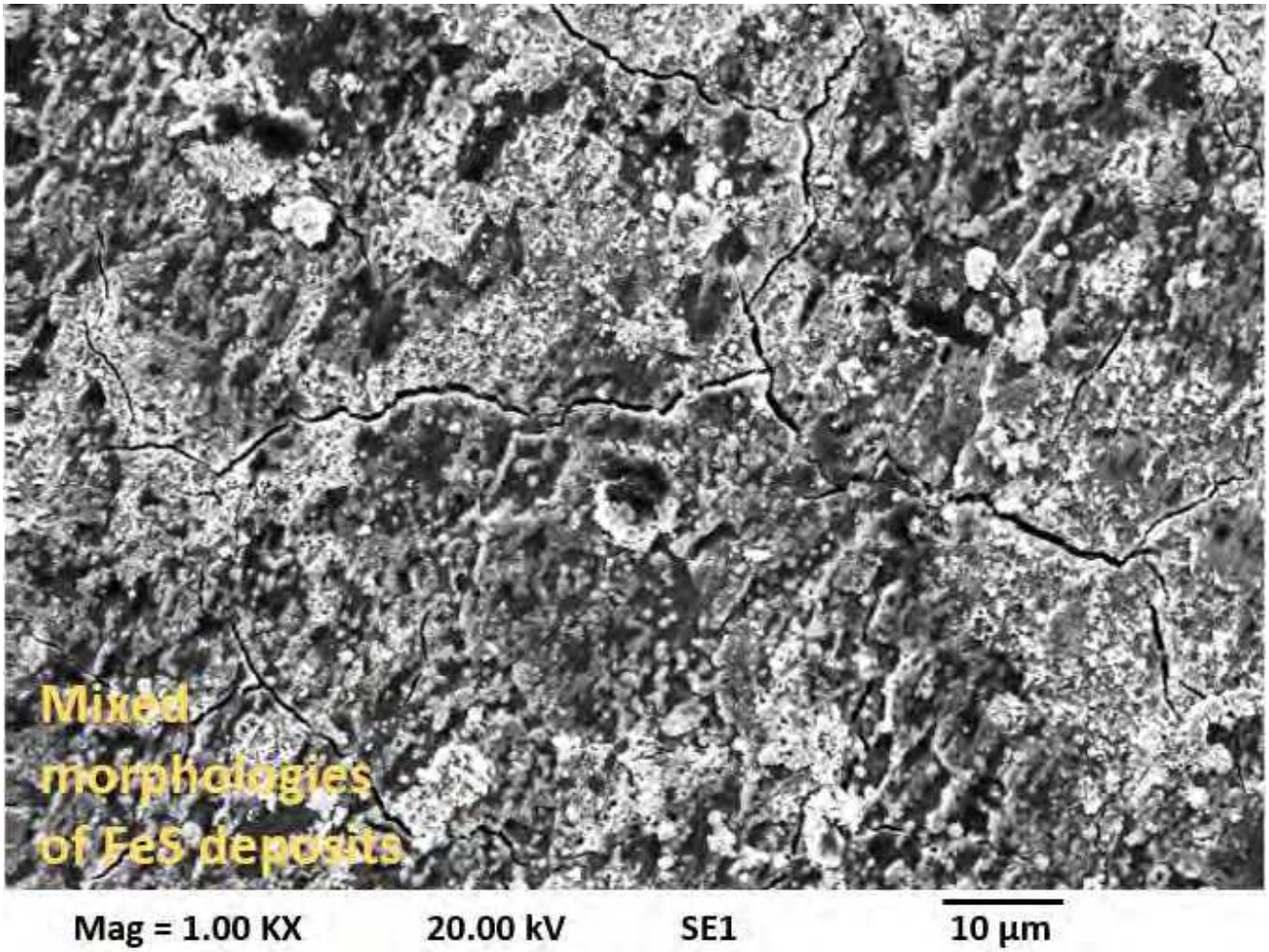
Mixed
morphologies
of FeS deposits
Mag = 1.00 KX
20.00 kV
SE1
10 µm

c

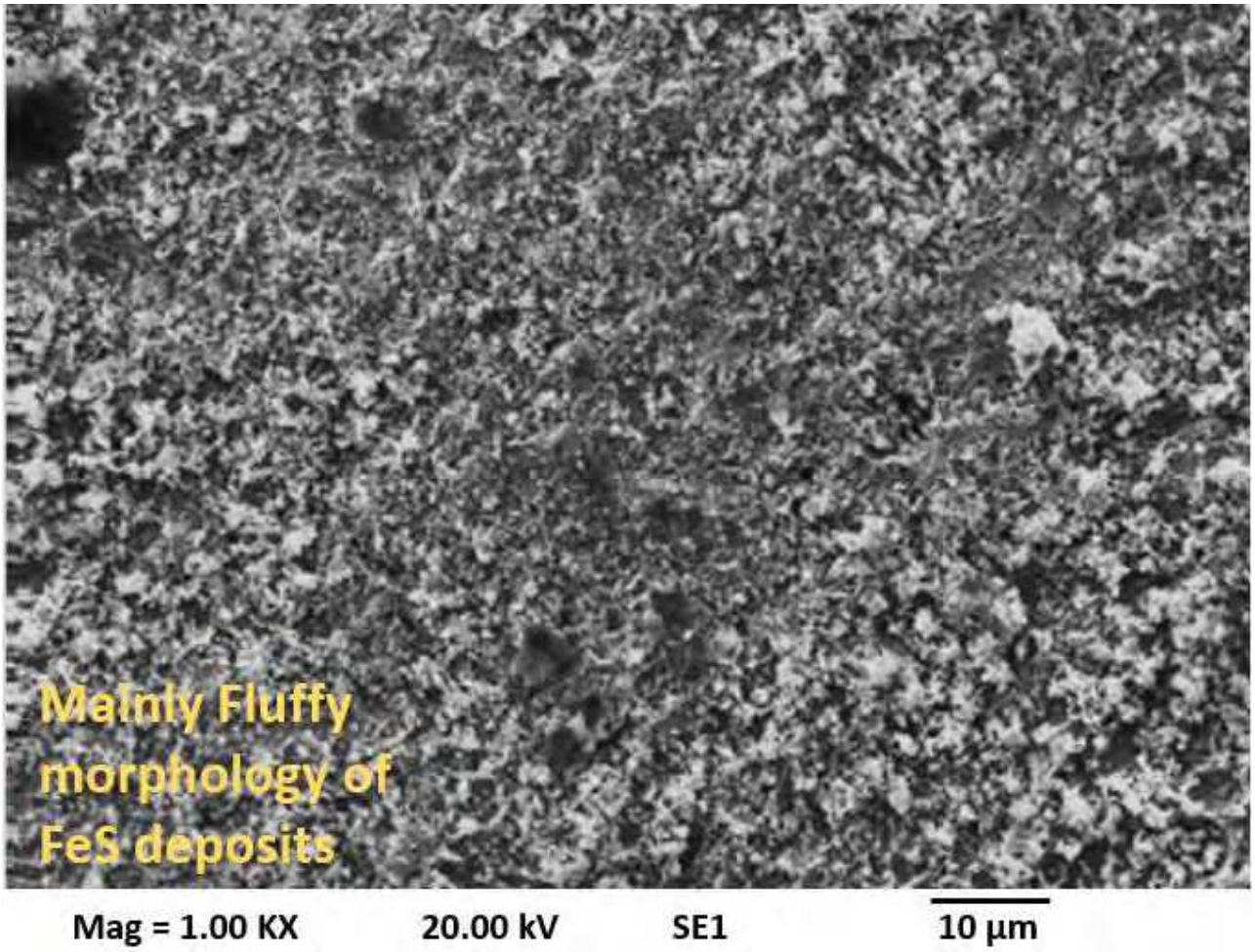
Mainly Fluffy
morphology of
FeS deposits
Mag = 1.00 KX
20.00 kV
SE1
10 µm

D

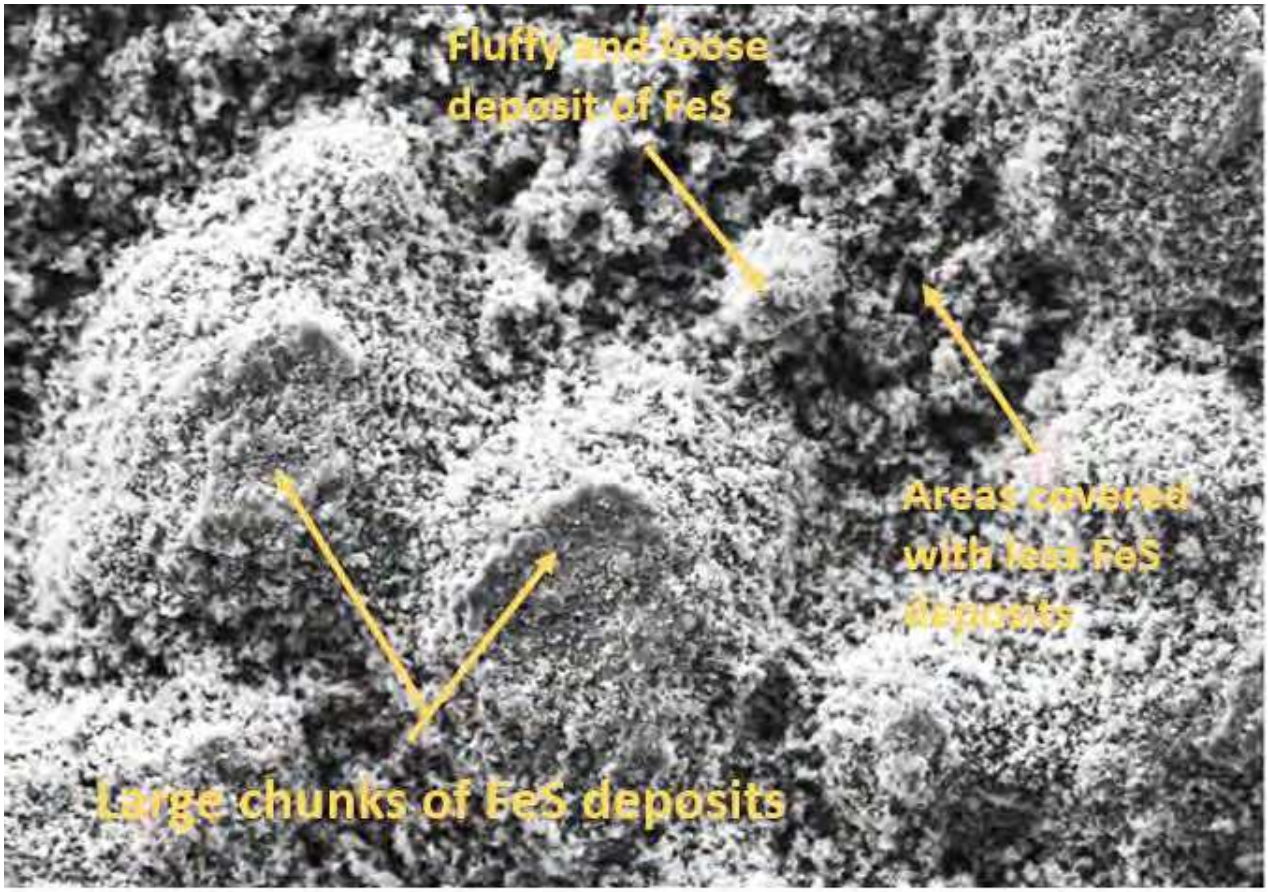

Mag = 1.00 KX 20.00 kV SE1 10 µm

E

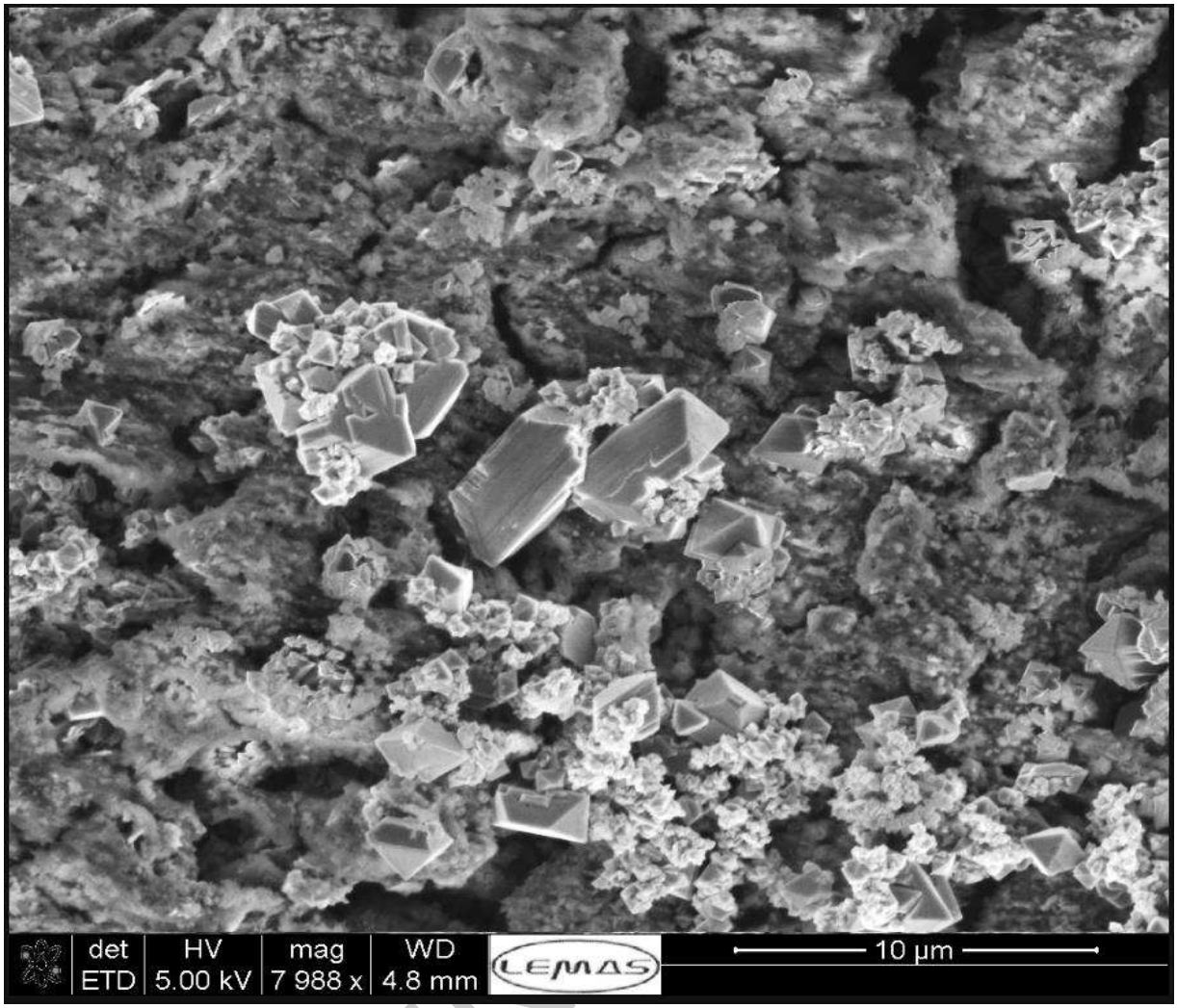

F

Figure 7: SEM images of corrosion product layer on X65 carbon steel in 3.5 wt. % NaCl solution under different combinations of H_2S-CO_2 gas;(a) 100 mol. % CO_2, (b) 100 ppm of H_2S gas, (c) 1000 ppm of H_2S gas, (d) 1% of H_2S gas (e) 10% of H_2S (f) 10% of H_2S (Higher Magnification) gas at 80℃ and after 168 h.

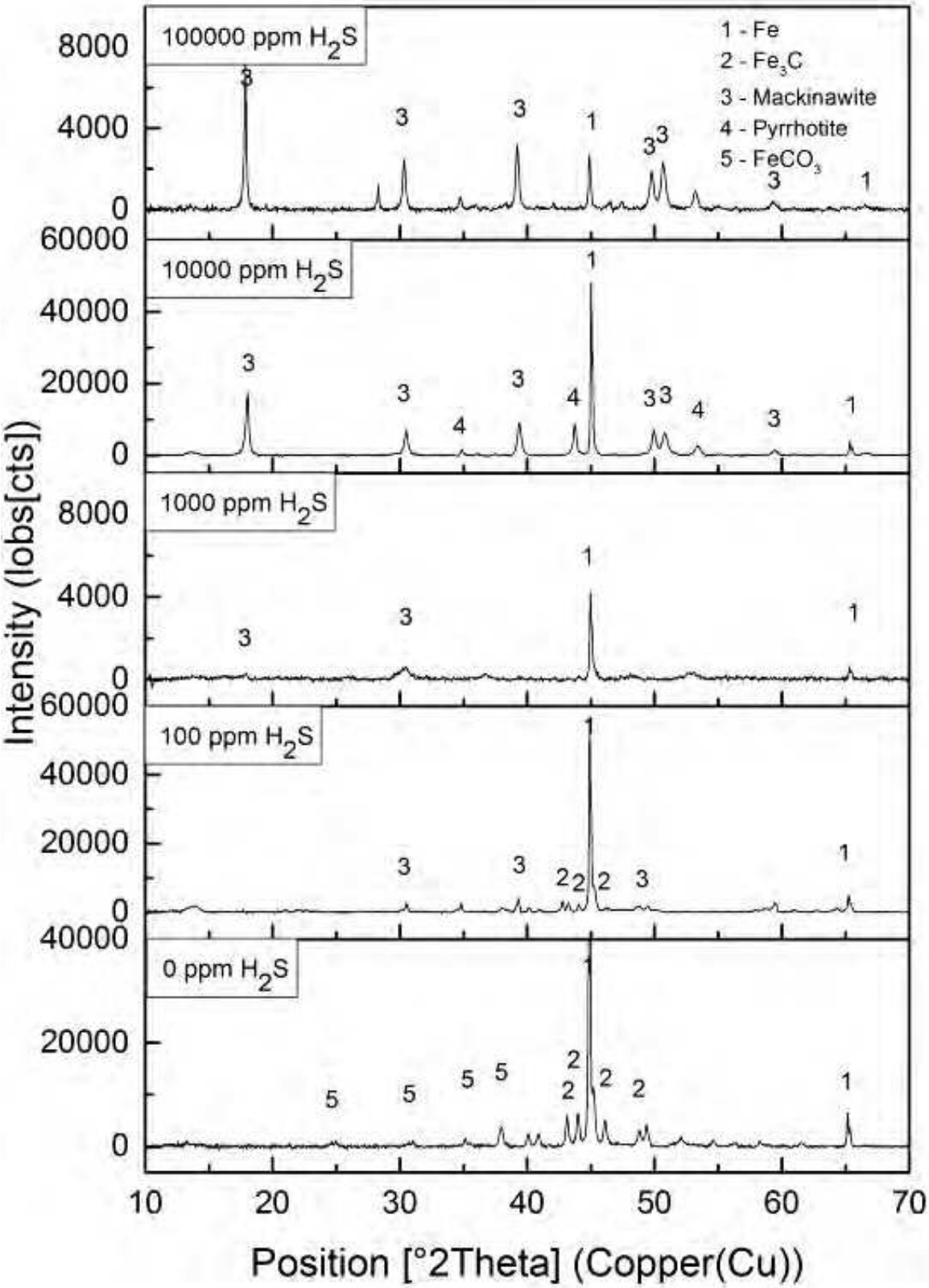

Figure 8: XRD patterns for corrosion products formed on X65 carbon steel in 3.5 wt.% NaCl solution under different combinations of H_2S-CO_2 gas at 80℃ after 168 h.

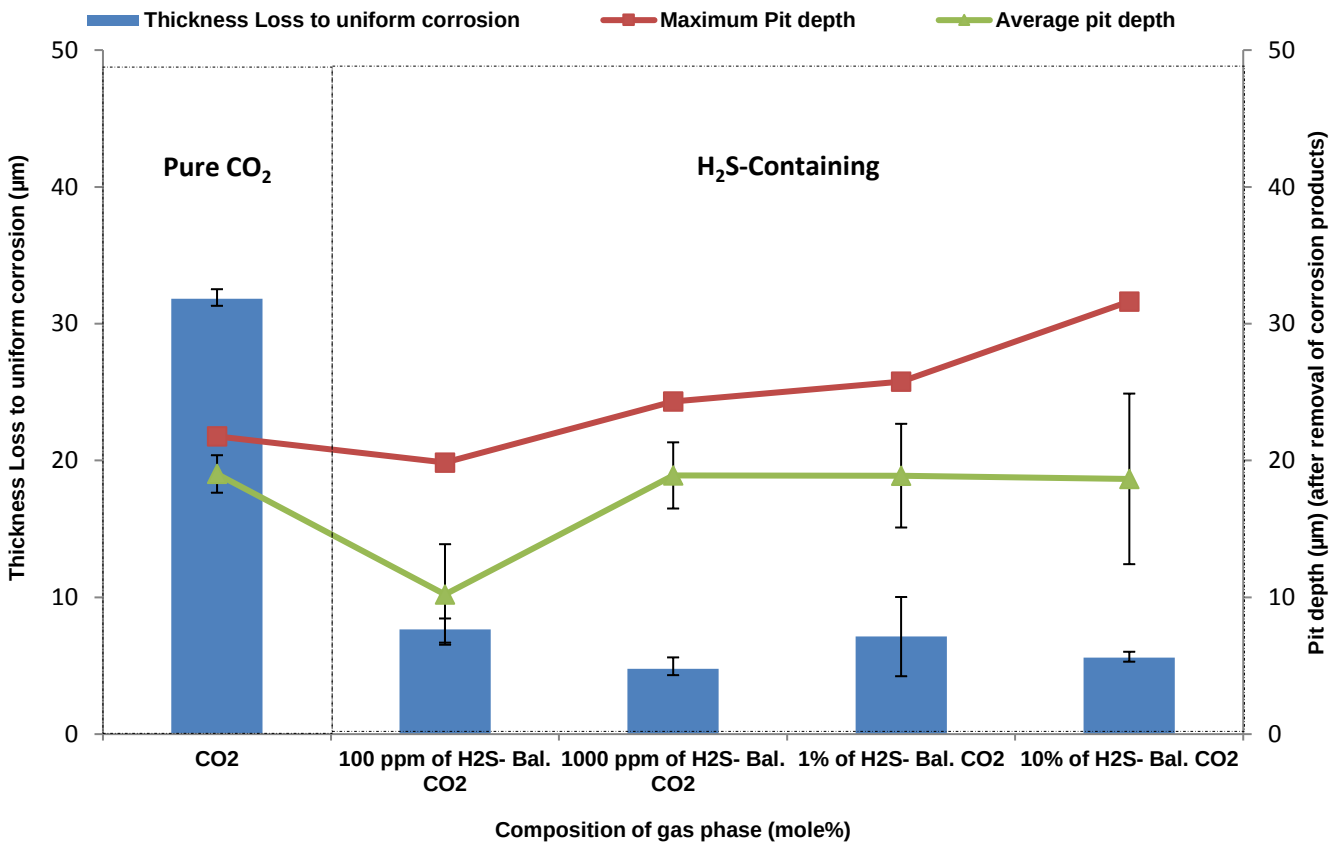

Figure 9: Contribution of thickness loss to uniform corrosion and pit depths (relative to corroded surface) of X65 carbon steel in 3.5 wt. % NaCl solution under exposed to different combination of H_2S-CO_2 gas at 30℃ for 168 h.

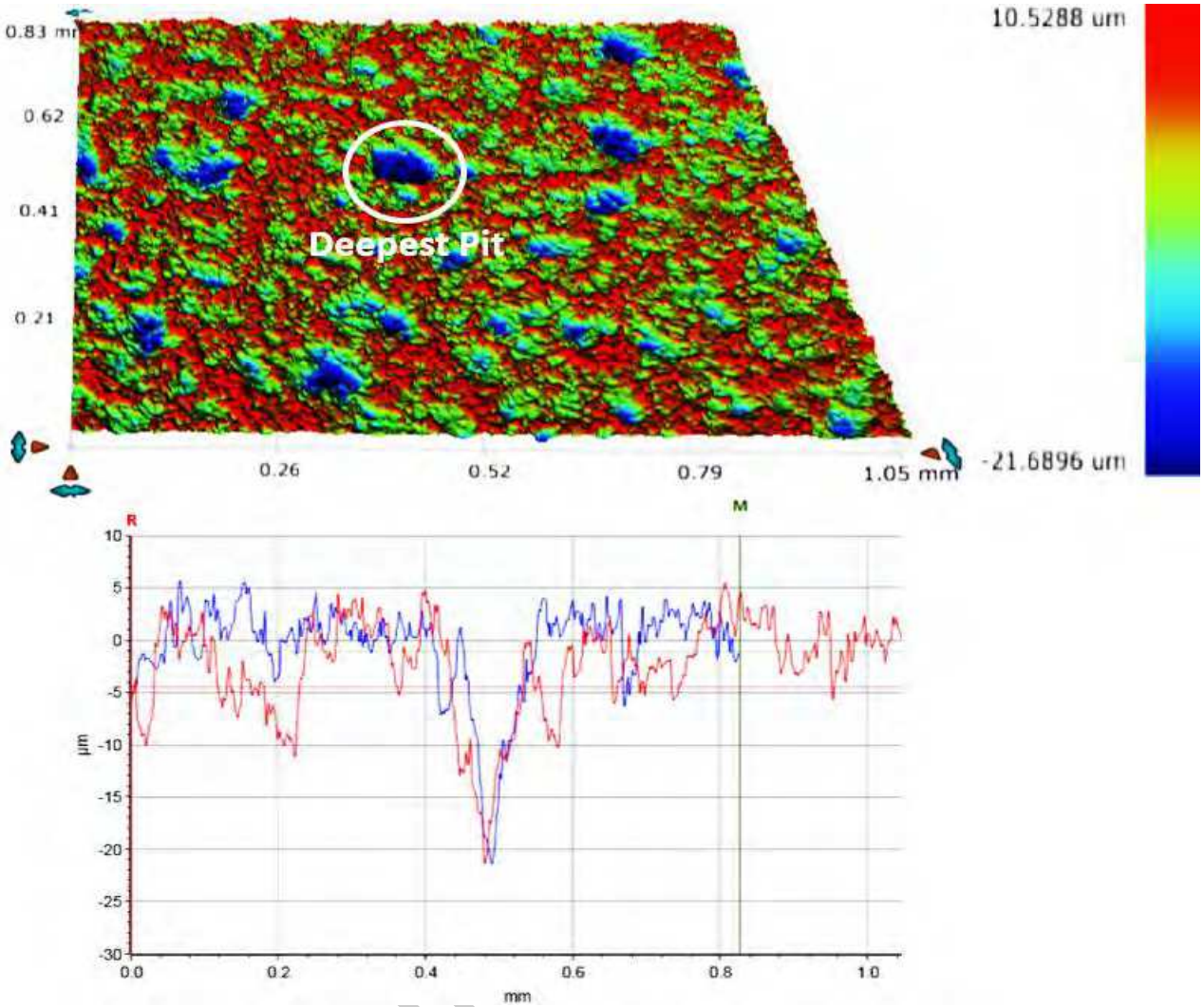
0.83 mm
0.62
0.41
0.21
Deepest Pit
0.26
0.52
0.79
1.05 mm
10.5288 um
-21.6896 um
R
M
µm
mm

A

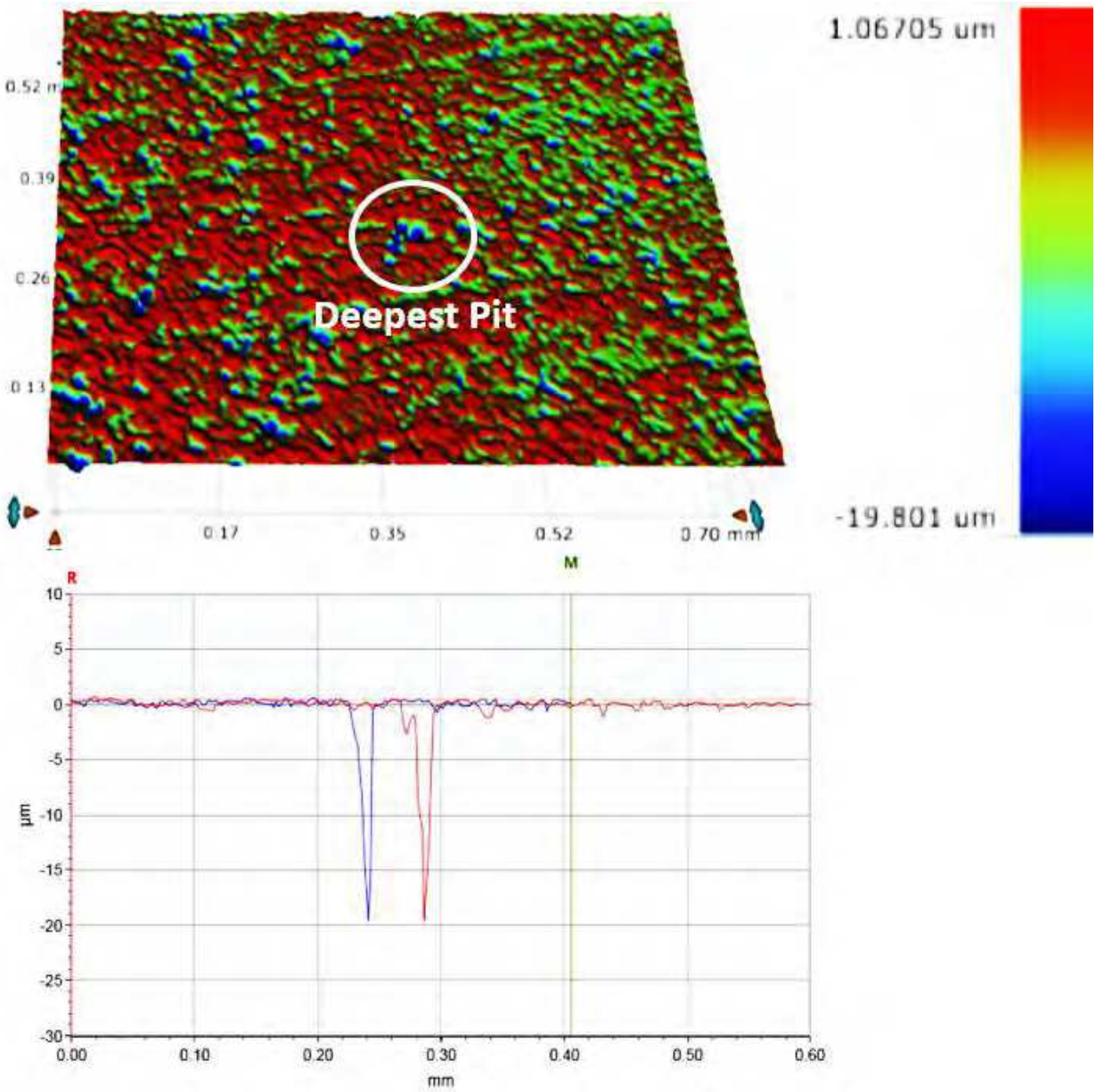
1.06705 um
-19.801 um
Deepest Pit
0.52 mm
0.39
0.26
0.13
0.17
0.35
0.52
0.70 mm
M
R
µm
mm
10
5
0
-5
-10
-15
-20
-25
-30
0.00
0.10
0.20
0.30
0.40
0.50
0.60

B

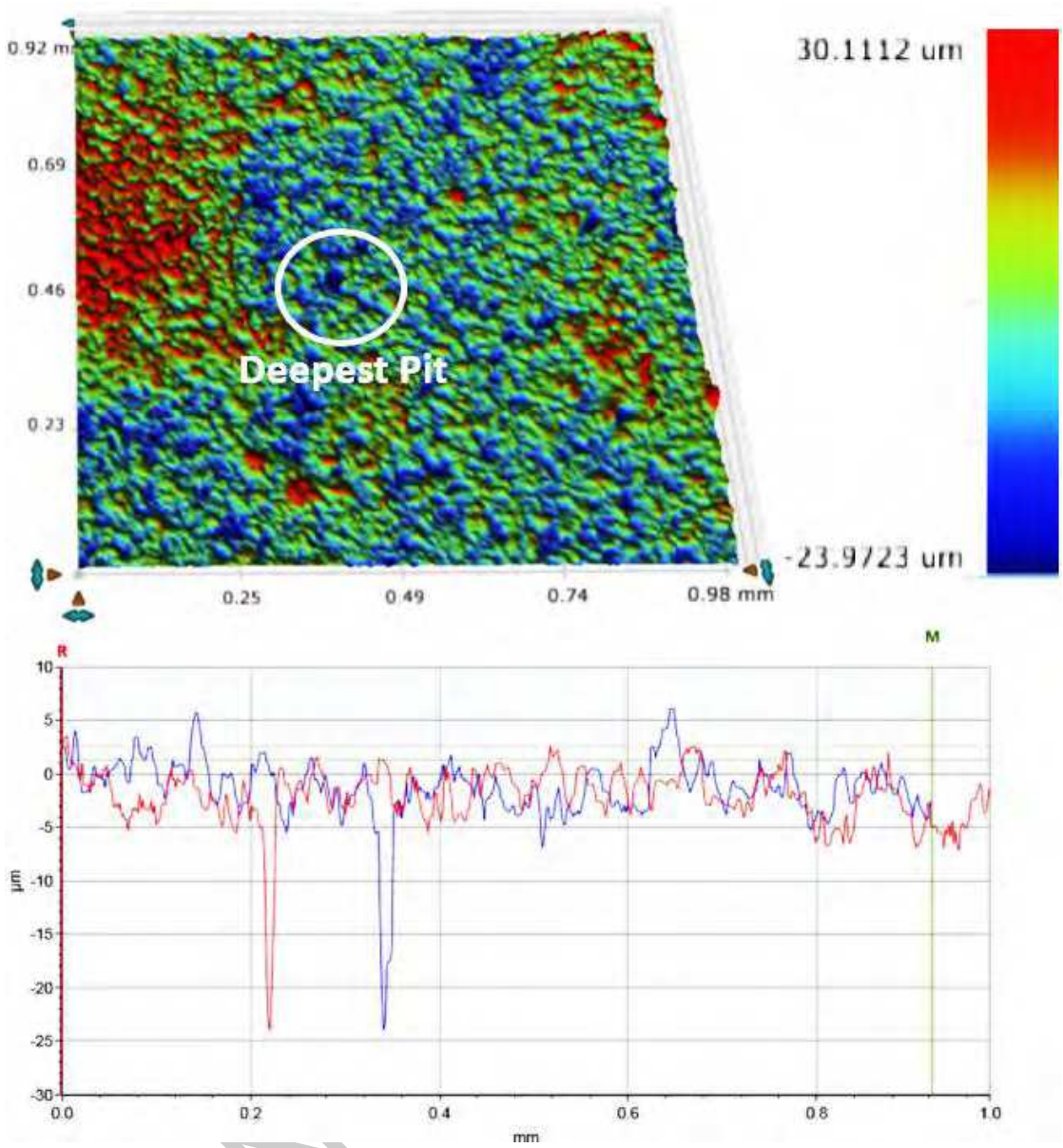
30.1112 um
-23.9723 um
Deepest Pit
0.92 mm
0.69
0.46
0.23
0.25
0.49
0.74
0.98 mm
R
M
µm
mm

C

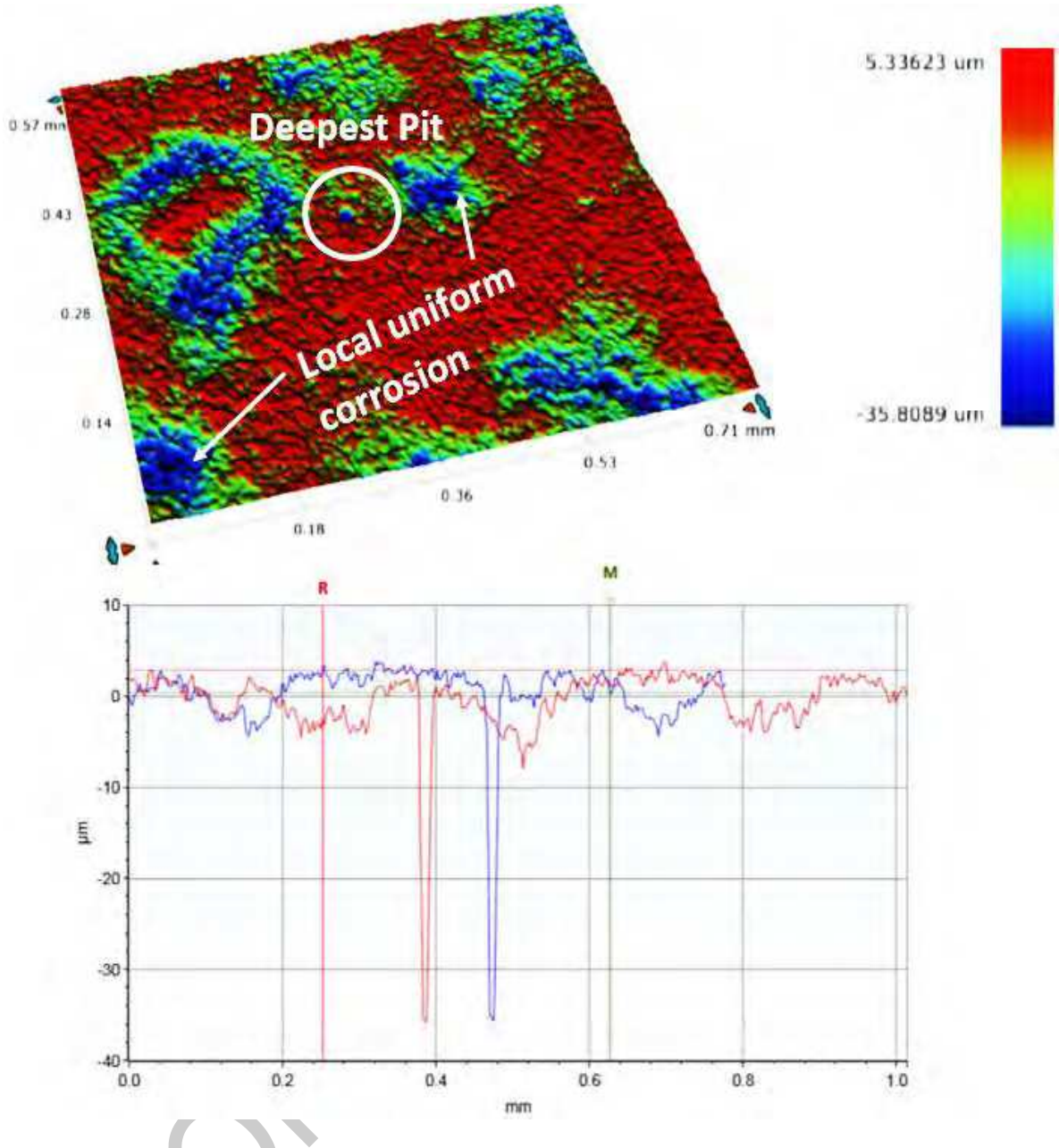

D

Figure 10: 3D images of pitting corrosion damage on carbon steel surface exposed to (a) pure CO_2, (b)100 ppm of H_2S, (c) 1000 ppm of H_2S and (d) 10% of H_2S corrosion system after 168 hours at 30℃.

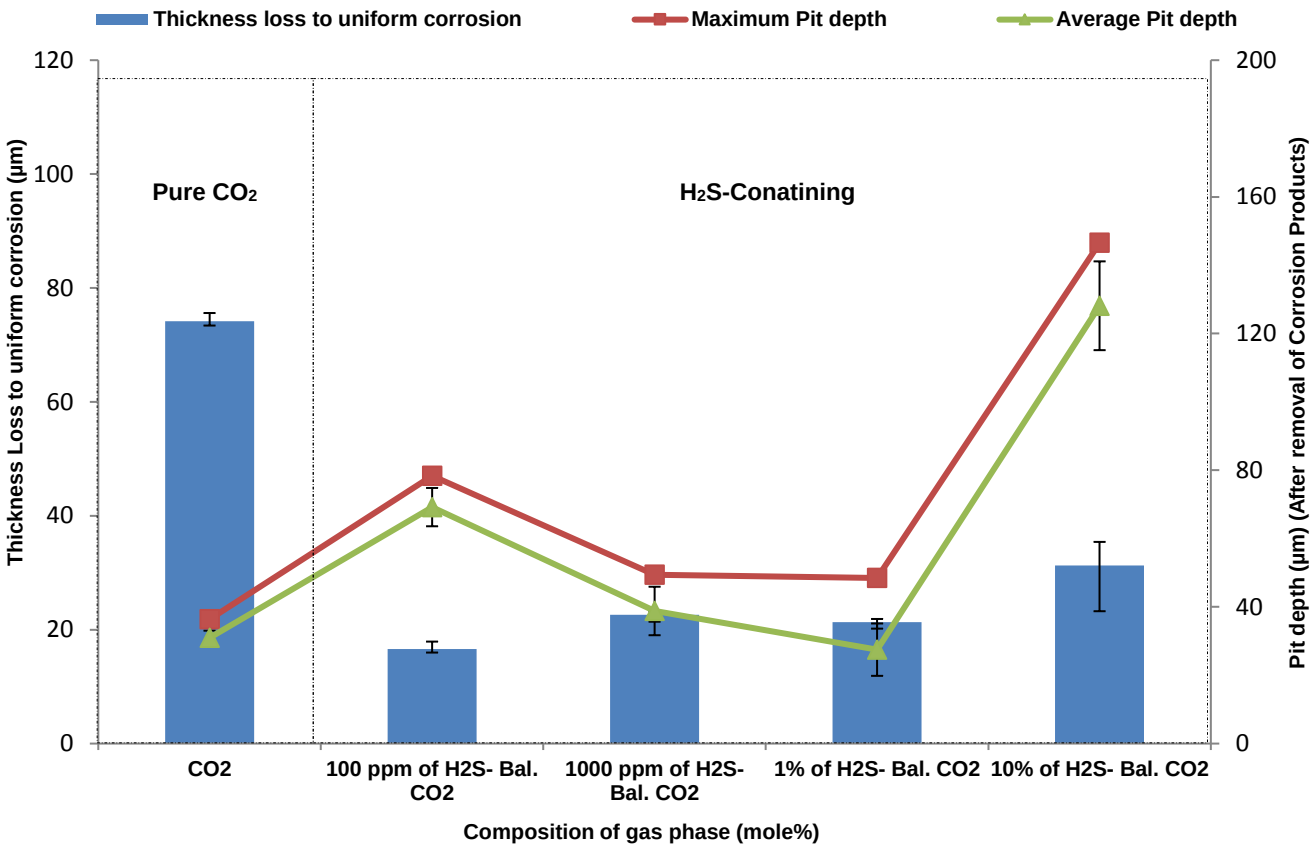

Figure 11: Contribution of thickness loss to uniform corrosion and pit depths (relative to corroded surface) of X65 carbon steel in 3.5 wt. % NaCl solution under exposed to different

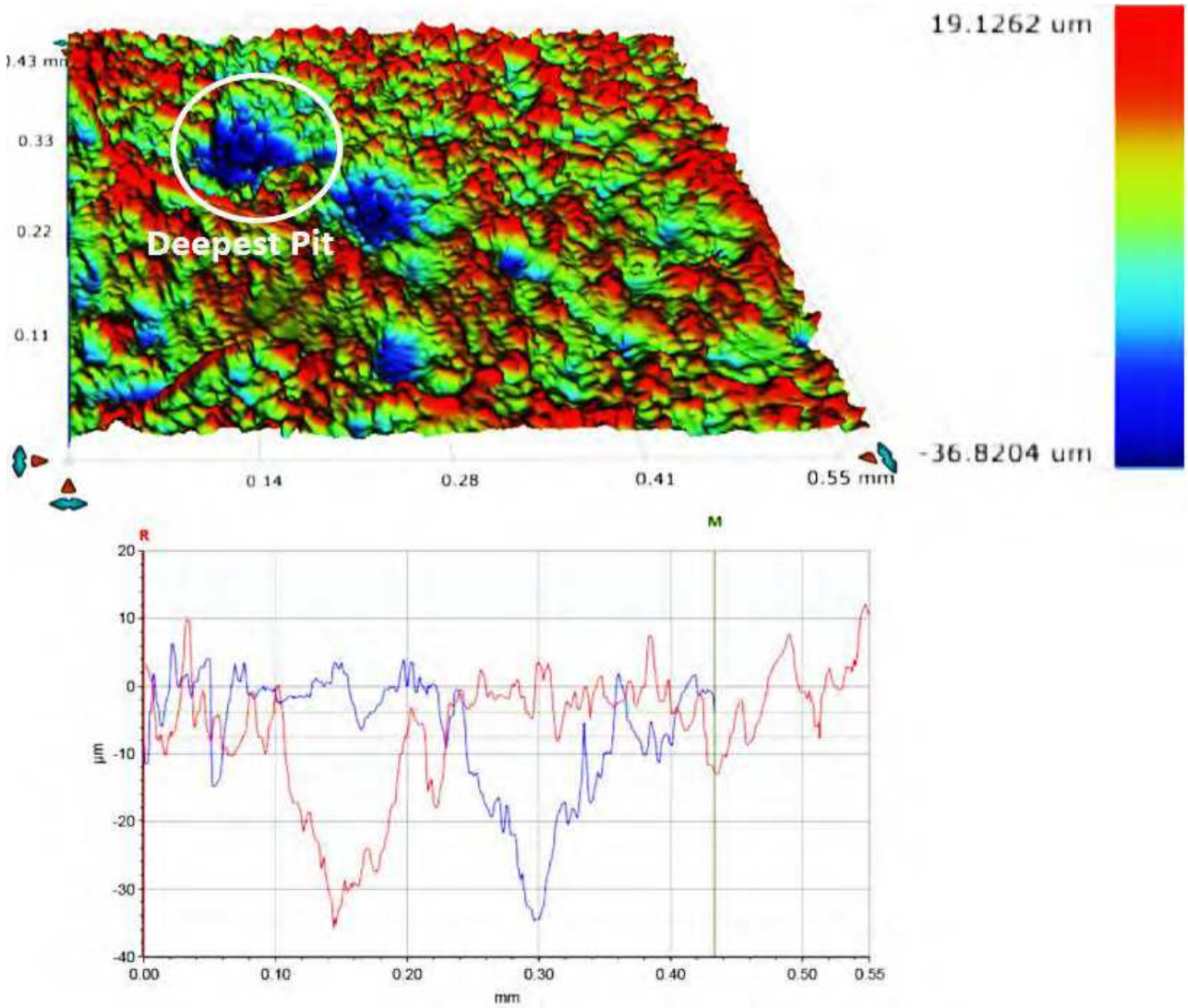
19.1262 um
-36.8204 um
Deepest Pit
0.33
0.22
0.11
0.14
0.28
0.41
0.55 mm
R
M
20
10
0
-10
-20
-30
-40
µm
0.00
0.10
0.20
0.30
0.40
0.50
0.55
mm

A

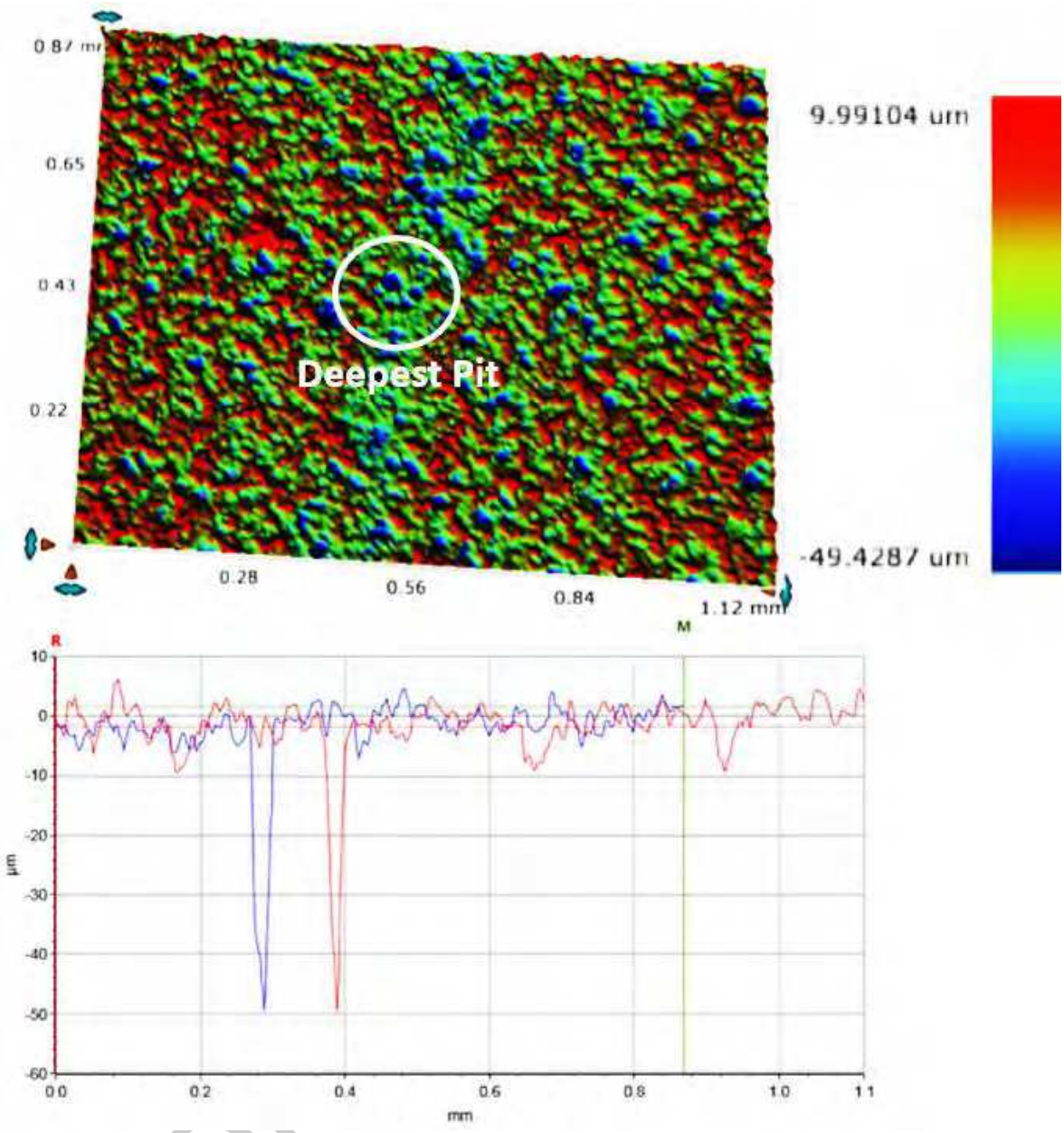
0.87 mm
0.65
0.43
0.22
0.28
0.56
0.84
1.12 mm
9.99104 um
-49.4287 um
Deepest Pit
R
M
10
0
-10
-20
-30
-40
-50
-60
µm
0.0
0.2
0.4
0.6
0.8
1.0
1.1
mm

B

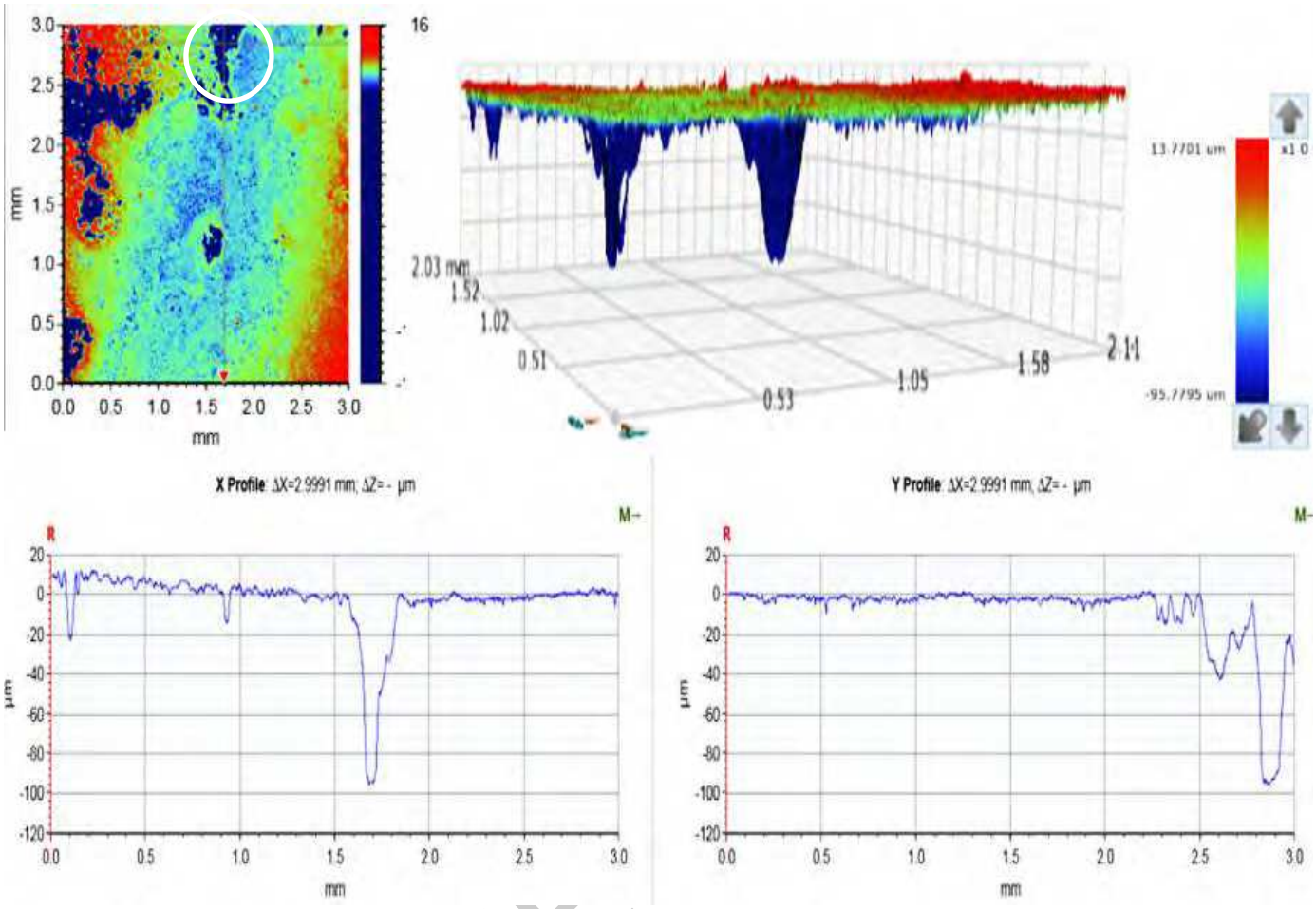

C

Figure 12: 3D images of pitting corrosion damage on carbon steel surface exposed to a) pure CO_2, (b) 1000 ppm of H_2S and (c) 10% of H_2S corrosion system after 168 h at 80℃.